METAL HALIDE PEROVSKITE HETEROSTRUCTURES FOR FUNDAMENTAL STUDIES AND OPTOELECTRONIC APPLICATIONS

by

DONGXU PAN

A dissertation submitted in partial fulfillment of

the requirements for the degree of

DOCTOR OF PHILOSOPHY

(CHEMISTRY)

at the

UNIVERSITY OF WISCONSIN-MADISON

2022

Date of final oral examination: February 17th, 2022

The dissertation is approved by the following members of the Final Oral Committee:

Song Jin, Professor, Chemistry
John C. Wright, Professor, Chemistry
Xudong Wang, Professor, Materials Science and Engineering
Kyoung-Shin Choi, Professor, Chemistry

Preface

Metal Halide Perovskite Heterostructures for Fundamental Studies and Optoelectronic Applications

Dongxu Pan

Under the supervision of Professor Song Jin

University of Wisconsin-Madison

Semiconductor heterostructures are central elements for modern electronics and optoelectronics. Metal halide perovskite is an emerging class of solution-processible semiconductors that exhibits excellent optical and electronic properties. However, heterostructures of Metal halide perovskites remain scarce due to synthetic challenges and the material's labile nature. My graduate research focuses on developing methods that enable the synthesis and fabrication of metal halide perovskite heterostructures, with control over the composition which in turn defines the electronic structure of the heterostructures.

Chapter 1 gives an overview of the development of the synthesis, fabrication, fundamental study and practical application of metal halide perovskite heterostructures. First, I reviewed the efforts on obtaining 3D metal halide perovskite heterostructures, which revealed that the hetero-junctions readily broaden due to rapid anion interdiffusion. Then, I described how two-dimensional (2D) Ruddlesden-Popper (RP) metal halide perovskite could be a diverse and versatile building block for fabrication of both perovskite-perovskite heterostructures and perovskite-2D materials heterostructures. The novel physics observed in, and devices fabricated based on these heterostructure materials are discussed. Finally, I proposed some promising future directions for the emergent 2D RP perovskite van der Waals heterostructures, which could interesting materials platform for exploration of exciton physics and novel device designs.

Chapter 2 presents the visualization and studies of ion-diffusion kinetics in 3D halide perovskites, which revealed rapid anion interdiffusion in these materials even at room temperature. $CsPbCl_3$ microplates were stacked on top of $CsPbBr_3$ nanowires, which led to the formation of $CsPbBr_{3-3x}Cl_{3x}$ (x = 0-1) gradient nanowires because of spontaneous anion interdiffusion. The high photoluminescence in all $CsPbBr_{3-3x}Cl_{3x}$ (x = 0-1) alloy phases and the composition-dependent bandgap allow direct visualization of anion movement through PL imaging. Spatially resolved confocal PL mapping was conducted to extract the composition profiles along the nanowire, and fitting composition profiles using Fick's law allowed us, for the first time, to extract interdiffusion coefficients of the chloride-bromide couple and an activation energy of 0.44 ± 0.02 eV for ion diffusion from temperature-dependent studies, which is orders of magnitude lower than those in the traditional III-V epitaxial heterostructures. These findings confirm the soft and dynamic lattice of 3D halide perovskite and provide mechanistic insights on the ion migration dynamics.

Chapter 3 reports an epitaxial growth of halide perovskite on oxide substrate. Specifically, we grow ultra-smooth $CsPbBr_3$ single-crystal thin films (SCTFs) on gallium gadolinium garnet (GGG) (100) substrates by chemical vapor deposition. We found that despite the lattice mismatch, good incommensurate epitaxy was achieved between $CsPbBr_3$ and GGG, with $CsPbBr_3$ [100] || GGG [100] and $CsPbBr_3$ [010] || GGG [010]. The resulting $CsPbBr_3$ SCTFs exhibit excellent crystal quality, surface smoothness, and high environmental stability, which make it an ideal building block for integration with other materials or fabrication of heterostructure devices. This success of this growth demonstrates the relaxed lattice matching in halide perovskite epitaxy, probably due to the ionic bonding characteristic, and opens up the possibility to integrate halide perovskites on various multi-functional oxide substrates.

In Chapter 4, we demonstrate the deterministic fabrication of arbitrary vertical heterostructures of 2D RP perovskite enabled by our developed synthesis and transfer methods. The direct and highly anisotropic growth of large-area RP perovskite nanosheets of with thickness down to a monolayer was enabled by a floating growth method at solution-air interface. By tuning the precursor ratios and optimizing the synthetic conditions, a great diversity of different RP perovskite phases can be obtained. Moreover, we discovered that by using a soft and hydrophobic polymer stamp, we can readily pick up the as-grown floating nanosheets and transfer them onto arbitrary substrate without compromising their structural integrity. These advances enable the fabrication of arbitrary vertical heterostructures and multi-heterostructures of RP perovskites with unprecedented structural degrees of freedom that define the electronic structures of the heterojunctions. In these novel heterostructures, interesting interlayer properties, such as interlayer carrier transfer and reduction of photoluminescence linewidth, were observed. The diverse RP perovskite phases and the potential integration of them with other 2D materials could enable unlimited heterostructure configurations and serve as ideal platforms for the exploration of exciton physics and optoelectronic applications.

Chapter 5 discusses the structural and property modulation in 2D RP perovskite through large A-cations. We obtained a whole series of 6 different $(PA)_2(A)Pb_2I_7$, which allowed us to systematically study how the A-cations influence the crystal structures and thereby the optoelectronic and ferroelectric properties in halide perovskites in general. We found that in contrast to common belief of A-cation size being the driving force for structural distortion, the shape and dipole of the organic cations also play important role in the structural and subsequent property modulations. Specifically, we analyzed the lattice expansion and distortion in different $(PA)_2(A)Pb_2I_7$, and the potential emergence of ferroelectricity due to “Pb-off-centering”. Optical

studies and DFT calculation were also conducted to correlated the relationship between structures and properties.

The following appendices provide supplementary information to the works presented in the main chapters. Specifically, Appendices 1, 2, 3, and 4 provide additional figures and tables pertaining to Chapters 2, 3, 4, and 5, respectively.

The body of the thesis presented here constitutes a significant advance toward understanding the crystallization of halide perovskite materials and development of stable halide perovskite heterostructures. The breakthrough in the growth of various 2D RP perovskites nanosheets and deterministic fabrication capability adds the diverse RP perovskite to the already rich 2D materials toolbox, which gives access to potentially unlimited heterostructures configuration to explore exciton physics. It also opens up opportunities for studying the intrinsic properties and unusual photophysics, and eventually exploiting the high-performance optoelectronic applications of these heterostructures.

Acknowledgements

It has been a very long and colorful 6 years and it also feels just like a flash. Finally, the journey is near its end, and it would not have been possible without the love, guidance, support, and companion from many people.

I must first dedicate my gratitude to my parents, who have been always supportive and let me choose my own life, who always worry about me but never let it becomes my distraction, who never said much but made me feel their love is always all around me. I am really grateful for having the best parents ever.

I must also express my sincere appreciation to my Ph.D. advisor, Prof. Song Jin. You offered me great freedom to explore, to err and to enjoy doing research. Your passion, your rigor, and your philosophy of life and work have been of vital influence in shaping who I am today, and they will be a ever-lasting source of motivation in the future. Thank you!

I would like to acknowledge my committee members, Prof. John C. Wright and Prof. Xudong Wang for witnessing and guiding my growth throughout the years. I would like to thank Prof. Kyoung-Shin Choi for reading and providing insightful comments on my dissertation.

I would like to extend my love and appreciation to all Jin group members that shared my journey in the past 6 years. I must first thank my mentor, Dr. Yongping Fu, for being a living example in research, for shaping my thinking, and providing guidance on many projects. I thank all people who are or have been in the perovskite subgroup for the candid suggestions and help along the way: Dr. Jie Chen, Dr. Matthew Hautingzer, Dr. Meiying Leng, Dr. Ming-Yu Kuo, Willa Mihalyi-Koch, Chris Roy and Kristel Forlano. Special thanks to Dr. Yuzhou Zhao and Dr.Weijie Li for helping me on research projects, and being my best friends and shared various Chipotle trips. I thank senior members in the Jin group Dr. Melinda Shearer, Dr.Matthew Stolt, Kyle Czech, Dr.

Lichen Xiu, and Dr.Lianna Dang, for helping me get started and teaching me various lab techniques. Thank my peers Dr. Matthew Hautingzer, Dr. Natilia Spitha, Dr. Hongyuan Sheng, Dr. Tim Tiambeng for sharing various memories together. I also want to express my appreciation to the postdoctoral researchers and visitors, Dr. Bo Song, Dr. Yifan Dong, Dr. Ying Yang, Dr. Liang Cai, Dr. Jinzhen Huang, Dr. Huawei Liu, Dr. Fengmei Wang, Dr. Hui-Chun Fu, and Dr. Chih-Jung Chen. Finally, my appreciations and best wishes to David Roberts, Chris Roy, Dominic Ross, Katelyn Michael, Willa Mihalyi-Koch, Emily Reasoner, Rui Wang, Erika Jackson, Kristel Forlano, Yueai Lin, Chris Triggs, Gerardo Quintana Cintron, Ethan Auleciems, Jaan Andrews.

I was fortunate to have collaborated many talented and motivated folks, who made important contributions to my research works. I thank Kyle C. Czech, Dr. Natalia Spitha, Dr. Dan Kohler, Dr. Darien Morrow, Jason Scheeler, and David Lafayette for help on various photophysical measurements and the rest of solar group for great discussions and suggestions. I thank Kyana Sanders and Dr. Ilia Guzei for the heroic efforts on solving many challenging crystal structures fo me. I thank Zhengbang Dai from Prof. Andrew Rappe's group in University of Pennsylvania for DFT calculations on the band structures of RP perovskites. I appreciate the help from Dr. Andrew Jones, Zachary Armstrong from Prof. Martin Zanni's group for ultrafast spectroscopic measurements; Dr. Weihao Zheng and Ziyu Luo from Prof. Anlian Pan's group in Hunan University for the collaboration on the interlayer exciton characterizations; Dr. Tze-hsuan Zhang from Prof. Jack Ma's group in MSE for collaboration on the device fabrication; Corey Carlos from Prof. Xudong Wang's group in MSE for PFM measurements on perovskite nanosheets; Shane Lindemann from Prof. Chang-Boem Eom's group in Engineering for attempts on ferroelectric characterizations; Dr. Chenyu Zhang from Prof. Paul M. Voyles's group in MSE for the help on STEM characterization,

My life in Madison and graduate school would not have been so colorful, and I wouldn't have survived the shutdowns during pandemic without my friends. Particularly, I would like to thank Dr. Beini Lyu for being an excellent roommate and helping me take care of Tiger. I would like to thank Team Shell Friday members Dr. Qingwei Wang, Dr. Yue Zha, Dr. Ruxiu Zhao, Dr. Ruohan Zhang, Dr. Chenlai Shi for playing with me in so many intramural bastketball tournaments; I thank the WiSolve gang Jennifer Peotter, Shaswath Sekar Chandrasekar, Dr. Dan Radecki, Dr. Xiangyang Liu, Dr. Annie Zhang, Emmar Lazaroff, Amy Qin, Ryan Trevena and Tyler Ogorek. I would also express my gratitude to other wonderful people I met in Madison, who shared a lot of memories throughout the years.

Lastly, my special appreciation to Rui Chen, who has supported me in some of my darkest moments and has been my source of motivation ever since.

Dongxu Pan

02/04/2022

Table of Contents

List of Figures and Tables

Chapter 1 Challenges and Progress Towards Stable Metal Halide Perovskite Heterostructure

1.1 Abstract

Metal halide perovskites materials have gained significant research attention in the past decades as promising optoelectronic and photovoltaic materials, because of their inherently high photoluminescence quantum yield, long carrier diffusion length, high absorption coefficient, great defect tolerance and solution processibility. The emerging two-dimensional (2D) Ruddlesden-Popper (RP) phase halide perovskites inherit the desirable properties of 3D perovskites with improved environmental stability. To further improve the performance and realize extended functionalities of halide perovskite-based devices, it is of interest to explore the synthesis, fabrication, and stabilization of halide perovskite heterostructures as well as its integration with other materials, which have been challenging due to the labile nature of the materials. Particularly, the unique modular structure of 2D RP perovskites endows great tunability of the optical and electronic properties. Interfacing the diverse 2D RP perovskite with other 2D materials including graphene and transitional metal dichalcogenides (TMDs) through van der Waals (vdW) stacking potentially offers unlimited heterostructure configurations for exploration of novel physic in semiconductor heterostructures and design of high-performance applications. In this article, we review the progress of the above-mentioned topics, and discuss the challenges remaining and future promising directions in this field.

1.2 Introduction

Semiconductor heterostructures are central elements for modern electronics and optoelectronics. Compared with single component devices, heterostructures can efficiently manipulate the generation, recombination and transport of carriers, leading to unique properties or

extended functionalities in optoelectronic devices. The breakthrough in epitaxial crystal growth led to the invention of III-V, II-V semiconductor quantum well (QW) and superlattices that exploit quantum confinement to engineer electronic states with custom-designed properties.[1-3] Development of van der Waals heterostructures constructed by stacking two or more layers of atomically thin two-dimensional (2D) materials such as graphene and transition metal dichalcogenides (TMDs) largely relaxed the requirement on lattice-matching.[4,5] New physical phenomena such as interlayer exciton and moiré excitons observed in such heterostructure are of great interest.[6-8]

In the recent years, metal halide perovskites (MHPs) have drawn great research interest as an emerging class of solution-processed semiconductors. The general formula of MHPs is ABX_3, where A represents a monovalent cation, B is usually Pb or Sn, and X corresponds to a halogen (Figure 1.1a). They were first reported as promising visible-light sensitizers in PV cells with a power conversion efficiency (PCE) of 3.9% in 2009[9], which has now exceeded 25% in 2021 in MHPs-based solar cells.[10] Moreover, MHPs-based optoelectronic devices, including lasers[11,12], photodetectors[13], and light-emitting diodes (LEDs)[14], have demonstrated decent performance. The outstanding performance of MHPs can be attributed to their superior characteristics, such as large optical absorption coefficient, high and balanced carrier mobility, long carrier diffusion length and great defect tolerance. Because of the excellent properties and the facile synthesis, it is attractive to explore heterostructures of halide perovskites for applications beyond optoelectronic devices, such as transistors, lasers and memory devices. However, the high anion diffusivity and poor stability pose challenges in obtaining high-quality and stable halide perovskite heterostructures.

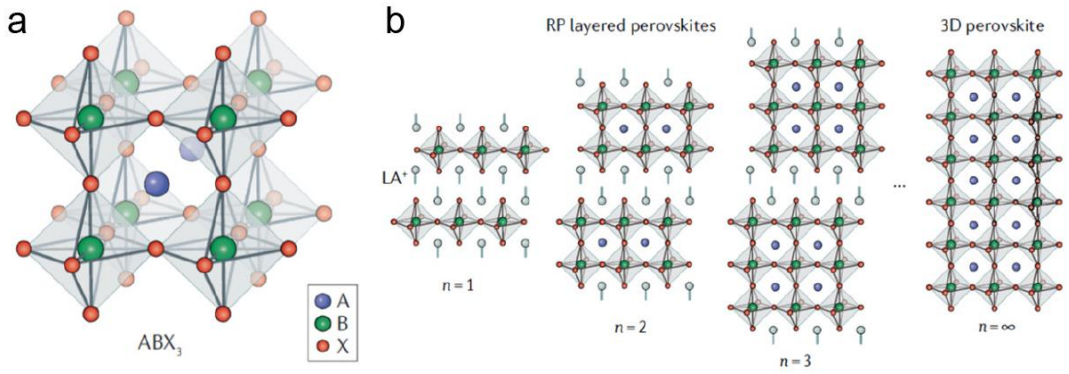

Figure 1.1 Crystal structures of (a) 3D metal halide perovskite (a) and 2D (b) Ruddlesden-Popper halide perovskites.

A is a cation, such as methylammonium (MA) or formamidinium (FA); B is Pb^{2+} or Sn^{2+}, and X is a halide anion. The number of $[PbX_6]^{4-}$ layers in 2D RP perovskite is indicated by the n number.

One strategy to suppress anion diffusion and realize stable heterostructure is to introduce long-chain organic cations and form two-dimensional (2D) Ruddlesden-Popper (RP) perovskites (Figure 1.1b). They have the general formula of $(LA)_2(A)_{n-1}Pb_nX_{3n+1}$, where LA is a long-chain alkylammonium cation, A is a small cation such as methylammonium (MA) and formamidinium (FA), X is a halide anion, and *n* is an integer. Their crystal structures consist of stacked 2D layers of $[(A)_{n-1}Pb_nX_{3n+1}]^{2-}$ inorganic framework charge balanced by the organic LA cations in the interlayer space. They inherent the good optical properties from the parent 3D halide perovskite, with improved the environmental stability and suppressed anion interdiffusion, thanks to the hydrophobic LA layers. These structures are often seen as natural multiple-quantum-wells in which the nanometer thick inorganic layers act as potential "wells" and the interlayer organic layers act as potential "barriers"[15], akin to III–V semiconductor quantum wells[16-19]. Due to the low dielectric constant of the interlayer cations, the excitons residing in the well experience significantly enhanced Coulomb interaction with exciton binding energies up to a few hundred meV[20]. Most significantly, such inherent quantum and dielectric confinement can be readily tuned

at the molecular level, in addition to the composition-dependent bandgap. These make RP perovskites a diverse and versatile 2D materials platform[21-24] for exploring exciton physics and high-performance optoelectronic devices, as demonstrated in van der Waals heterostructures of transition metal dichalcogenides (TMDs). Fulfilling the promises of 2D RP perovskite heterostructures, however, has been challenging, due to the fragile nature of halide perovskite materials and the lack of ideal synthesis that has control over composition and morphology[25,26].

In this review, we will summarize recent research activities in the synthesis, fabrication, characterization and application of halide perovskite heterostructures, spanning from heterostructures between 3D perovskites with different halide anions, to heterostructures between 2D RP phase halide perovskite, and finally heterostructures between halide perovskites and other 2D materials. We exclude bulk crystals, poly-crystalline thin-film as well as colloidal nanocrystal heterostructures from this account, and *focus on the nano- and micromaterials,* because of higher quality interface. In addition, the nano- or micro-dimension facilitates compositional, morphological and structural characterizations. Finally, we will discuss the challenges and perspectives of halide perovskite heterostructures, which will provide new insights into future research of high-performance applications as well as fundamental studies.

1.3 Three-dimensional halide perovskite heterostructures

1.3.1 Synthesis and fabrication methods

3D halide perovskite heterostructures have been created between two types of halide perovskites (Figure 1.2a), with methods including post-synthetic ion-exchange, epitaxial growth and spontaneous phase separation.

Most commonly adopted ion-exchange approach takes advantage of the “soft” and dynamic lattice of halide perovskites. For example, immersing a single crystal of $MAPbBr_3$ into a $MAPbI_3$

solution for a few seconds yields a $MAPbBr_3$/$MAPbI_3$ bulk heterostructure (Figure 1.2b).[27] A clear interface between the black $MAPbI_3$ phase and the orange $MAPbBr_3$ phase was observed. However, due to the large size of the crystal and limited ion diffusion rate, only a thin surface layer of $MAPbBr_3$ was transformed into $MAPbI_3$, and the interface between the two phases is blurry with a composition gradient spanning over a few micrometers. On the same scale, a bulk single-crystal $MAPbI_3$-$MAPbCl_3$ heterostructure has been grown epitaxially by continuously adjusting the precursor solution (Figure 1.2c).[28] But the interface can be as broad as 1 mm and the $MAPbI_3$ region became heavily alloyed so it appeared orange instead of black.

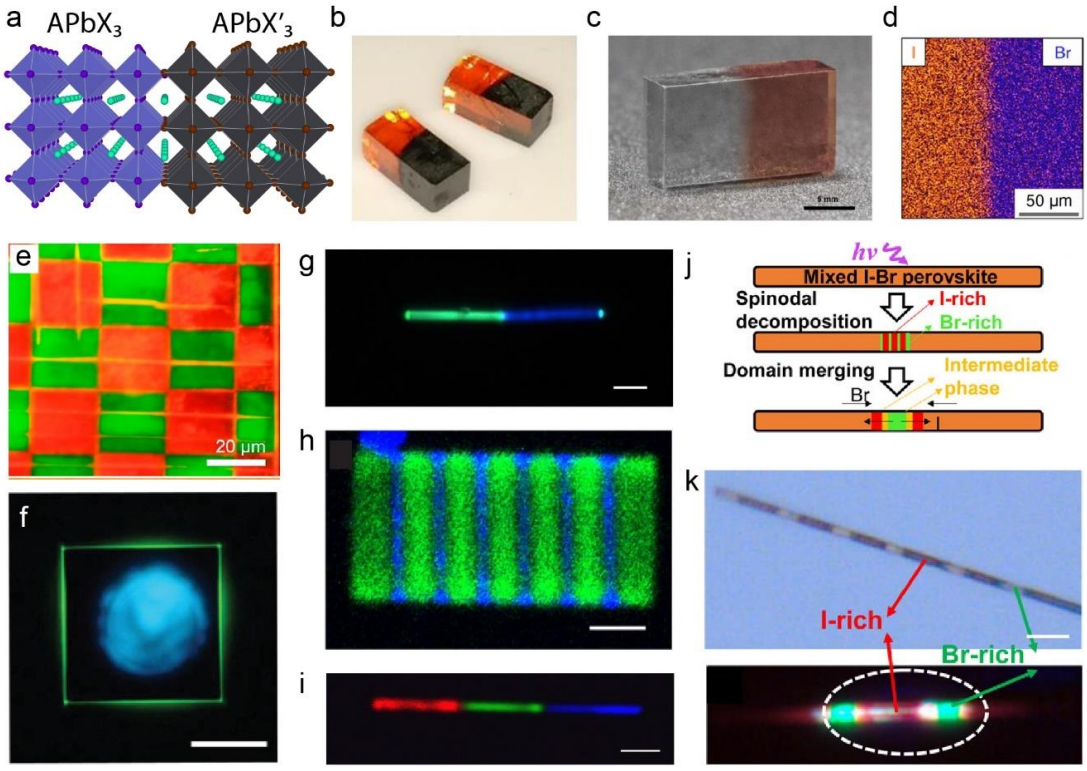

Figure 1.2 Three-dimensional perovskite heterostructures.

(a) Schematic illustration of 3D halide perovskite heterostructures with different halide $APbX_3$-$APbX'_3$. (b) Bulk $MAPbI_3$-$MAPbBr_3$ heterostructure from ion exchange. (c) Bulk $MAPbI_3$-$MAPbCl_3$ heterostructure from epitaxial growth. (d) EDS elemental mapping of thin-film $MAPbI_3$-$MAPbBr_3$ via selected-area ion exchange. (e) PL image of chessboard-patterned $CsPbBr_3$-$CsPbI_3$

thin film heterostructure. (f) PL image of $CsPbCl_xBr_{(3-x)}$-$CsPbBr_3$ lateral heterostructure microplates epitaxially grown on mica substrate. Confocal PL mappings of a $CsPbCl_3$ (blue, 410-450 nm)-$CsPbBr_3$ (green, 500-550 nm) nanowire (g), a bromide-chloride superlattice nanoplate (h), and a $CsPbCl_3$ (blue, 410-450 nm)-$CsPbBr_3$ (green, 500-550 nm)-$CsPbI_3$ (red, 580-640 nm) nanowire (i). Scale bars in panels g-i are 3 μm. panels g-i. (j) Schematics showing the proposed microscopic process for illumination-induced spinodal decomposition. (k) Optical image of multiple double heterojunctions patterned on a single nanowire by laser irradiation. The two different phases show clear contrast in bright-field image (above) and distinct PL emissions (below). The green color emission corresponds to Br-rich phase and the red color to I-rich phase. Scale bar: 4 μm.

In addition to bulk crystals, thin-film 3D halide perovskite heterostructures can also be fabricated via ion exchange. Kennard et al. demonstrated the fabrication of lateral $MAPbI_3$-$MAPbBr_3$ heterostructure by exposing partially exposed $MAPbI_3$ spin-coated thin film to Br_2 vapor.[29] The energy-dispersive (EDS) elemental mapping (Figure 1.2d) shows the boundary between the iodide phase and the bromide phase. Like in the case of bulk crystals, the interface is still blurry, due to the rough spatial resolution of the physical shadow mask (e.g. PDMS) applied and the intrinsically rapid halide interdiffusion. Wang et al. reported large-area epitaxial growth of monocrystalline $CsPbBr_3$ thin film on muscovite mica, and subsequent selective transformation into $CsPbI_3$, forming a patterned $CsPbBr_3$-$CsPbI_3$ lateral heterostructure array.[30] Better spatial resolution and sharper junction were achieved in such lateral heterostructure via electron-beam lithography. Figure 1.2e shows a spatially resolved PL image of the heterostructure array. The areas without anion-exchange retains the intense green-light emission from $CsPbBr_3$ and the areas after anion-exchange show distinct red-light emission from $CsPbI_3$.

Compared to bulk crystals and thin films, 3D halide perovskite heterostructure fabricated on single-crystal nano- or micro-objects are advantageous in getting abrupt hetero-interfaces because the high-aspect ratio facilitates complete anion exchange in one dimension while maintaining a sharper interface in the other dimension. Ren et al. fabricated $CsPbCl_xBr_{(3-x)}/CsPbBr_3$ lateral heterostructures in microplates through controlled chemical vapor deposition.[31] The PL image of the as-grown lateral heterostructure (Figure 1.2f) shows the interior and the periphery of the microplates exhibit bright cyan and green emissions, corresponding to regions of $CsPbCl_xBr_{(3-x)}$ and $CsPbBr_3$ components, respectively. The width of the $CsPbBr_3$ periphery is determined to be ~ 1 μm. Dou et al. fabricated diverse one-dimensional (1D) and two-dimensional (2D) halide perovskite heterostructures using electron-beam lithography to partially expose the nanowires or nanoplates to solutions with different halides in 1-octadecene.[32] $CsPbCl_3$ (blue)-$CsPbBr_3$ (green) nanowire (Figure 1.2g), $CsPbCl_3$ (blue)-$CsPbBr_3$ (green) superlattice nanoplate (Figure 1.2h), and $CsPbCl_3$ (blue)-$CsPbBr_3$ (green)-$CsPbI_3$ (red) multi-heterostructures nanowire (Figure 1.2i) are shown to represent the successful transformation using such method.

In addition to ion exchange strategy, 3D halide perovskite heterostructures can be formed via spontaneous phase separation in alloyed phases. The I/Br mixed halide alloy phase is unstable thermodynamically and undergoes rapid spinodal decomposition upon external stimulation such as laser illumination. Wang et al. demonstrated that high-energy photon could generate high vacancy concentration in the illuminated area (Figure 1.2j), which will facilitate the anion-interdiffusion process in the kinetically-trapped mixed-halide alloy phase and allow it to phase separate into I-rich and Br-rich phases, resulting in a double heterostructure as shown in Figure 1.2k.[33] However, such photoinduced phase separation is undesired in optoelectronic applications.

1.3.2 Fast anion-interdiffusion kinetics

Although various 3D halide perovskite heterostructures have been successfully synthesized or fabricated, interfaces between the different phases in many of the heterostructures are very diffusive, due to the lack of control over synthesis or conversion reactions. Even if the as-fabricated junction appeared to be abrupt and pristine at first, it is prone to broaden itself overtime due to the unavoidable anion interdiffusion in the soft and dynamic crystal lattice of halide perovskites.

The quantitative ionic diffusivity in halide perovskite have been investigated using electrical measurements and polycrystalline samples.[34,35] These results reflect contributions from both cations and anions and are often complicated by grain boundaries. In contrast, the single-crystalline nano- and micro-structures are free of grain boundaries and thus are ideal material platforms for fundamental studies of anion diffusion kinetics. Particularly, the perovskite nanowires with one-dimensional (1D) geometry provides directional channels for ion migration and allows simple modeling. Our group fabricated a heterostructure of $CsPbCl_3$ microplates on $CsPbBr_3$ nanowire networks, and visualized the solid-state anion interdiffusion via confocal PL imaging.[36] As shown in Figure 1.3a, thermodynamically favored interfacial halide exchange reaction would occur between the microplate and nanowire, followed by axial concentration-gradient driven chloride/bromide interdiffusion. Owing to the strong photoluminescence of the perovskite nanowires, the anion interdiffusion process was directly visualized in a series of time-dependent PL images (Figure 1.3b). The blue and green emissions come from the Cl-rich regions and Br-rich regions, respectively. The evolution of emission color can be correlated with the spatial change of halide composition (Figure 1.3c), and by fitting the composition-profiles to Fick's law, the bromide-chloride interdiffusion coefficient is estimated to be 1.40×10^{-10} $cm^2\ s^{-1}$ at 200 °C, much faster than in the traditional III-V semiconductors.[37] Lai et al. presented a similar study on the anion interdiffusion in $CsPbCl_3$-$CsPbBr_3$ nanowire heterostructures, and found halide diffusivities

to be ~ 10^{-12} cm^2 s^{-1} at 100 °C.[38] The diffusion is found to be vacancy mediated (Figure 1.3d-e), and the free energy anions have to overcome to diffuse in an equal-molar mixture by exchanging the their positions are computed to be 0.28 and 0.34 eV for Br and Cl, respectively (Figure 1.3 f-g). Vacancy formation free energies computed from molecular simulation are small, accounting for the high equilibrium vacancy concentration, in consistent with the soft and deformable perovskite lattice, allowing the fast anion diffusion in halide perovskites. Zhang et al. further studied the vapor-solid anion exchange kinetics in single-crystalline halide perovskite nanoplates using confocal photoluminescence microscopy.[39] The anion exchange occurred between CVT grown $CsPbBr_3$ nanoplates and n-$C_4H_9NH_3I$ vapor. The transformation is observed to start from the peripheral sites of the nanoplates, before propagating symmetrically into the center, leading to the formation of $CsPbBr_3$-$CsPbBr(_{1-x}I_x)_3$ perovskite lateral heterostructures (Figure 1.3h, i) with coherent interfaces tunable by reaction conditions. Based on a proposed two-step reaction-diffusion model (Figure 1.3j, k), the halide diffusion coefficient was estimated to be on the order of 10^{-14} cm^2 s^{-1}. These studies unanimously speak to the challenges of stable 3D halide perovskite heterojunctions posed by the high intrinsic ion diffusivities, which prevents practical future applications.

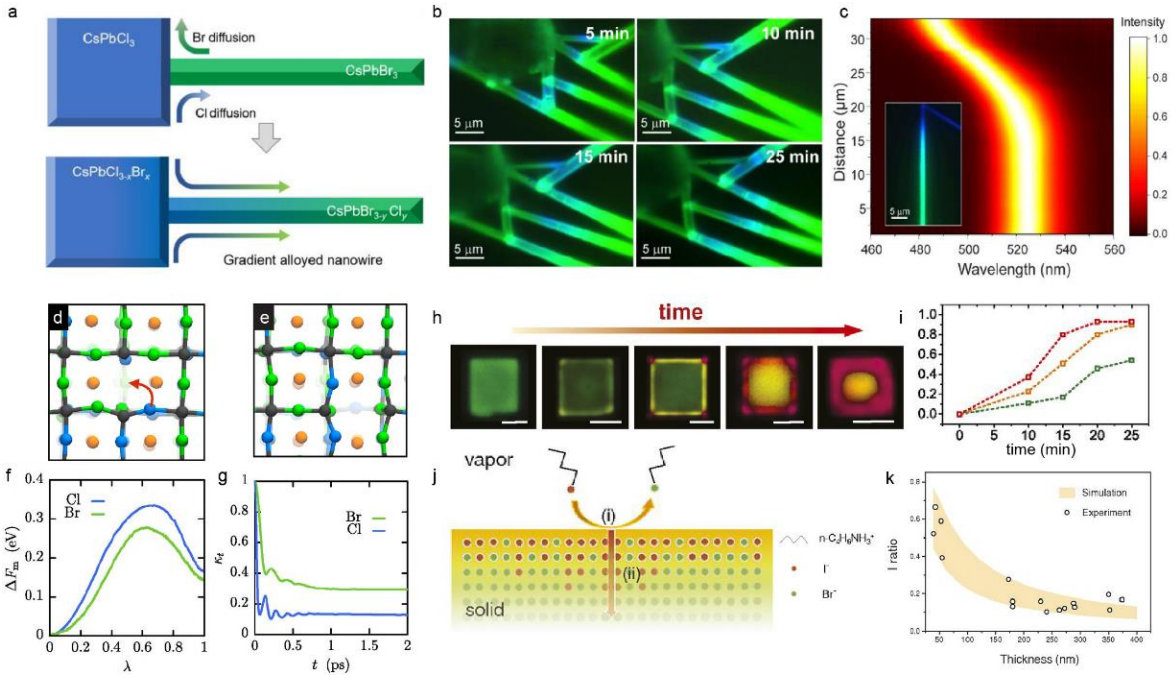

Figure 1.3 Anion-interdiffusion studies in 3D halide perovskites.

(a) Schematic of the perovskite heterostructure fabricated by stacking $CsPbCl_3$ microplate on $CsPbBr_3$ NW and the subsequent solid-state ion interdiffusion process. (b) A set of time-dependent PL images of $CsPbCl_3$/$CsPbBr_3$ heterostructures showing the evolution of anion interdiffusion at 200 °C. (c) Normalized PL profile along a gradient $CsPbBr_{3-3x}Cl_{3x}$ NW formed as a result of anion interdiffusion. The inset is a real-color PL image of the NW under broad laser excitation. (d) MD simulation snapshots of a chloride anion swapping with a vacancy in an equal-molar mixture in the initial position (d) and final position (e). Cesium, lead, bromide, and chloride are colored orange, black, green and blue, respectively. (f) Free energy along halides' trajectories for Cl and Br. $\lambda = (z\text{-}z_i)/(z_f\text{-}z_i)$ is the dimensionless reaction coordinate, with z being the coordinate of the ion. (g) Time-dependent transmission coefficient corresponding to the energy barriers show in f. (h) Confocal PL mapping on a $CsPbBr_3$ nanoplate that underwent vapor-phase anion exchange reaction for 10, 15, 20, and 25 min, respectively. Scale bars: 5 μm. (i) Plots of iodine ratio obtained from PL profile changing with reaction time at the face (green), edge (orange) and corner (red) of

the nanoplate, respectively. (j) Proposed 2-step mechanism for the anion exchange process: i, surface reaction for anion exchange between n-$C_4H_9NH_3I$ vapor and $CsPbBr_3$ nanoplates; and ii, solid-state diffusion of I^- in $CsPbBr_3$ nanoplates. (k) Comparison of the simulation (shaded area) and experimental results of the thickness-dependent I ratio (average) at the center of the plates.

1.4 2D Ruddlesden-Popper phase lead halide perovskite heterostructures

As discussed in the previous section, fast anion interdiffusion has greatly hindered practical application of 3D halide perovskite heterostructures. An effective strategy for improving the environmental stability of halide perovskite and suppressing ion diffusion is to introduce long-chain organic ligands to 3D halide perovskites and form 2D RP phase perovskites.[40,41] As an emerging class of 2D semiconductors, they not only inherit the good optical properties from their parent 3D counterparts, such as high PL quantum yield and high defect tolerance, but also exhibit large exciton binding energies up to hundreds of meV due to dielectric and quantum confinements. More importantly, their unique modular structure endows great tunability on the optical and electronic properties. As a result, 2D RP halide perovskites present unlimited heterostructure configurations for exploration, and could serve as diverse and versatile 2D building blocks for exploring exciton physics and high-performance optoelectronic devices.[21-24].

1.4.1 Epitaxial heterostructures

Constructing 2D RP perovskite heterostructures with different halide is challenging, due to the fast crystallization kinetics and facile formation of alloy phases. Direct synthesis by mixing precursors in solution only led to the formation of mixed halide alloy phases, whereas sequential growth methods with two or more growth steps would generally alter the existing materials. Recently, Shi et al. found that by employing mild growth conditions, including lowering growth temperature and adding more antisolvent in the precursor solution, 2D I/Br perovskite lateral

heterostructures can be grown epitaxially in a 2-step reaction (Figure 1.4a-f).[42] The success of this sequential growth relied on careful engineering of the solubilities of the precursors: the less soluble bromide perovskite was synthesized first, followed by iodide perovskites so that the product from the first step would remain intact. Two different organic ligands were employed to investigate the stability of such lateral heterostructures: a conjugated ligand $2T^+$ (Figure 1.4a,c,d) and an alkyl ligand BA^+ (Figure 1.4b,e,f). The heterostructure nanoplates clearly show different contrast and PL emissions in the inner squares and outer squares, indicating different composition and bandgap. The absence of PL emission from the inner $(2T)_2PbBr_4$ region is due to the type-II band alignment between the inorganic $[PbBr_4]^{2-}$ and organic $2T^+$ layers. Interestingly, compare to alkyl BA^+ ligand, the conjugated 2T+ ligand could significantly inhibit the halide interdiffusion along the in-plane direction across the heterojunction, as shown in the comparison between the PL images of the two heterostructures (Figure 1.4g,h) after heating at 100 °C for 1 h. The EDS elemental mappings (Figure 1.4i) show the distribution of Br and I, in agreement with the optical and PL images. Selected area electron diffraction (SAED) patterns and fast Fourier transform (FFT) patterns clearly show two sets of diffraction spots, corresponding to domains of $(2T)_2PbBr_4$ and $(2T)_2PbI_4$, respectively, with identical orientation, confirming the epitaxial relationship. Furthermore, the suppressed anion interdiffusion led to high-quality and abrupt heterojunctions, as demonstrated by low-dose aberration corrected TEM and HRTEM (Figure 1.4j_1, j_2). The interface is as sharp as a few nanometers, and periodic interfacial misfit dislocations are clearly observed (Figure 1.4k), indicating the edge dislocation is the primary mechanism that enabled the hetero-epitaxy.

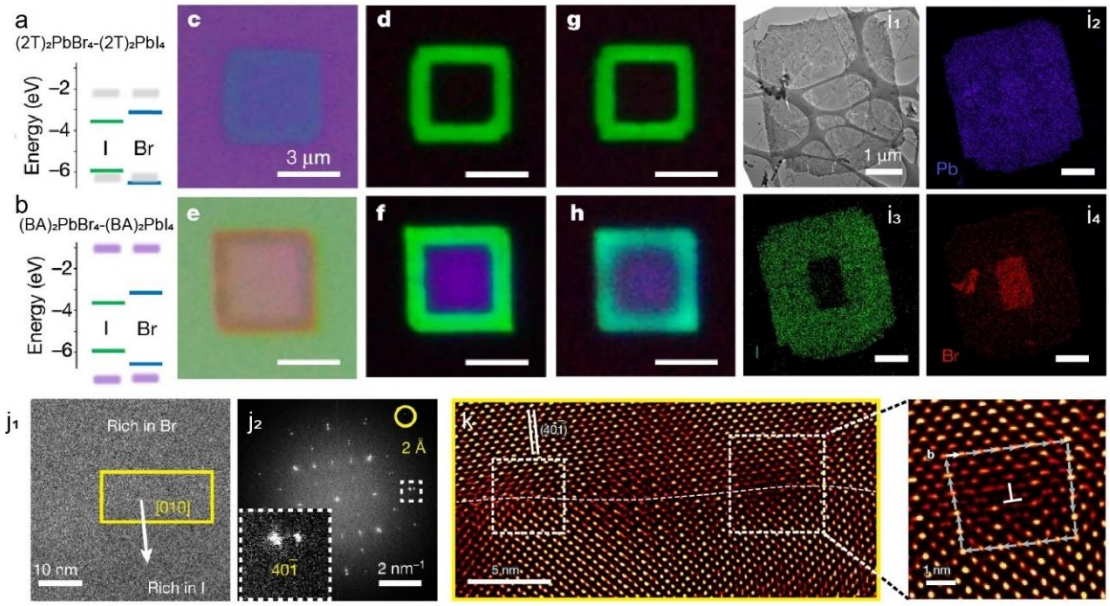

Figure 1.4 Two-dimensional halide perovskite lateral epitaxial heterostructures with different halides.

Proposed band alignment (a), optical (c) and PL (d) image of a $(2T)_2PbBr_4$-$(2T)_2PbI_4$ lateral heterostructure. Proposed band alignment (b), optical (e) and PL (f) image of a $(BA)_2PbBr_4$-$(BA)_2PbI_4$ lateral heterostructure. (g) PL image of the $(2T)_2PbBr_4$-$(2T)_2PbI_4$ lateral heterostructure after 1 h of heating at 100 °C. (h) PL image of the $(BA)_2PbBr_4$-$(BA)_2PbI_4$ lateral heterostructure after 1 h of heating at 100 °C. All scale bars are 3 μm. Low-magnification TEM image (i_1) of a $(2T)_2PbBr_4$-$(2T)_2PbI_4$ heterostructures, where i_2, i_3, i_4, and j_5 show the EDS elemental mappings of Pb, I, and Br, respectively. The scale bars are 1 μm. Angle-corrected-HRTEM (j_1) and Fourier analysis (j_2) of a $(2T)_2PbBr_4$-$(2T)_2PbI_4$ heterostructures. (k) Fourier filtered and magnified AC-HRTEM image showing the epitaxial interface with enlarged image of an edge dislocation. The white arrow denotes the Burger vector.

Such growth strategy can be applied to epitaxial growth other types 2D halide perovskite lateral heterostructures. Figure 1.5 shows the library of 2D halide perovskite lateral heterostructures with distinct organic ligands ($4Tm^+$ and BTm^+, Figure 1.5a), distinct metals (Pb^{2+}

and Sn^{2+}, Figure 1.5b), different octahedrons ($[SnI_4]^{2-}$ and $[PbBr_4]^{2-}$, Figure 1.5c) and different superlattices ($(2T)_2PbI_4$-$(2T)_2PbBr_4$ × 3, Figure, 1.5d). These 2D halide perovskites lateral heterostructures with varies electronic and optical properties provide a more stable platform to study the carrier dynamics and novel exciton physics.

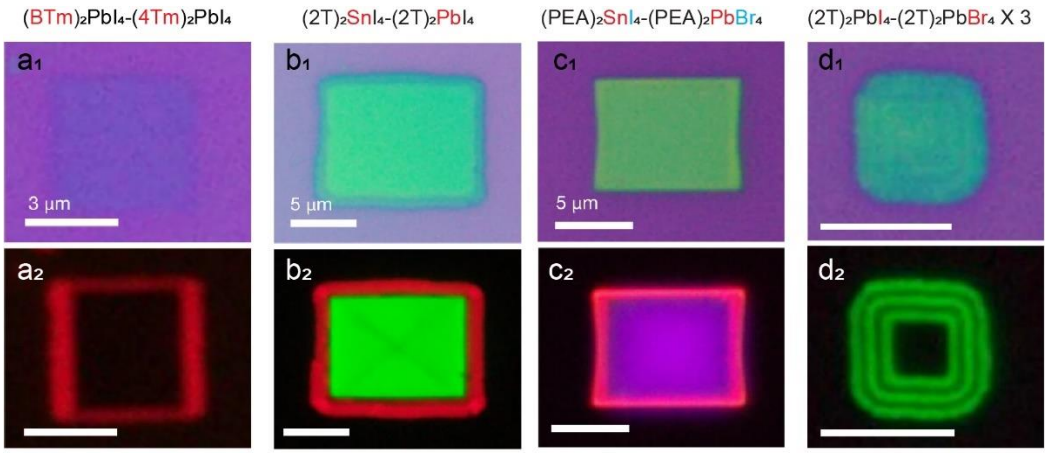

Figure 1.5 Library of different types 2D halide perovskite lateral heterostructures.
(a) $(BTm)_2PbI_4$-$(4Tm)_2PbI_4$ lateral heterostructure with different LA cations. (b) $(2T)_2SnI_4$-$(2T)_2PbI_4$ lateral heterostructure with different B cations. (c) $(PEA)_2SnI_4$-$(PEA)_2PbBr_4$ lateral heterostructure with different B cations and halides. (d) $(2T)_2PbI_4$-$(2T)_2PbBr_4$ × 3 lateral superlattice. a_1, b_1, c_1, and d_1 are optical images; a_2, b_2, c_2, and d_2 are the corresponding PL images. Scale bars in a are 3 μm; all other scale bars are 5 μm.

The above method is, however, limited to 2D perovskites with a single layer of $[PbI_6]$, (n = 1), which have a relatively large bandgap and large exciton binding energy due to the strong quantum confinement. In order to diversify the band structure in the heterostructure, and improve the electrical conductivity of the material, it is desired to construct lateral heterostructures of 2D RP perovskites with higher n values. Toward this goal, our group found a more general approach that enables lateral heterostructures of 2D RP perovskites with $n \geq 1$ to be made via anion

exchange.[43] Specifically, as shown in Figure 1.6a, single-crystal microplates of 2D RP perovskites were exposed to a controlled flow of hydrobromide (HBr) vapor, where Br^- will replace I^- in the perovskite lattice while the H^+ cations are too small to be incorporated as A-cation and shift the equilibrium between RP perovskite *n* phases. Figure 1.6b shows an optical image of a $(HA)_2(FA)Pb_2I_7/(HA)_2(FA)Pb_2Br_7$ lateral heterostructure. The binary interface can be clearly seen in the PL image (Figure 1.6c), where the blue and green regions correspond to characteristic emission wavelengths of 445 nm for $(HA)_2(FA)Pb_2Br_7$ and 580 nm for $(HA)_2(FA)Pb_2I_7$, respectively, confirming the inner and outer components as pure single halide phases. Time-of-flight secondary ion mass spectroscopy (ToF-SIMS) reveals that iodide is exclusively present in the center of the microplate (Figure 1.6e), whereas bromide is present across the entire top surface (Figure 1.6d), which is due to the slow but non-zero out-of-plane anion exchange. SEM-EDS mapping performed on a heterostructure with the top layer exfoliated (Figure 1.6f-h) eliminates this convolution and shows a sharp I/Br lateral interface over a distance of ~ 2 μm. Furthermore, we found the sharpness of the heterojunction formed this way depends on the quantum well thickness (*n* value), and is further modulated by the spacer and A-site cations (Figure 1.6j). Because of the layered structure, the anion exchange kinetics is substantially fasted in the lateral direction along the basal planes than in the vertical direction across the organic LA bilayers. Depending on the extent of such anisotropy: when $n \leq 2$, sharp junctions are formed, but when $n \geq 3$, more diffuse junctions are formed, similar to those in 3D perovskites (Figure 1.6a). This contrast is demonstrated by the sharp heterojunctions formed in $n = 1$ and $n = 2$ microplates (Figure 1.6k,l), and gradient colors observed toward the edge of the $n = 3$ microplates (Figure 1.6m). Importantly, in distinction to 3D halide perovskite heterojunctions, such 2D halide perovskite lateral junctions remained sharp under elevated temperatures of 50 °C, which is harsher that the

normal operating conditions of many optoelectronic devices. These stable lateral heterostructures with great diversity and tunability are of potential for future optoelectronic device applications.

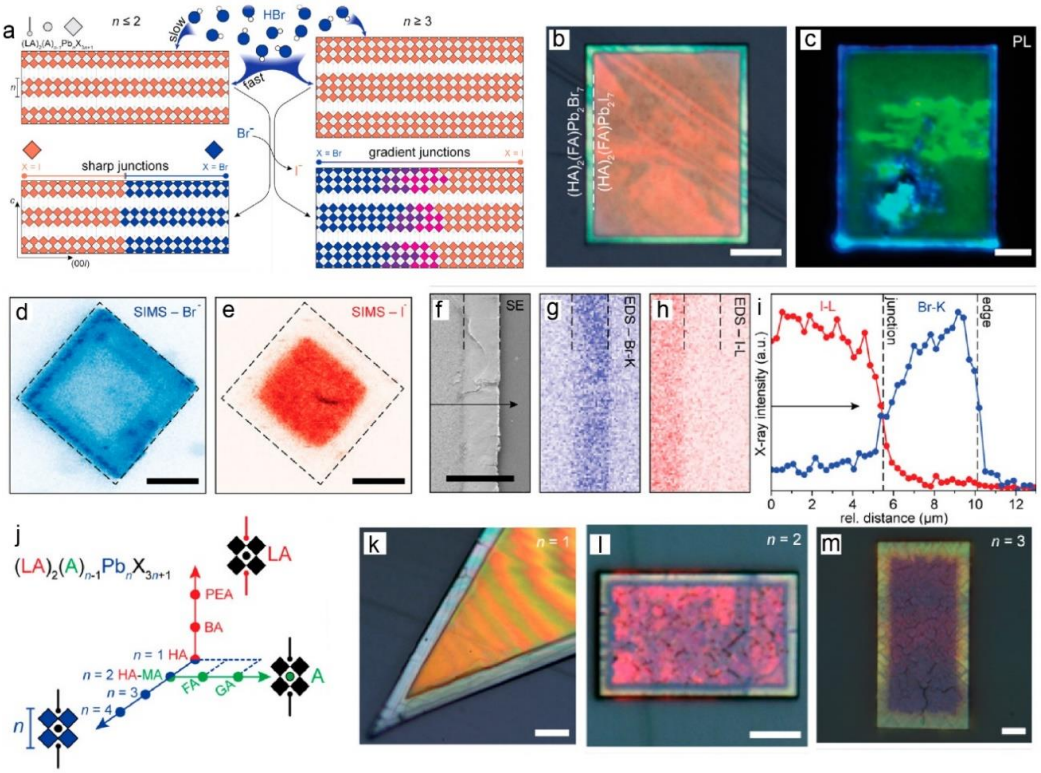

Figure 1.6 2D RP halide perovskite lateral heterostructures fabricated from anion exchange. (a) Scheme showing the formation of halide hetero-junctions in 2D RP perovskites via vapor-solid anion exchange reaction. Sharp junctions are formed in $n \leq 2$; when $n \geq 3$, gradient junctions are formed instead. Blue and red diamonds represent $[PbBr_6]^{4-}$ and $[PbI_6]^{4-}$ octahedra, respectively. Optical image (b) and PL image (c) of a $(HA)_2(FA)Pb_2I_7$-$(HA)_2(FA)Pb_2Br_7$ lateral heterostructure. ToF-SIMS halide maps of a lateral heterostructure showing bromide (d) and iodide (e) signal intensities, respectively. The physical outline of the microplate is shown by the dashed line. Top-down SEM image (f) of an exfoliated layer of a lateral heterostructure and EDS elemental mapping of Br (g) and I (h), respectively. (i) EDS line scan corresponding to the arrow in f. (j) Compositional space mapping of 2D RP halide perovskites. (k-m) Optical images of representative

lateral I/Br heterostructures of the homologous series $(HA)_2(MA)_{n-1}Pb_nI_{3n+1}$ produced by anion exchange. All scale bars are 10 μm.

Another interesting type of 2D RP perovskite heterostructures is between different *n* phases. Due to quantum confinement, the bandgap decreases as the *n* number increases. The early works attempted fabrication of 2D RP halide perovskite $n = 1/n = 2$ heterostructures through vapor phase cation intercalation (Figure 1.7a,b), with methylammonium iodide (MAI) or methylammonium chloride (MACl) vapor as source of MA^+.[25] During the intercalation process, MA^+ is inserted into the center of eight $[PbI_6]^{4-}$ octahedra and the equatorial halide atoms are relocated while two BAI molecules are released. The two phases show distinct colors, where yellow region and red region correspond to $n = 1$ and $n = 2$ phases, respectively. However, the heterojunction formed this way is quite diffuse, as indicated by the PL mapping (Figure 1.7c).

Our group reported a facile one-step solution growth method for 2D RP halide perovskite vertical multiple-heterostructures.[44] By immersing lead acetate thin film into isopropyl alcohol solution of PEA and MA cations, RP phases with different *n* values could nucleate and grow on top of existing layers via van der Waals epitaxy (Figure 1.7d). As each layer in 2D perovskites consists of self-assembled PEA ligands on the surface, the interaction between the neighboring layers is van der Waals in nature, which enables epitaxial integration of different RP phases with atomically sharp interfaces. By changing the PEA to MA ratios, vertical multi-heterostructures with different average $\langle n \rangle$ values can be formed. As shown in the PL spectra (Figure 1.7e) and PL images (Figure 1.7f), these heterostructures display distinctive PL peaks from the individual layers exhibiting different degrees of quantum confinement. Interestingly, the integrated PL intensities from a $n = 1/n = 2$ heterostructure as a function of excitation power density (Figure 1.7g) shows the emission intensity of the $n = 1$ peaks grows linearly with the excitation power density

(β = 0.99), whereas the n = 2 grows super-linearly (β = 1.45), indicating possible carrier transfer between the two phases (Figure 1.7g inset). Time-resolved PL (TRPL) studies further provided convincing evidence of internal energy transfer (Figure 1.7h), as the PL kinetics for the lower-bandgap n = 2 phase emission showed non-monoexponential decay, due to the competitive dynamic between recombination within the layer and energy transfer from the neighboring n = 1 layer. The time scale for such transfer is estimated to be hundreds of picoseconds. These heterostructures capable of emitting multiple colors with high spectral purity are attractive platforms to explore new properties and physics in 2D materials. They also show promise for building versatile photonic devices that are easily solution-processed.

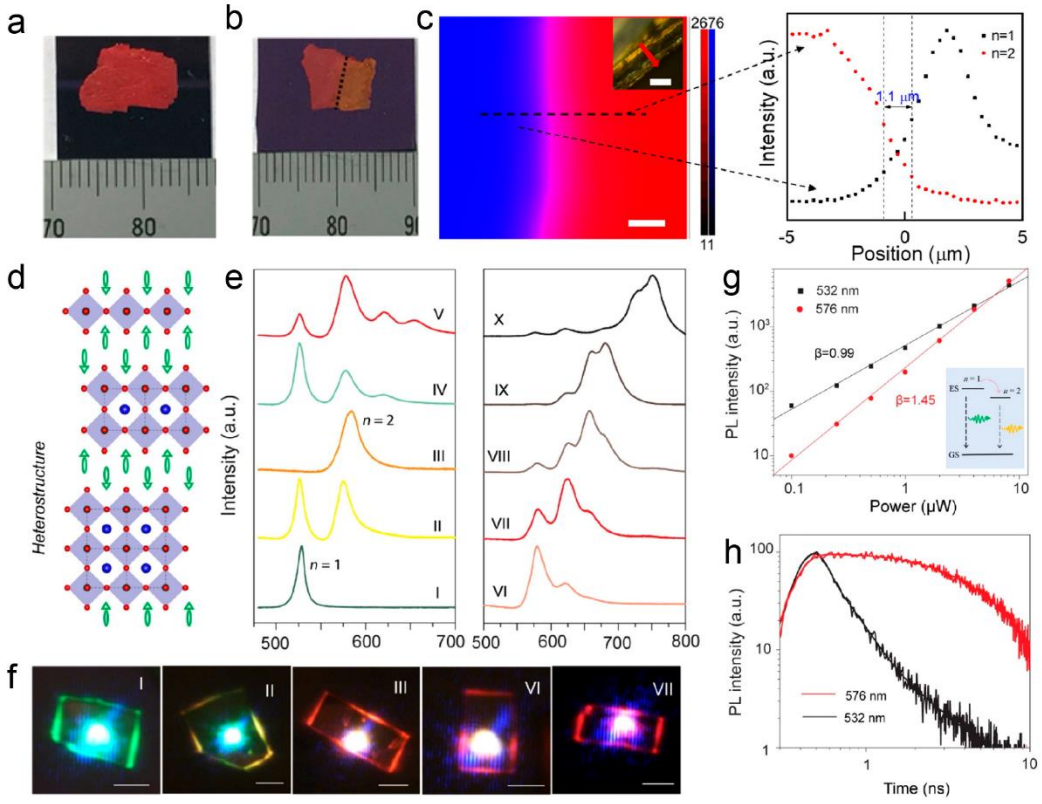

Figure 1.7 2D RP halide perovskite epitaxial heterostructure with different n phases. Optical image of vertical (a) and lateral (b) $(BA)_2PbI_4$ (n = 1)/$(BA)_2(MA)Pb_2I_7$ (n = 2) heterostructure formed vapor phase intercalation reaction. (c) Spatially resolved cross-section PL

mapping at 520 nm (blue, $n = 1$) and 590 nm (red, $n = 2$) of the $(BA)_2PbI_4$ ($n = 1$)/$(BA)_2(MA)Pb_2I_7$ ($n = 2$) heterostructure. Inset shows the cross-section where the PL mapping was acquired. Scale bar for the mapping is 1 μm and 20 μm for the inset image. PL intensity profile was collected along the dashed line. (d) Schematic illustration of the self-assembled vertical heterostructure formed within a microplate with multiple *n* numbers. (e) Confocal PL spectra of various heterostructures. (f) Optical images of various heterostructures under 442 nm laser excitation, showing different emission colors. (g) PL intensity of the 532 nm ($n = 1$) and 576 nm ($n = 2$) peaks as a function of excitation power density in a $n = 1/n = 2$ heterostructure. The slopes are indicated by β. (h) TRPL curves of the $n = 1/n = 2$ heterostructure probed at both components' emission wavelength.

An extreme case of the *n*-heterostructures would be those between 2D perovskites and 3D perovskites ($n = \infty$). The 2D on 3D (2D/3D) perovskite heterostructures marries the environmental stability of 2D perovskites to the superior carrier transport properties of 3D perovskites.[45,46] Also, introducing a thin 2D perovskite layer or embedding 2D perovskites within the grain boundaries of 3D perovskite matrix have been shown to be able to passivate surface defects and suppress interface charge recombination for better device efficiency.[47-49] As a result, 2D/3D perovskite heterostructures have been widely studied and employed in perovskite solar cells[50] and LEDs[51] with both enhanced stability and excellent performance.

However, hindered by the poorly controlled heterointerfaces in spin-coated polycrystalline samples, the exact charge carrier transfer behaviors at the 2D/3D interface are still under debate.[52] And it is challenging to form 2D/3D perovskite heterostructures with clean and well-defined heterojunctions due to the similar solubilities and formation energies for 2D and 3D perovskites. Our group reported a solution growth of 2D/3D perovskite heterostructures with microplates of

2D $(PEA)_2PbBr_4$ horizontally or vertically aligned on the vapor-phase grown single-crystal films of 3D $CsPbBr_3$ (Figure 1.8a).[53] Briefly, 3D $CsPbBr_3$ single-crystalline thin film was first epitaxially grown on STO substrate, where the subsequent epitaxial growth of 2D $(PEA)_2PbBr_4$ occurred. The key factor to the success of this step-wise growth is the sparingly low solubility of $CsPbBr_3$ in IPA, which allowed it to remain largely unchanged during the $(PEA)_2PbBr_4$ solution growth. Interestingly, some $(PEA)_2PbBr_4$ microplates grow vertically along the $CsPbBr_3$ [100] or [010] directions (Figure 1.8c), while others grow horizontally on top of $CsPbBr_3$ (001) (Figure 1.8b).

These well-defined 2D/3D perovskite heterojunctions with different orientations provide ideal platforms for investigating the physical properties and the charge transfer processes across the heterojunctions in a more definitive fashion. We conducted time-resolved photoluminescence (TRPL) studies on horizontally aligned 2D heterostructures with varying 2D thickness, as well as on vertically aligned heterostructures with different probing height along a 2D plate away from the surface of 3D perovskites. Clearly carrier transfer is observed in horizontally aligned heterostructures where the lifetime of the $(PEA)_2PbBr_4$ emission decreases with decreasing microplate thickness, while such trend is absent in the vertically aligned heterostructures, as the $(PEA)_2PbBr_4$ TRPL probed at different heights appear similar. This could be due to the limited exciton diffusion length in 2D n = 1 perovskites. Two kinetic models (Figure 1.8f,g) based on Type-I and Type-II band alignments are then applied to define the observed dynamics, which reveals a shift in balance between carrier transfer and recombination: Type-I band alignment better describes the behaviors of heterostructures with thin 2D perovskite microplates (Figure 1.8h), but Type-II band alignment better describes those with thick 2D microplates (>150 nm) (Figure 1.8i). These results shed new insights on the charge transfer mechanisms in these common 2D/3D

perovskite heterostructures and provide guidelines for designing more efficient solar cell and LED devices on their basis.

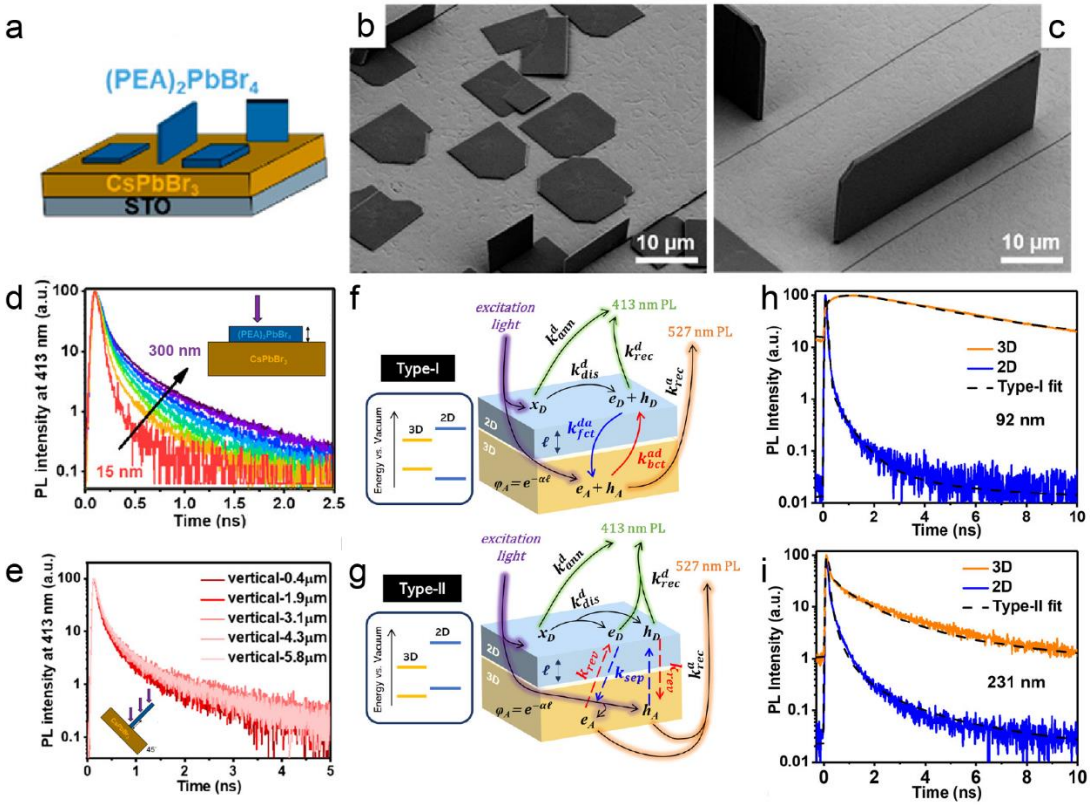

Figure 1.8 2D/3D halide perovskite heterostructures.

(a) Schematics of vertically and horizontally aligned $(PEA)_2PbBr_4$ microplates on $CsPbBr_3$ single-crystal thin films on STO substrate. Representative SEM images of horizontally (b) and vertically (c) aligned $(PEA)_2PbBr_4$ microplates on $CsPbBr_3$. (d) TRPL spectra of the 413 nm emission ($(PEA)_2PbBr_4$) in the heterostructure with varying thickness. The inset shows the measurement schematics. (e) TRPL spectra of the 413 nm emission ($(PEA)_2PbBr_4$) in the heterostructure probed at different height. The inset shows the measurement schematics. Graphical representations of the Type-I (f) and Type-II (g) kinetic models used to fit the TRPL transients of the 2D and 3D perovskite materials in the 2D/3D heterostructures. Kinetic Modeling results of the time-resolved PL of horizontally aligned $(PEA)_2PbBr_4/CsPbBr_3$ heterostructures for selected samples by the Type-I (h) and Type-II (i) models.

1.4.2 2D perovskite/2D materials van der Waals heterostructures

Generally, formation of epitaxial heterostructures requires the two components to have similar crystal symmetry and lattice constant, which greatly limits the choice of materials. In comparison, 2D van der Waals (vdW) integration, through which two component 2D flakes are mechanically stacked to form heterostructures by weak vdW interaction, offers an alternative integration strategy without lattice matching requirement, and enabled fabrication of various 2D materials heterostructures, such as graphene, h-BN and transitional metal dichalcogenides (TMDs). [4,5]

Since the layers 2D perovskites are bonded by weak vdW interactions between the organic ligands, thin flakes can be exfoliated from their bulk crystals, which can then be integrated with other 2D materials to form vdW heterostructures. These novel types of 2D building blocks are very attractive to explore for the following merits: First, the broad variety of RP phases and compositions allow the bandgaps, exciton binding energies, phonon coupling, chirality and non-linear properties of the component 2D perovskites to be rationally designed. Secondly, the poor out-of-plane electrical conductivity of 2D perovskites rendered by the insulating organic ligands could be improved by bandgap engineering and interfacing with other 2D materials. Last but not the least, the 2D materials stacked on top of 2D perovskites can serve as encapsulation layers to further improve the environmental or operational stability of 2D perovskite-based devices. As a result, 2D perovskite/2D materials vdW heterostructures have gained great research attention for both fundamental studies and practical applications.

The heterostructures of 2D perovskite/monolayer TMD are ideal platforms to study carrier transfer behaviors in semiconductor heterojunctions, owing to the great diversity in both classes of materials. Depending on the band alignments (Figure 1.9), different types of carrier transfer are expected: in type-I band-aligned heterostructures, excitons diffuse from the larger bandgap material to the smaller bandgap material, whereas type II band alignment favors electron-hole

separation into different layers. Yang et. al reported giant photoluminescence enhancement in a 2-layer $WS_2/(BA)_2(MA)_3Pb_4I_{13}$ heterostructure (Figure 1.10a-c).[54] The enhancement is attributed to the charge transfer induced dipole moments, which induces a local electrical field, leading to the indirect-to-direct bandgap transition in 2L WS_2. It is also found the TMDs layer on top significantly improved the stability of the 2D perovskite layer underneath. Zhang et. al reported the observation of excitonic energy transfer in monolayer-$WS_2/(C_6H_5C_2H_4NH_3)_2PbI_4$ (PEPI) heterostructure (Figure 1.10d)[55]. Up to 8-fold photoluminescence enhancement (Figure 1.10e) from the WS_2 layer is attributed to Förster-type energy transfer from perovskite layer to WS_2, which is supported by fluorescence microscopy and photoluminescence excitation (PLE) spectroscopy (Figure 1.10f).

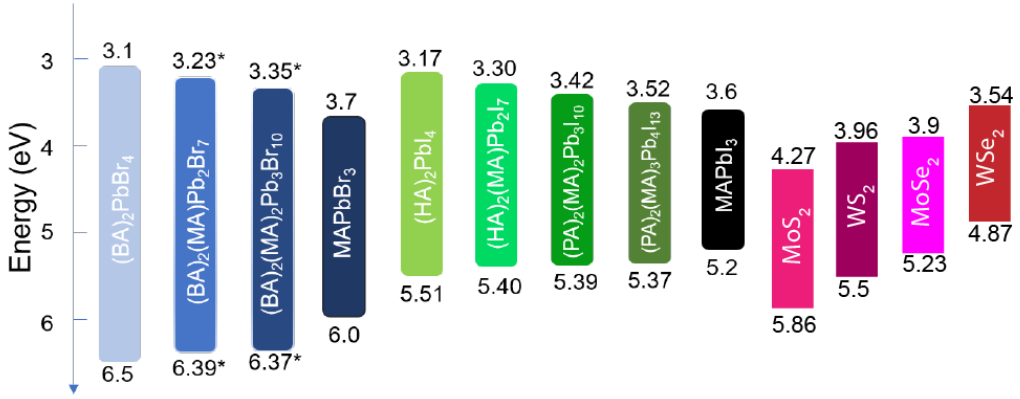

Figure 1.9 Band diagrams of 3D halide perovskite, 2D RP halide perovskite with different n number and TMDs.

In type II monolayer TMDs/2D perovskites, spontaneous electron-hole separation could potentially lead to the formation of interlayer excitons, which have been extensively studied in stacked TMDs heterostructures.[6,7] Chen et. al reported pronounced interlayer exciton emission in $(iso\text{-}BA)_2PbI_4$/monolayer WSe_2 heterostructure (iso-BA=isobutylammonium).[56] The interlayer exciton emission completely dominates the emission spectrum at 78 K (Figure 1.10g).

Interestingly, in distinction with those observed in TMDs heterostructures, the formation such interlayer exciton does not require thermal annealing and is independent of stacking sequence or alignment angle between the component layers.

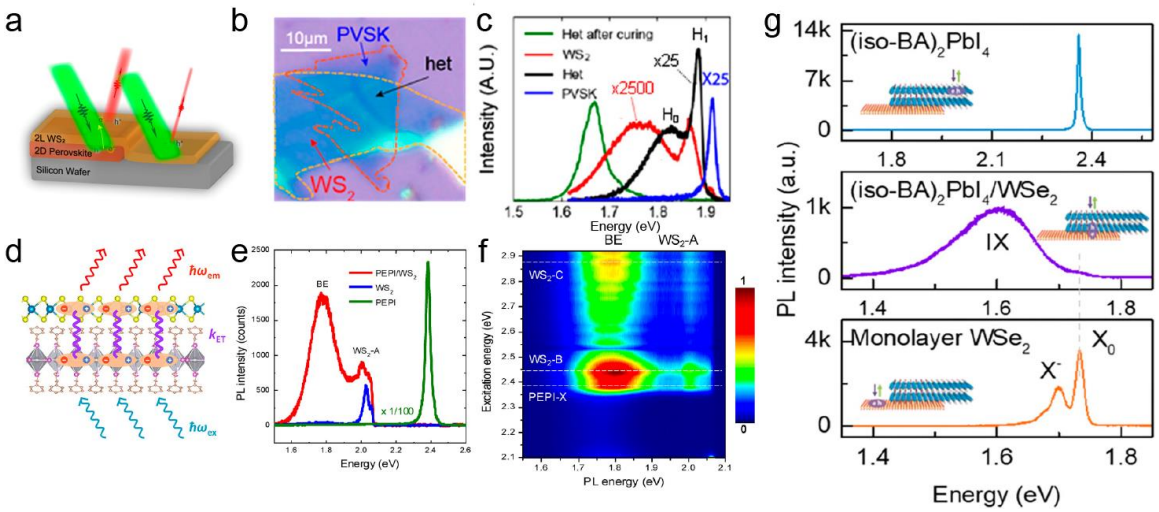

Figure 1.10 Carrier transfer in 2D perovskite/2D materials van der Waals heterostructures. (a) Schematics showing photoluminescence enhancement in 2L-WS_2/$(BA)_2(MA)_3Pb_4I_{13}$ heterostructure. (b) Optical image of the stacked 2L-WS_2/$(BA)_2(MA)_3Pb_4I_{13}$ heterostructure. (c) PL spectra taken at 7 K with 550 nm laser excitation for $(BA)_2(MA)_3Pb_4I_{13}$, 2L (two-layer) WS_2, and their heterostructures before and after curing. (d) Schematic showing excitonic energy transfer in stacked monolayer-WS_2/PEPI (PEPI stands for $(C_6H_5C_2H_4NH_3)_2PbI_4$) heterostructure. (e) PL spectra taken at 110 K PEPI, WS_2, and their heterostructures. (f) Color-coded intensity map of a WS_2/PEPI heterostructure at 110 K. (g) PL spectra of $(iso\text{-}BA)_2PbI_4$ under 473 nm (2.62 eV) excitation, the monolayer WSe2 under 633 nm (1.96 eV) excitation and their heterostructure under 473 nm (2.62 eV) excitation.

Incorporating chiral organic ligands in 2D perovskites allows the carriers to be spin-polarized due to chiral-induced spin selectivity effect.[57-59] Interfacing chiral perovskites with monolayer TMDs may allow the spin- and valley-associated properties to be tuned. Chen et. al reported the

manipulation of valley polarization in chiral $(MBA)_2PbI_4$ ($MBA=C_6H_5C_2H_4NH_3$)/monolayer TMD heterostructure (Figure 1.11a).[60] Due to the selective spin injection from the chiral 2D perovskite to TMDs, persistent valley polarization up to 10% (Figure 1.11c, d) was achieve in monolayer MoS_2 or WSe_2 from liquid-nitrogen temperature to 200 K with 78% average spin injection efficiency, without the need of magnetic field or circularly polarized excitation. Similarly, Huang et. al found the degree of circularly polarized light emission in $(BA)_2PbI_4$ can be up to 30% (Figure 1.11e, f), by reducing the carrier lifetimes via carrier transfer to WS_2.[61] These findings demonstrate 2D perovskite/TMDs heterostructures as promising materials for future spintronic or valleytronic applications.

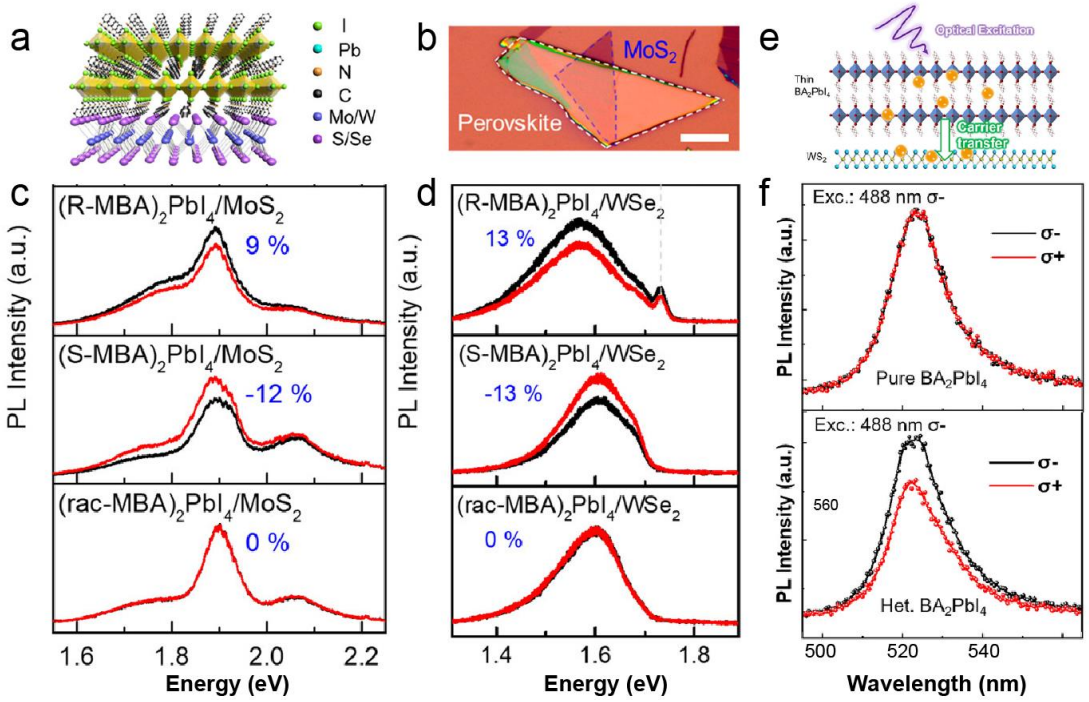

Figure 1.11 Manipulation of valley degree of freedom in 2D perovskite/2D materials van der Waals heterostructures.

(a) Schematic illustration of the chiral $(MBA)_2PbI_4$/monolayer TMD heterostructure. $MBA=C_6H_5C_2H_4NH_3^+$. (b) Representative optical image of a chiral 2D perovskite/MoS_2

heterostructure. Scale bar: 10 μm. (c) Manipulating valley polarization of free excitons of monolayer MoS_2 in chiral 2D perovskite/MoS_2 heterostructure. (d) Manipulating valley polarization of interlayer excitons of monolayer WSe_2 in chiral 2D perovskite/WSe_2 heterostructure. (e) Schematic illustration of the carrier interlayer transportation in thin BA_2PbI_4/monolayer WS_2 heterostructure. BA=$C_4H_9NH_3^+$. (f) Circularly polarized PL spectra of pure BA_2PbI_4 and BA_2PbI_4/monolayer WS_2 heterostructure, respectively.

Since the band structures, band alignments, and interfacial properties can all be designed and realized, it is of great interest to explore high-performance optoelectronic applications based on 2D perovskite/2D materials vdW heterostructures, which combines the merits of the two classes of materials. Previously, 3D perovskite/2D material heterostructures have already demonstrated high performance solar cells and photodetectors[28], due to their highly efficient charge transfer across the interface. The performance may be further improved in 2D perovskite/2D materials heterostructures-based devices, which do not suffer from the existence of the dangling bonds on the surface of 3D perovskite. Moreover, compared to bulk crystals, exfoliated thin 2D perovskites sheets offer better gate dielectrics and conformal adhesion on electrodes, thus mitigating the contact barrier issues faced by thick crystals.

A major bottleneck to application of 2D perovskite-based devices is, however, the high charge injection barrier caused by insulating organic molecules on surfaces of 2D perovskites. To mitigate this effect, Leng et. al found graphene makes good electrical contact to 2D perovskite.[62] Frist, the experimental determined band energy diagrams (Figure 1.12a) show the conduction band of 2D RP n = 4 perovskite is near the Fermi level of graphene (G), which allows electron to flow from G to 2D perovskite with a lower barrier than from Au to 2D perovskite. Secondly, the atomic smoothness of graphene surface renders intimate interaction across the hetero-interface, necessary

for efficient carrier transfer. Lastly, a higher degree of surface crystalline order was also observed in 2D perovskite when interfacing with G compared to Au, which is attributed to the high-quality van der Waals interface. As a result, a much higher current when a positive gate bias is applied is observed in the 2D perovskite/G FET devices than that of 2D perovskite/Au, attaining an ON/OFF ratio of 1.6×10^6 (Figure 1.12b). Ultrafast charge transfer on the order of 50 fs or less was revealed by femtosecond pump-probe spectroscopy (Figure 1.12c). In addition, it is shown that graphene can serve as encapsulation layer and significantly improve the stability of 2D perovskite devices, which shows no degradation after 75 days (Figure 1.12d).[63] These advantages enabled Tan et. al to fabricated high-performance photodetectors based on 2D $(C_4H_9NH_3)_2PbBr_4$ nanosheets with graphene film as top contact and protection (Figure 1.12e,f).[64] Both a high responsivity (~2100 A/W) and extremely low dark current (~ 10^{-10} A) are achieved with a design of interdigital graphene electrodes. These early works demonstrate 2D perovskite/graphene may be enabling platforms for future optoelectronics.

2D perovskite/TMDs heterostructure-based devices have been a direction of intense research interest. Fang et. al reported the fabrication of few-layer MoS_2 (n-type) and lead free 2D perovskite $(PEA)_2SnI_4$ (p-type) heterostructure photodetectors (Figure 1.12i).[65] The heterojunction device is capable of sensing light over the visible and near-infrared wavelength range. Additionally, the device performance could be improved when few-layer graphene flakes are used as electrical contact, and a responsivity of 1100 A/W at 3V bias, a fast response speed of ~ 40 ms under zero bias, and a rectification ratio of 500 are achieved. In addition, the photovoltaic and photodetection performance in monolayer WS_2/2D perovskite $(PEA)_2PbI_4$ vertical heterostructures with type II band alignment also have been reported (Figure 1.12k).[66] The device shows an open-circuit voltage of −0.57 V and a short-circuit current of 41.6 nA (Figure 1.12l), where graphene was also used to

realize good electrical contacts. Without external bias, this device can also work as self-driven photodetector with a photoresponsivity of 24.2 μA/W and an on/off ratio of approximately 1500, as well as an EQE of 5.7×10^{-5}.

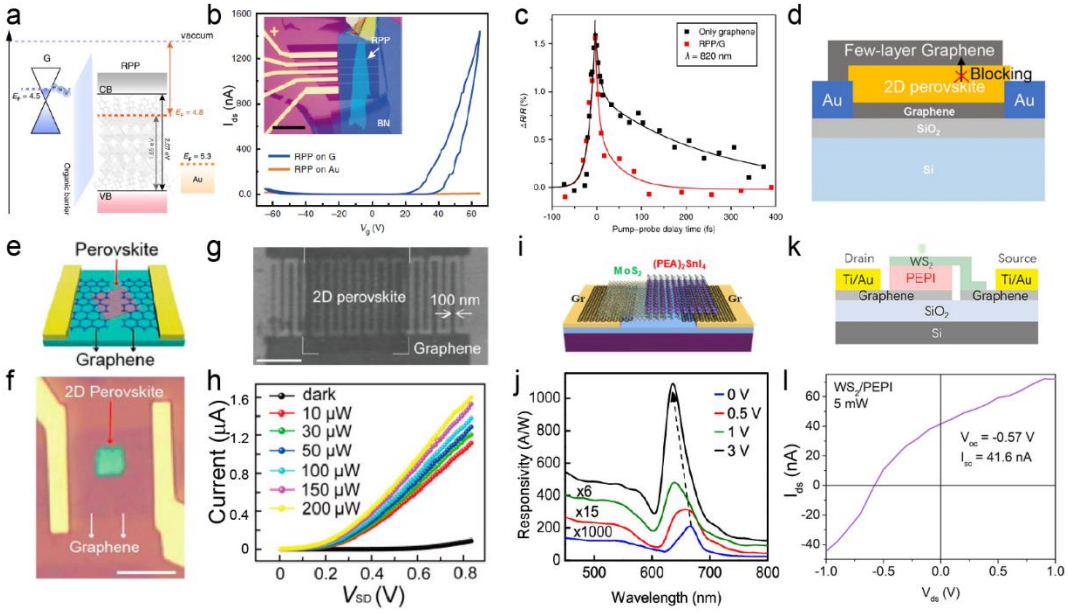

Figure 1.12 2D perovskite/2D materials heterostructure-based devices.

(a) Interfacial energy alignment diagrams of $(BA)_2(MA)_3Pb_4I_{13}$ (RPP), graphene (G) and Au. (b) Transfer characteristics of RPP/G and RPP/Au FET devices at 1.7 K. Inset show an optical image of a typical bilayer thick 2D RPP device using G as electrode. Scale bar: 15 μm. (c) Differential reflectivity spectra of a G (black) and RPP/G (red) probed at 820 nm as a function of pump-probe delay time, when pumping at 25 pJ/μm^2 peak energy density. Solid lines in the graph correspond to fits considering exponential growth (t<0 fs) and decay (t>0 fs) functions. (d) Schematic illustration of a graphene/2D perovskite/graphene device, where 2D perovskite is protected by graphene and show improved stability. (e) Schematic illustration of the 2D $(C_4H_9NH_3)_2PbBr_4$ photodetector with graphene as source-drain top electrode. (f) Optical image for the $(C_4H_9NH_3)_2PbBr_4$ photodetector with graphene electrodes. Scale bar: 10 μm. (g) SEM image of $(C_4H_9NH_3)_2PbBr_4$ photodetector with interdigital graphene electrodes. Scale bar: 1 μm. (h)

Current-voltage (I_{SD}-V_{SD}) curves of the individual device in the dark and under different illumination intensities with a 470 nm defocused laser. (i) Schematic illustration of a graphene/$(PEA)_2SnI_4$/MoS_2/graphene device and (j) its spectral response under different biases. (k) Schematic illustration of the graphene/monolayer WS_2/few-layer PEPI/graphene heterostructure device. (l) Current-voltage (I_{SD}-V_{SD}) curves of the heterostructure device under a 532 nm laser illumination at 5 mW.

1.4.3 Deterministic fabrication of arbitrary vertical heterostructures

Despite the early reports, the fragile nature of halide perovskite materials and the limited lateral dimension make transferring and mechanically stacking of exfoliated 2D RP perovskite thin sheets[21] or those directly grown on substrates[23] much less effective and reliable. Moreover, access to large-area phase-pure $n > 1$ 2D perovskite building blocks is lacking. To address these challenges, our group reported a hybrid approach that allows deterministic fabrication of arbitrary vertical heterostructures of 2D RP lead halide perovskites with different halides, *n* phases, LA and/or A cations. [67]

We first developed a controllable growth strategy for large-area molecularly thin nanosheets of various phase-pure RP perovskites at the solution-air interface. The amphiphilic LA cations self-assemble at the solution-air interface and serve as a soft template that enables highly anisotropic growth (Figure 1.13a). By changing the stochiometric ratios of (LA)X, AX, and PbX_2 in precursor solutions, a diverse library of RP perovskite thin sheets were synthesized (see Figure 1.13b for selective phases). The lateral sizes of the as-grown nanosheets can be up to a few hundred micrometers with thickness down to a monolayer. We further developed a gentle transfer method that allowed us to pick up these floating thin sheets and transfer them onto arbitrary substrates including glass, quartz and Si/SiO_2, via a PDMS-based soft transfer method (Figure 1.14a). Thanks

to the hydrophobic nature of PDMS as well as the soft/compliant character of water droplets and the PDMS film, even though atomically thin perovskites are extremely fragile, the as-transferred sheets remained mostly intact and the surface appeared to be clean, which is essential to achieving the desired heterostructure properties.

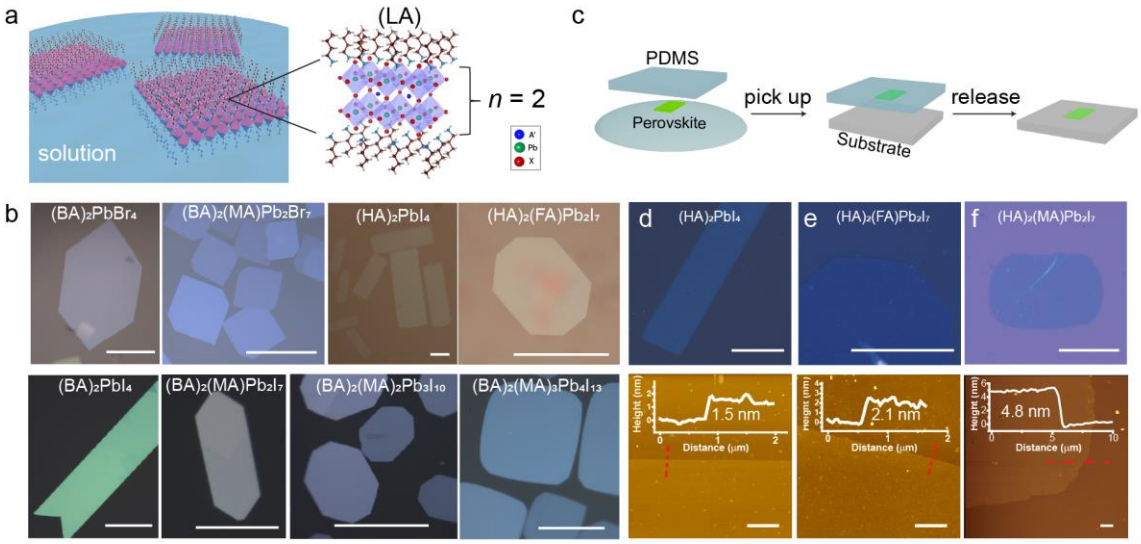

Figure 1.13 Floating growth of large area nanosheets of various phases of 2D RP perovskites. (a) Scheme for the solution floating growth of 2D RP perovskite nanosheets at the solution-air interface, using an example of n = 2 RP perovskite $(LA)_2(A)Pb_2I_7$. (b) Optical images of selective phases of RP perovskite nanosheets (or occasionally nanoribbons) still floating on water surface. All scale bars are 50 μm. (c) Schematic illustration for the process of picking up the floating thin sheets with PDMS and transferring onto other substrates. (d)-(f) Optical images and corresponding AFM images showing representative transferred nanosheets on Si/SiO_2 substrates. Height profiles extracted along the red dotted lines demonstrating the smoothness and the thicknesses down to monolayer or single unit cell. Scale bar for optical images: 25 μm. Scale bar for AFM images: 2 μm.

These diverse large-area thin sheets with atomically clean and sharp surfaces are ideal building blocks for fabrication of vertically stacked heterostructures. We then created a range of

representative vertical heterostructures using different RP perovskites (Figure 1.14a-c), many of which were not accessible previously. In the $(BA)_2PbBr_4/(BA)_2PbI_4$ heterostructure (Figure 1.14a_1). we show that the hetero-interface is sharp and smooth, with no obvious air/water bubble inclusion (Figure 1.14a_2), which was attributed to the soft, compliant and hydrophobic nature of LA ligands at the layer surface. The 2D heterojunction with different halides here are stable for weeks when stored in desiccators at room temperature with negligible ion interdiffusion (Figure 1.14a_3).

The intimate interaction in the stacked van der Waals heterostructure allows emergent interlayer properties to be observed. We demonstrated the fabrication of an unusual tri-layer multi-heterostructure that has shuffled *n*-phases $(BA)_2PbI_4/(BA)_2(MA)_2Pb_3I_{10}/(BA)_2(MA)Pb_2I_7$ (n = 1/ n = 3/n = 2) with well-defined junctions and stacking sequence (Figure 1.15b_1). Confocal PL spectra (Figure 1.14b_2) taken in different regions (i-iv) of the heterostructure marked in Figure 1.15b clearly show a total of three different PL peaks at 520 nm, 575 nm and 618 nm in various combinations, which correspond to the excitonic emissions of n = 1, n = 2, and n = 3 RP phases, respectively. Interestingly, confocal PL mapping on the heterostructure (Figure 1.15b_3-b_5) clearly reveals dramatic changes in the steady-state PL intensities of these three PL peaks in different regions. We attributed such phenomena to energy transfer from the low *n*-phases to high *n*-phases due to the decreasing bandgaps and type-I band alignments[68] following previous reports[69-72] (illustrated in Figure 1.15b_6 inset). These clearly defined multi-heterostructures with full control over the compositions (*n* phase, LA and A cations) and sequences can serve as ideal platforms to study the interlayer carrier dynamics.

We also fabricated a 2D perovskite/monolayer WS_2 heterostructure (Figure 1.14c) to demonstrate our capability to integrate 2D perovskites with other 2D functional materials. The diverse heterostructures configurations are of great interest for future exploration.

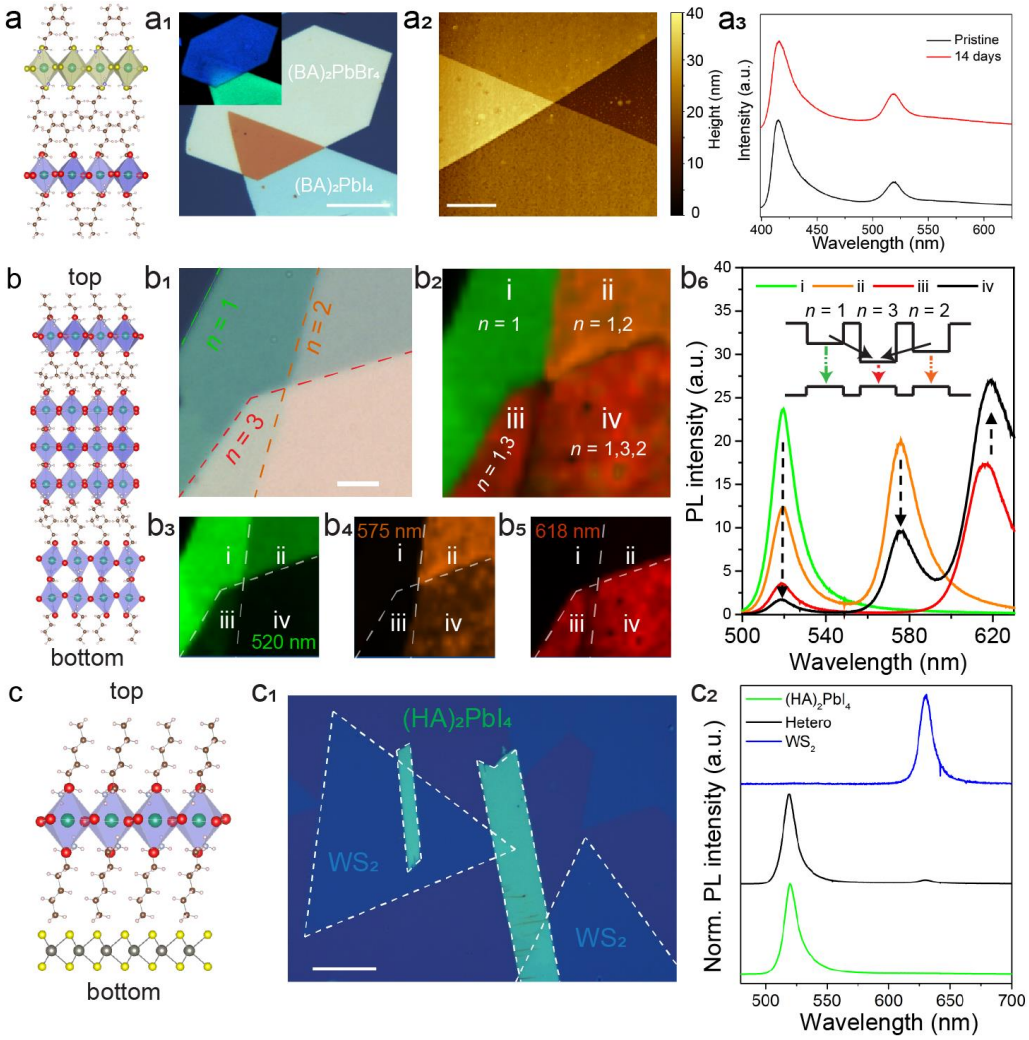

Figure 1.14 Fabrication and characterization of several types of vertical heterostructures of 2D RP perovskite.

(a) Schematic and (a_1) Optical image of a $(BA)_2PbBr_4/(BA)_2PbI_4$ heterostructure on Si/SiO_2 substrate. Inset shows a real-color image of the heterostructure under UV LED excitation. Scale bar: 25 μm. (a_2) AFM image of the heterostructure. Inset shows the 3D height landscape. Scale bar: 2 μm. (a_3) PL spectra of the as-fabricated heterostructure (black) and after 14 days (red). (b) Schematic for a $n = 1/n = 3/n = 2$ multi-heterostructure. (b_1) Optical image of the heterostructure

fabricated on a Si/SiO_2 substrate. Scale bar: 5 μm. (b_2-b_5) PL mappings of this heterostructure: (b_2) Overview mapping image with the four different regions (i-iv) marked together with the *n* phase found in those regions; (b_3) green represents emission integrated from 515 to 525 nm (n = 1); (b_4) orange from 570 to 580 nm (n = 2); (b_5) red from 613 to 623 nm (n = 3). (b_6) Confocal PL spectra collected in the regions labeled as i-iv in (b_2) more clearly show the PL intensity evolution between different single phase (i) and double layer (ii,iii) and triple layer (iv) structures. Inset shows the schematic band energy diagram of the 3 phases illustrating one possible scenario of energy transfer processes among them. (c) Schematic for a $(HA)_2PbI_4/WS_2$ heterostructure. (c_1) Optical image of the heterostructure. Scale bar: 25 μm. (b_2) Confocal PL spectra taken at the $(HA)_2PbI_4$ (green), WS_2 (blue), and heterostructure (black) region, respectively.

1.5 Conclusion and outlook

We summarized the efforts on creation of a variety of halide perovskite heterostructures between different 3D perovskites, between different RP phase perovskites, and between RP phase perovskite and 2D materials. These heterostructures feature various band and alignment and exhibit interesting optical or photophysical properties, and are thus ideal materials platform for studying new physics and fabrication of high-performance optoelectronic devices. We will propose some future research directions of interest, and discuss the challenges remained.

1.5.1 Novel heterostructures configurations

We reviewed the progress on developing lateral heterostructures of 2D RP perovskite with different halides through epitaxial growth or post-synthetic anion exchange. However, many of these junctions are still susceptible to halide interdiffusion which broadens the hetero-interface over time and are not ideal for fundamental studies or practical applications. Fabrication of lateral structures with different *n* numbers is equally interesting, and since the A-cations are much larger

and require more energy to migrate in the lattice, the as-formed heterojunction would likely stay sharp. An obvious challenge for this approach is the potentially large lattice mismatch among the components. This issue may be circumvented, however, by careful selection of component phases in the heterostructure, and creative epitaxial growth designs are needed to realize such idea. For the vertical heterostructures, although arbitrary combination of RP phases can now be made into a heterostructure through our developed synthesis and transfer method[67], the efficiency and throughput of such process is pretty low. It is thus still highly desired to achieve direct synthesis of high-quality RP perovskite heterostructures with control over the composition and morphology, which is rather challenging given the fast crystallization kinetics of halide perovskites and delicate thermodynamic equilibrium among different *n* phases. Special cases may be realized through designing special crystallization sequence that takes advantage the different solubilities of component phases.

Moreover, the research on 2D perovskite-2D materials van der Waals heterostructures is still in its infancy. Most of the work reported so far were based on exfoliated $n = 1$ halide perovskites[54,56,60,61], due to limited access to high-quality $n > 1$ building blocks. The choice of 2D materials in the heterostructure, on the other hand, were limited to graphene and TMDs. In light of the variety of 2D RP perovskite thin sheets recently enabled by our synthesis and large number of available novel layered materials not yet explored (BP, MXenes and MOFs, for example), we expect large amount of novel heterostructures that integrate the inherent electronic characteristics of individual components and exhibit potentially novel functionalities are yet to be discovered and studied.

1.5.2 Studies on carrier transfer and novel physics

Understanding carrier transfer dynamics in semiconductor heterostructures is key to achieving high performance devices and realizing new functionalities. For example, carrier funneling from lower *n* RP phase to higher *n*-phase has been proposed in the mixed-phase thin film devices, which led to improved efficiency in the LEDs[70-72]. However, the junctions in these polycrystalline samples are poorly defined, and the exact RP phase compositions, stacking sequences, and grain orientations are unknown. It is therefore desired to disentangle such effects and investigate the carrier transfer behaviors across vdW heterostructures with sharp interfaces and known crystallographic alignment. Moreover, the diverse organic spacer cations offer an additional independent dimension to tune the carrier transport across different layers, where the length (interlayer distance), dielectric constant (exciton binding energy), HOMO-LUMO levels (conductivity) of the spacer ligands can all be engineered. In addition to energy-transfers, 2D perovskite heterostructures are interesting platforms to study the charge-transfer excitons (interlayer excitons) with electron and hole reside localized in different layers. Although the interlayer exciton has been widely observed and extensively studied in the TMDs heterostructures[6,7], such phenomenon is yet to be observed in halide perovskite heterostructures, partly due to the common type-I band alignment among the different RP phases, unfavorable for the formation of interlayer excitons. In addition, it has been recently predicted that moiré excitons can form in 2D RP perovskite heterostructures[73] with lattice mismatch or rotational misalignment (Figure 1.17d), which degree of freedom has not been explored. Lastly, carriers in the chiral 2D perovskites are inherently spin-polarized.[57-59] By interfacing the chiral 2D perovskite with monolayer TMDs, the valley polarization can be manipulated.[60] Nevertheless, the spin injection process and associated physical mechanism are still under investigation.

1.5.3 Heterostructure device fabrication

Despite the current progress on 2D RP perovskite-based vdW heterostructure devices, one major obstacle that hinders integrated device fabrication is the incompatibility of halide perovskites with current semiconductor fabrication processes, such as electron-beam lithography and photolithography, due to labile nature of the halide perovskites. Only few works have addressed this issue by dry fabrication[74] or using modified lithography conditions.[75] Another issue is the general poor electrical conductivity of 2D RP perovskite in the out-of-plane direction, due to the existence of insulating organic ligands, which could be improved by employing edge contacts[76] or using special types of organic ligands.[24] Lastly, the long-term environmental stability of halide perovskites is still inferior to other 2D materials. Spin-coating polymer layers or encapsulation by h-BN have been shown to greatly improve the stability of perovskite devices[77], but coating large-area film/array of heterostructures is challenging.

In summary, we believe that the future of halide perovskite nanomaterials and heterostructures is bright, and we anticipate that the field will continue to grow on multiple fronts with integrated efforts from chemists, physicists, and engineers to address the challenges.

1.6 References

1 Vrijen, R. *et al.* Electron-spin-resonance transistors for quantum computing in silicon-germanium heterostructures. *Phys Rev A* **62**, doi:ARTN 012306DOI 10.1103/PhysRevA.62.012306 (2000).

2 Ahn, C. H., Rabe, K. M. & Triscone, J. M. Ferroelectricity at the nanoscale: Local polarization in oxide thin films and heterostructures. *Science* **303**, 488-491, doi:DOI 10.1126/science.1092508 (2004).

3 Bernevig, B. A., Hughes, T. L. & Zhang, S. C. Quantum spin Hall effect and topological phase transition in HgTe quantum wells. *Science* **314**, 1757-1761, doi:10.1126/science.1133734 (2006).

4 Novoselov, K. S., Mishchenko, A., Carvalho, A. & Castro Neto, A. H. 2D materials and van der Waals heterostructures. *Science* **353**, aac9439, doi:10.1126/science.aac9439 (2016).

5 Cheng, R. Q., Yin, L., Wang, F., Wang, Z. X. & He, J. Van der Waals integration of 2D atomic crystals for advanced multifunctional devices. *Sci Bull* **64**, 1033-1035, doi:10.1016/j.scib.2019.03.026 (2019).

6 Mak, K. F. & Shan, J. Opportunities and challenges of interlayer exciton control and manipulation. *Nat*

Nanotechnol **13**, 974-976, doi:10.1038/s41565-018-0301-1 (2018).

7 Rivera, P. *et al.* Interlayer valley excitons in heterobilayers of transition metal dichalcogenides. *Nat Nanotechnol* **13**, 1004-1015, doi:10.1038/s41565-018-0193-0 (2018).

8 Urbaszek, B. & Srivastava, A. Materials in flatland twist and shine. *Nature* **567**, 39-40, doi:DOI 10.1038/d41586-019-00704-x (2019).

9 Kojima, A., Teshima, K., Shirai, Y. & Miyasaka, T. Organometal Halide Perovskites as Visible-Light Sensitizers for Photovoltaic Cells. *Journal of the American Chemical Society* **131**, 6050-+, doi:10.1021/ja809598r (2009).

10 Jeong, J. *et al.* Pseudo-halide anion engineering for alpha-FAPbI(3) perovskite solar cells. *Nature*, doi:10.1038/s41586-021-03406-5 (2021).

11 Xing, G. C. *et al.* Low-temperature solution-processed wavelength-tunable perovskites for lasing. *Nat Mater* **13**, 476-480, doi:10.1038/Nmat3911 (2014).

12 Zhu, H. M. *et al.* Lead halide perovskite nanowire lasers with low lasing thresholds and high quality factors. *Nat Mater* **14**, 636-U115, doi:10.1038/Nmat4271 (2015).

13 Dou, L. T. *et al.* Solution-processed hybrid perovskite photodetectors with high detectivity. *Nat Commun* **5**, doi:ARTN 540410.1038/ncomms6404 (2014).

14 Sutherland, B. R. & Sargent, E. H. Perovskite photonic sources. *Nat Photonics* **10**, 295-302, doi:10.1038/Nphoton.2016.62 (2016).

15 Katan, C., Mercier, N. & Even, J. Quantum and Dielectric Confinement Effects in Lower-Dimensional Hybrid Perovskite Semiconductors. *Chem Rev* **119**, 3140-3192, doi:10.1021/acs.chemrev.8b00417 (2019).

16 Charbonneau, S., Thewalt, M. L., Koteles, E. S. & Elman, B. Transformation of spatially direct to spatially indirect excitons in coupled double quantum wells. *Phys Rev B Condens Matter* **38**, 6287-6290, doi:10.1103/physrevb.38.6287 (1988).

17 Golub, J. E., Kash, K., Harbison, J. P. & Florez, L. T. Long-lived spatially indirect excitons in coupled GaAs/AlxGa1-xAs quantum wells. *Phys Rev B Condens Matter* **41**, 8564-8567, doi:10.1103/physrevb.41.8564 (1990).

18 Butov, L. V., Zrenner, A., Abstreiter, G., Bohm, G. & Weimann, G. Condensation of indirect excitons in coupled AlAs/GaAs quantum wells. *Phys Rev Lett* **73**, 304-307, doi:10.1103/PhysRevLett.73.304 (1994).

19 Butov, L. V. *et al.* Stimulated scattering of indirect excitons in coupled quantum wells: signature of a degenerate Bose-gas of excitons. *Phys Rev Lett* **86**, 5608-5611, doi:10.1103/PhysRevLett.86.5608 (2001).

20 Blancon, J. C. *et al.* Scaling law for excitons in 2D perovskite quantum wells. *Nat Commun* **9**, 2254, doi:10.1038/s41467-018-04659-x (2018).

21 Leng, K. *et al.* Molecularly thin two-dimensional hybrid perovskites with tunable optoelectronic

properties due to reversible surface relaxation. *Nat Mater* **17**, 908-914, doi:10.1038/s41563-018-0164-8 (2018).

22 Wang, J. *et al.* Room Temperature Coherently Coupled Exciton-Polaritons in Two-Dimensional Organic-Inorganic Perovskite. *ACS Nano* **12**, 8382-8389, doi:10.1021/acsnano.8b03737 (2018).

23 Dou, L. T. *et al.* Atomically thin two-dimensional organic-inorganic hybrid perovskites. *Science* **349**, 1518-1521, doi:10.1126/science.aac7660 (2015).

24 Gao, Y. *et al.* Molecular engineering of organic-inorganic hybrid perovskites quantum wells. *Nat Chem* **11**, 1151-1157, doi:10.1038/s41557-019-0354-2 (2019).

25 Wang, J. *et al.* Controllable Synthesis of Two-Dimensional Ruddlesden-Popper-Type Perovskite Heterostructures. *J Phys Chem Lett* **8**, 6211-6219, doi:10.1021/acs.jpclett.7b02843 (2017).

26 Wang, J. *et al.* Controllable Growth of Centimeter-Sized 2D Perovskite Heterostructures for Highly Narrow Dual-Band Photodetectors. *ACS Nano* **13**, 5473-5484, doi:10.1021/acsnano.9b00259 (2019).

27 Shewmon, N. T., Yu, H., Constantinou, I., Klump, E. & So, F. Formation of Perovskite Heterostructures by Ion Exchange. *Acs Appl Mater Inter* **8**, 33273-33279, doi:10.1021/acsami.6b10034 (2016).

28 Lei, Y. S. *et al.* A fabrication process for flexible single-crystal perovskite devices. *Nature* **583**, 790-+, doi:10.1038/s41586-020-2526-z (2020).

29 Kennard, R. M. *et al.* Phase Stability and Diffusion in Lateral Heterostructures of Methyl Ammonium Lead Halide Perovskites. *Acs Appl Mater Inter* **11**, 25313-25321, doi:10.1021/acsami.9b06069 (2019).

30 Wang, Y. L. *et al.* Large-Area Synthesis and Patterning of All-Inorganic Lead Halide Perovskite Thin Films and Heterostructures. *Nano Lett* **21**, 1454-1460, doi:10.1021/acs.nanolett.0c04594 (2021).

31 Ren, Y. J. *et al.* Halide Perovskite Lateral Heterostructures for Energy Routing Based Photonic Applications. *Adv Opt Mater* **8**, doi:ARTN 200134710.1002/adom.202001347 (2020).

32 Dou, L. *et al.* Spatially resolved multicolor CsPbX3 nanowire heterojunctions via anion exchange. *P Natl Acad Sci USA* **114**, 7216-7221, doi:10.1073/pnas.1703860114 (2017).

33 Wang, Y. P. *et al.* Epitaxial Halide Perovskite Lateral Double Heterostructure. *Acs Nano* **11**, 3355-3364, doi:10.1021/acsnano.7b00724 (2017).

34 Meloni, S. *et al.* Ionic polarization-induced current-voltage hysteresis in CH3NH3PbX3 perovskite solar cells. *Nat Commun* **7**, doi:ARTN 1033410.1038/ncomms10334 (2016).

35 Li, C. *et al.* Iodine Migration and its Effect on Hysteresis in Perovskite Solar Cells. *Adv Mater* **28**, 2446-2454, doi:10.1002/adma.201503832 (2016).

36 Pan, D. X. *et al.* Visualization and Studies of Ion-Diffusion Kinetics in Cesium Lead Bromide Perovskite Nanowires. *Nano Lett* **18**, 1807-1813, doi:10.1021/acs.nanolett.7b05023 (2018).

37 Gillin, W. P. *et al.* Vacancy Controlled Interdiffusion of the Group-V Sublattice in Strained Ingaas/Ingaasp Quantum-Wells. *Appl Phys Lett* **63**, 797-799, doi:Doi 10.1063/1.109911 (1993).

38 Lai, M. L. *et al.* Intrinsic anion diffusivity in lead halide perovskites is facilitated by a soft lattice. *P Natl Acad Sci USA* **115**, 11929-11934, doi:10.1073/pnas.1812718115 (2018).

39 Zhang, Y. *et al.* Quantitative imaging of anion exchange kinetics in halide perovskites. *P Natl Acad Sci USA* **116**, 12648-12653, doi:10.1073/pnas.1903448116 (2019).

40 Lin, Y. *et al.* Suppressed Ion Migration in Low-Dimensional Perovskites. *Acs Energy Lett* **2**, 1571-1572, doi:10.1021/acsenergylett.7b00442 (2017).

41 Xiao, X. *et al.* Suppressed Ion Migration along the In-Plane Direction in Layered Perovskites. *Acs Energy Lett* **3**, 684-688, doi:10.1021/acsenergylett.8b00047 (2018).

42 Shi, E. Z. *et al.* Two-dimensional halide perovskite lateral epitaxial heterostructures. *Nature* **580**, 614-+, doi:10.1038/s41586-020-2219-7 (2020).

43 Roy, C. R. *et al.* Anion Exchange of Ruddlesden-Popper Lead Halide Perovskites Produces Stable Lateral Heterostructures. *Journal of the American Chemical Society* **143**, 5212-5221, doi:10.1021/jacs.1c01573 (2021).

44 Fu, Y. P. *et al.* Multicolor Heterostructures of Two-Dimensional Layered Halide Perovskites that Show Interlayer Energy Transfer. *Journal of the American Chemical Society* **140**, 15675-15683, doi:10.1021/jacs.8b07843 (2018).

45 Ran, C. X. *et al.* Bilateral Interface Engineering toward Efficient 2D-3D Bulk Heterojunction Tin Halide Lead-Free Perovskite Solar Cells. *Acs Energy Lett* **3**, 713-+, doi:10.1021/acsenergylett.8b00085 (2018).

46 La-Placa, M. G. *et al.* Vacuum-Deposited 2D/3D Perovskite Heterojunctions. *Acs Energy Lett* **4**, 2893-2901, doi:10.1021/acsenergylett.9b02224 (2019).

47 Ye, T. *et al.* Efficient and Ambient-Air-Stable Solar Cell with Highly Oriented 2D@3D Perovskites. *Adv Funct Mater* **28**, doi:ARTN 180165410.1002/adfm.201801654 (2018).

48 Li, P. W. *et al.* Phase Pure 2D Perovskite for High-Performance 2D-3D Heterostructured Perovskite Solar Cells. *Adv Mater* **30**, doi:ARTN 180532310.1002/adma.201805323 (2018).

49 Lee, J. W. *et al.* 2D perovskite stabilized phase-pure formamidinium perovskite solar cells. *Nat Commun* **9**, doi:ARTN 302110.1038/s41467-018-05454-4 (2018).

50 Heo, S. *et al.* Dimensionally Engineered Perovskite Heterostructure for Photovoltaic and Optoelectronic Applications. *Adv Energy Mater* **9**, doi:ARTN 190247010.1002/aenm.201902470 (2019).

51 Chin, X. Y. *et al.* Self-assembled hierarchical nanostructured perovskites enable highly efficient LEDs via an energy cascade. *Energ Environ Sci* **11**, 1770-1778, doi:10.1039/c8ee00293b (2018).

52 Zhou, N. H. *et al.* Distinguishing Energy- and Charge-Transfer Processes in Layered Perovskite Quantum Wells with Two-Dimensional Action Spectroscopies. *J Phys Chem Lett* **11**, 4570-4577, doi:10.1021/acs.jpclett.0c00844 (2020).

53 Kuo, M. Y. *et al.* Distinct Carrier Transport Properties Across Horizontally vs Vertically Oriented Heterostructures of 2D/3D Perovskites. *Journal of the American Chemical Society* **143**, 4969-4978, doi:10.1021/jacs.0c10000 (2021).

54 Yang, A. *et al.* Giant Enhancement of Photoluminescence Emission in WS2-Two-Dimensional Perovskite Heterostructures. *Nano Lett* **19**, 4852-4860, doi:10.1021/acs.nanolett.8b05105 (2019).

55 Zhang, Q., Linardy, E., Wang, X. Y. & Eda, G. Excitonic Energy Transfer in Heterostructures of Quasi-2D Perovskite and Monolayer WS2. *Acs Nano* **14**, 11482-11489, doi:10.1021/acsnano.0c03893 (2020).

56 Chen, Y. Y. *et al.* Robust Interlayer Coupling in Two-Dimensional Perovskite/Monolayer Transition Metal Dichalcogenide Heterostructures. *Acs Nano* **14**, 10258-10264, doi:10.1021/acsnano.0c03624 (2020).

57 Ahn, J. *et al.* A new class of chiral semiconductors: chiral-organic-molecule-incorporating organic-inorganic hybrid perovskites. *Mater Horiz* **4**, 851-856, doi:10.1039/c7mh00197e (2017).

58 Long, G. K. *et al.* Spin control in reduced-dimensional chiral perovskites. *Nat Photonics* **12**, 528-+ (2018).

59 Ma, J. Q. *et al.* Chiral 2D Perovskites with a High Degree of Circularly Polarized Photoluminescence. *Acs Nano* **13**, 3659-3665 (2019).

60 Chen, Y. Y. *et al.* Manipulation of Valley Pseudospin by Selective Spin Injection in Chiral Two-Dimensional Perovskite/Monolayer Transition Metal Dichalcogenide Heterostructures. *Acs Nano* **14**, 15154-15160, doi:10.1021/acsnano.0c05343 (2020).

61 Huang, L. Y. *et al.* Enhancing circular polarization of photoluminescence of two-dimensional Ruddlesden-Popper perovskites by constructing van der Waals heterostructures. *Appl Phys Lett* **119**, doi:Artn 151101
10.1063/5.0062979 (2021).

62 Leng, K. *et al.* Electron tunneling at the molecularly thin 2D perovskite and graphene van der Waals interface. *Nat Commun* **11**, doi:ARTN 548310.1038/s41467-020-19331-6 (2020).

63 Zhao, L. F. *et al.* Ultrasensitive Heterojunctions of Graphene and 2D Perovskites Reveal Spontaneous Iodide Loss. *Joule* **2**, 2133-2144, doi:10.1016/j.joule.2018.07.011 (2018).

64 Tan, Z. J. *et al.* Two-Dimensional (C4H9NH3)(2)PbBr4 Perovskite Crystals for High-Performance Photodetector. *Journal of the American Chemical Society* **138**, 16612-16615, doi:10.1021/jacs.6b11683 (2016).

65 Fang, C. *et al.* High-Performance Photodetectors Based on Lead-Free 2D Ruddlesden-Popper Perovskite/MoS2 Heterostructures. *Acs Appl Mater Inter* **11**, 8419-8427, doi:10.1021/acsami.8b20538 (2019).

66 Wang, Q. X. *et al.* Optoelectronic Properties of a van der Waals WS2 Monolayer/2D Perovskite Vertical Heterostructure. *Acs Appl Mater Inter* **12**, 45235-45242, doi:10.1021/acsami.0c14398 (2020).

67 Pan, D. X. *et al.* Deterministic fabrication of arbitrary vertical heterostructures of two-dimensional Ruddlesden-Popper halide perovskites. *Nature Nanotechnology* **16**, 159-+, doi:10.1038/s41565-020-00802-2 (2021).

68 Spanopoulos, I. *et al.* Uniaxial Expansion of the 2D Ruddlesden-Popper Perovskite Family for Improved Environmental Stability. *J Am Chem Soc* **141**, 5518-5534, doi:10.1021/jacs.9b01327 (2019).

69 Fu, Y. *et al.* Multicolor Heterostructures of Two-Dimensional Layered Halide Perovskites that Show

Interlayer Energy Transfer. *J Am Chem Soc* **140**, 15675-15683, doi:10.1021/jacs.8b07843 (2018).

70 Yuan, M. *et al.* Perovskite energy funnels for efficient light-emitting diodes. *Nat Nanotechnol* **11**, 872-877, doi:10.1038/nnano.2016.110 (2016).

71 Proppe, A. H. *et al.* Synthetic Control over Quantum Well Width Distribution and Carrier Migration in Low-Dimensional Perovskite Photovoltaics. *J Am Chem Soc* **140**, 2890-2896, doi:10.1021/jacs.7b12551 (2018).

72 Wang, N. N. *et al.* Perovskite light-emitting diodes based on solution-processed self-organized multiple quantum wells. *Nat Photonics* **10**, 699-+, doi:10.1038/Nphoton.2016.185 (2016).

73 Zhang, L. H., Zhang, X. & Lu, G. Predictions of moire excitons in twisted two-dimensional organic-inorganic halide perovskites. *Chem Sci* **12**, 6073-6080, doi:10.1039/d1sc00359c (2021).

74 Liu, Y. *et al.* Approaching the Schottky-Mott limit in van der Waals metal-semiconductor junctions. *Nature* **557**, 696-+, doi:10.1038/s41586-018-0129-8 (2018).

75 Lin, C. H. *et al.* Orthogonal Lithography for Halide Perovskite Optoelectronic Nanodevices. *Acs Nano* **13**, 1168-1176, doi:10.1021/acsnano.8b05859 (2019).

76 Wang, L. *et al.* One-Dimensional Electrical Contact to a Two-Dimensional Material. *Science* **342**, 614-617, doi:10.1126/science.1244358 (2013).

77 Leng, K. *et al.* Molecularly thin two-dimensional hybrid perovskites with tunable optoelectronic properties due to reversible surface relaxation. *Nat Mater* **17**, 908-+, doi:10.1038/s41563-018-0164-8 (2018).

Chapter 2 Visualization and Studies of Ion Diffusion Kinetics in Cesium Lead Bromide Perovskite Nanowires[1]

2.1 Abstract

The facile chemical transformation of metal halide perovskites via ion exchange has been attributed to their "soft" crystal lattices that enable fast ion migration. Kinetic studies of such processes could provide mechanistic insights on the ion migration dynamics. Herein, by using aligned single-crystal nanowires of cesium lead bromide ($CsPbBr_3$) perovskite on epitaxial substrates as platforms, we carry out visualization and investigation of the cation or anion interdiffusion kinetics via spatially resolved photoluminescence measurement on heterostructures fabricated by stacking $CsPbCl_3$, $MAPbI_3$, or $MAPbBr_3$ microplates on top of $CsPbBr_3$ nanowires. Time-dependent confocal photoluminescence microscopy and energy-dispersive X-ray spectroscopy showed the solid-state anion interdiffusion can readily occur to result in halide concentration gradients along $CsPbBr_{3-3x}Cl_{3x}$ (x = 0-1) nanowires. Quantitative analysis of such composition profiles using Fick's law allowed us, for the first time, to extract interdiffusion coefficients of the chloride-bromide couple and an activation energy of 0.44 ± 0.02 eV for ion diffusion from temperature-dependent studies. In contrast, iodide-bromide interdiffusion is limited, likely due to the complex phase behaviors of mixed alloys of $CsPb(Br,I)_3$. In contrast to the relatively mobile anions, A-site cation interdiffusion across the $MAPbBr_3/CsPbBr_3$ junctions was barely observed at room temperature. Our results present a general method to investigate the kinetics of the solid-state ion migration, and the gained insights on ion diffusion can provide

[1] This chapter was originally published in *Nano Lett.*, **2018**, 18(3), 1807-1813, in collaboration with Y. Fu, J. Chen, K. J. Czech, J. C. Wright, and S. Jin

guidelines for rationally designing perovskite heterostructures that could lead to new properties for fundamental studies and technological applications.

2.2 Introduction

Lead halide perovskites [$APbX_3$, A is a monovalent cation, *e.g.* methylammonium (MA), formamidinium (FA), Cs^+, X is a halide anion] are excellent semiconductors for high performance photovoltaic and optoelectronic devices due to their superior photophysical properties.[1-8] Furthermore, they can be easily processed in solution, which could enable the production of low-cost optoelectronic devices for large-scale applications. However, the low energy barrier for crystal formation that enables the facile solution synthesis also results in a soft and dynamic crystal lattice, and consequently poor chemical and structural stability.[9, 10] This characteristic makes it easy for the ions in the perovskite lattice to move around, which has been utilized in post-synthetic composition tuning via ion exchange in both nanostructures[11-14] and bulk thin films.[15, 16] In fact, metal halide perovskites have been known as ionic conductors for over 30 years,[17, 18] but ion migration had not received much attention until the reports of several abnormal phenomena that are likely associated with ion motions. These phenomena include abnormal hysteresis of the current-voltage curves observed in various perovskite solar cells,[19-22] slow electrical response in the photoconductivity measurements of $CH_3NH_3PbI_3$,[23, 24] a reversible photo-induced halide segregation in mixed halide $CH_3NH_3Pb(Br, I)_3$ perovskite film,[25] and a giant switchable photovoltaic effect.[26]

Despite the recognized need to understand the impacts of ion migration on perovskite-based devices, there have been limited approaches and few reports to experimentally study this process. Previous experimental studies on the ion migration mostly relied on electrical measurements, such as current-voltage measurements,[22, 27] conductivity measurements,[28, 29] and photocurrent relaxation

measurements.[30] These indirect measurements revealed the "net" migration result of both cations and anions in the lattice and are dependent on the device architecture and sampling,[31] thus the identification of the actual moving species and the interpretation of the activation energy obtained remained ambiguous and sometimes even controversial.[32, 33] Moreover, the dominance of surface and grain boundaries in these thin film samples on the ion migration[34, 35] may present additional complexity to the correlation of experimental results (i.e. activation energies) obtained from different polycrystalline samples to theoretical predictions[22, 30, 36] that only take bulk point defects into account. There have also been kinetic studies of anion exchange on $CsPbX_3$ colloidal nanocrystals,[37] but it revealed the exchange kinetics at the solution-solid interface, which is slightly different from the solid-state ion exchange process in solid-state devices. Direct kinetic studies of solid-state ionic (anions or cations) exchange or diffusion would provide new insights on the ion migration dynamic in perovskite materials.

Recently, there have been significant advances in the synthesis and applications of single-crystal nanowires (NWs) of halide perovskites with different compositions and optical properties[3, 12, 38-43] Compared with the colloidal nanocrystals and commonly studied thin films, aligned single-crystal $CsPbX_3$ NWs grown on epitaxial substrates[39] stand out as ideal platforms to study the kinetics of solid-state ion exchange. First, the unique one-dimensional (1D) geometry provides directional channels for ion migration and allows much simpler modeling. Second, the strong photoluminescence (PL) of all perovskite compositions enables direct visualization of the ion movement through PL measurement. Last, single-crystal NWs are free of grain boundaries that may present complications to the understanding of the diffusion process and distort the diffusion characteristics acquired. Herein, we demonstrated the direct visualization of the fast solid-state bromide-chloride interdiffusion process along single-crystal $CsPbX_3$ NWs by monitoring the time-

dependent spatially resolved PL emission due to perovskite composition gradients. By modeling the composition distribution profiles based on the Fick's law, we determined a bromide-chloride interdiffusion coefficient of ~10^{-13} cm^2 s^{-1} at room temperature (RT) and further extracted an activation energy of 0.44 ± 0.02 eV based on temperature-dependent studies. However, similar studies revealed a limited extent of iodine-bromine interdiffusion likely due to the limited miscibility of $CsPbBr_3$ and $CsPbI_3$ perovskites. In contrast to the fast anion interdiffusion, A-site cation interdiffusion between $MAPbBr_3$/$CsPbBr_3$ was also observed but with a much slower rate, indicating a higher cation migration activation energy.

2.3 Material synthesis

All chemicals and regents were purchased from Sigma-Aldrich and used as received unless noted otherwise. The F-doped phlogopite mica substrates [chemical formulae: $KMg_3(AlSi_3O_{10})F_2$] were purchased from Taiyuan Fluorphlogopite Mica Company Ltd., Changchun City, P. R. China.

2.3.1 Synthesis of $CsPbBr_3$ nanowires

The synthesis of $CsPbBr_3$ nanowires (NWs) followed our previous report with a few modifications. Specifically, ground powers of 10 mmol CsBr and 10 mmol $PbBr_2$ were loaded in a quartz boat placed at the center of the heating zone of a Lindberg Blue M tube furnace in a home-built chemical vapor deposition (CVD) system (see Figure 2.1). The F-doped phlogopite mica substrate was placed downstream at the cooling zone. The reaction was then carried out at 345 ℃ for 45 min at 80 mTorr with 18 sccm Argon gas flow. Then the furnace was cooled down naturally.

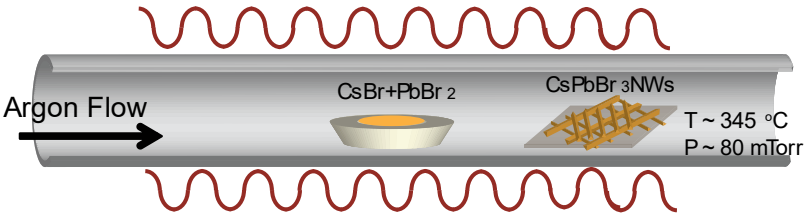

Figure 2.1 Schematic of the vapor-phase epitaxial growth of CsPbBr3 NWs using a home-built CVD system

2.3.2 Synthesis of $CsPbCl_3$ nanoplates

To synthesize $CsPbCl_3$ nanoplates, 200 mg/mL $PbCl_2$ solution in dimethyl sufoxide and 100 mg/mL $PbAc_2{\cdot}3H_2O$ solution in methanol were sequentially drop-casted onto a glass slide. The coated substrate was then annealed at 65 ℃ in an oven for 45 min before it was immersed into a 10 mg/mL CsCl solution in methanol with the lead precursor facing down. The reaction was allowed for 2 days in the oven at 50 ℃ before the glass substrate covered with the $CsPbCl_3$ nanoplate product was removed and washed with methanol and blow dried with N_2 gas.

2.3.3 Synthesis of $CH_3NH_3PbX_3$ ($MAPbX_3$, X=I, Br) nanoplates

We first prepared $PbAc_2$ thin film by dropcasting a 100 mg/mL $PbAc_2{\cdot}3H_2O$ solution in methanol onto a glass slide. The coated substrate was then annealed at 65 ℃ in an oven for 45 min before it was immersed in a 5 mg/mL MABr or 40 mg/mL MAI solution in isopropanol (IPA) at room temperature for 2 days to form nanoplates of $MAPbBr_3$ and $MAPbI_3$, respectively, on the glass substrates. The glass substrates were then removed and washed with IPA and blow dried with N_2 gas. These nanoplates were transferred on top of the $CsPbBr_3$ NWs by directly contacting the mica substrate face-to-face with the glass slide.

2.4 Structural and spectroscopic characterization

The optical images of the perovskite nanostructures were obtained on an Olympus BX51M optical microscope. The scanning electron microscopy (SEM) images were collected on a LEO

SUPRA 55 VP field-emission scanning electron microscope operated at 3 kV. Energy dispersive X-ray spectroscopy (EDS) and EDS analysis were performed using a LEO SUPRA 55 VP field-emission SEM equipped with an EDS detector operating at 10.0 kV.

The true-color optical images were taken using a home-built system. Specifically, excitation pulses of 400 nm were created by second harmonic generation of a Ti:Sapphire oscillator (Coherent Vitesse 800-2) output. The collimated 400 nm pulse was focused through the back side of the mica substrate and the resulting Perovskite PL was collected with a 100x plan apochromatic objective lens (Olympus MPLAPON100X). All excitations were widefield in nature, with a 200 μm beam diameter. PL images were spectrally resolved with an imaging spectrograph (Acton SP-2300i), utilizing a 150 groove/mm reflective grating and an imaging array (Andor Neo 5.5 sCMOS). The photoluminescence (PL) spectra and mapping data were collected using the line scan function of an Aramis Confocal Raman Microscope using a 442 nm laser source. The spatial resolution was ~1 μm.

The temperature-dependent experiments were carried out by heating the samples on a hot plate after transferring the source microplates to NW network for different time periods. And the reaction was quenched by removing the substrates (mica) from the hot plate and the samples were then characterized.

2.5 Results and Discussion

We fabricated perovskite heterostructures by physically stacking single-crystal $CsPbCl_3$, $MAPbBr_3$, or $MAPbI_3$ microplates on single-crystal $CsPbBr_3$ NWs (see Figure 2.2A, B for an example of $CsPbCl_3/CsPbBr_3$). These heterostructures were then used as model systems to study the solid-state ion exchange kinetic by monitoring the optical properties via PL mapping. These aligned $CsPbBr_3$ NWs were grown epitaxially on fluorinated-mica substrates via physical vapor

deposition[39] and the $CsPbCl_3$ or $MAPbBr_3$ or $MAPbI_3$ microplates were synthesized via solution-based approaches reported by our group previously[3, 12]. These $CsPbBr_3$ NWs were grown along the (001) direction of cubic perovskite structure on mica substrates, forming a NW network (Figure 2.2B). They typically have a width of several hundred nanometers to ~ 1 μm and a length up to a few hundred micrometers. Such unique 1D geometry with precise crystallographic orientation makes them ideal platforms to track and quantify the ion diffusion on a microscopic scale, when in contact with another perovskite with different cations or anions. The free-standing solution grown microplates of $CsPbCl_3$, $MAPbBr_3$, $MAPbI_3$ are typically of tens of micrometers in lateral dimension, and a few micrometers in thickness (Figure A1.1 in the appendix). These microplates can be easily transferred on top of the $CsPbBr_3$ NWs by directly face-to-face contacting the two substrates.

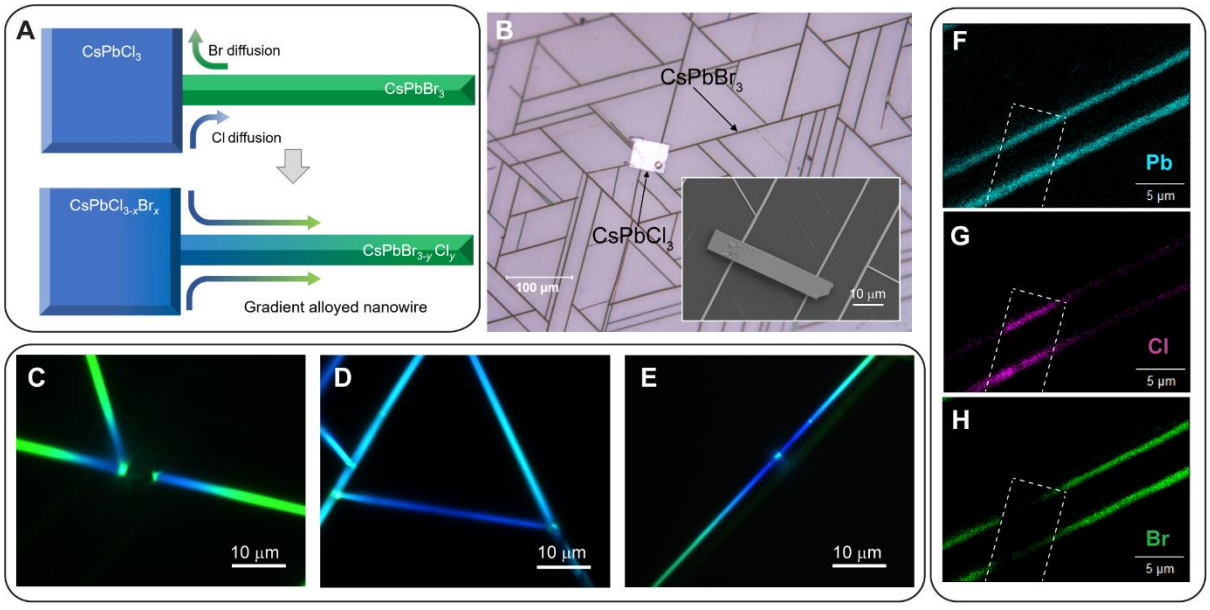

Figure 2.2 Evidence of anion interdiffusion in $CsPbBr_3$/$CsPbCl_3$

(A) Schematic of the perovskite heterostructure fabricated by stacking $CsPbCl_3$ microplate on $CsPbBr_3$ NW for solid-state ion interdiffusion study. Because of complete miscibility of the two compounds, thermodynamically favored interfacial halide exchange reaction between the

microplate and NW occurs, followed by axial chloride/bromide interdiffusion along the NW driven by concentration gradient, leading to the formation of gradient NWs. (B) Optical image and SEM image (inset) of representative heterostructures of a $CsPbCl_3$ microplate placed over $CsPbBr_3$ NW networks. (C, D, E) Representative optical images of the Cl-Br gradient NWs formed by ion diffusion under 400 nm laser excitation. The emission is in real color. (F, G, H) SEM-EDS mappings of the gradient NWs show the spatial elemental distribution of Pb, Br, and Cl, respectively. The dashed rectangular boxes denote the original location of the removed $CsPbCl_3$ microplate.

We first studied the chloride-bromide interdiffusion in $CsPbCl_3$/$CsPbBr_3$ systems. Figure 2.2B shows an optical image of an as-fabricated $CsPbCl_3$/$CsPbBr_3$ heterostructure. A representative scanning electron microscopy (SEM) image (Figure 2.2B inset) confirms the solid physical contact between the two objects, which ensures the solid-state alloying to proceed by continuously feeding Cl^- ions into the $CsPbBr_3$ NW. After a certain reaction time, we found that heterojunctions with gradient halide composition were readily formed. Under broad illumination of a 400 nm pulsed laser, the NWs in contact with $CsPbCl_3$ exhibited spatially distributed multicolor emission from deep blue to cyan then to green color (Figure 2.2C-E), suggesting a gradient halide composition ($CsPbBr_{3-3x}Cl_{3x}$, x = 0-1). The blue and green emissions come from the Cl-rich regions and Br-rich regions, respectively, because Cl incorporation increases the bandgap of the $CsPbBr_{3-3x}Cl_3$ alloys. The PL intensity decreases as the emission becomes more blue-shifted due to the lower PL quantum yield of the Cl-rich composition. The length of the color transition (or composition gradient) region could be tuned from a few to tens of micrometers, depending on the reaction temperature and the reaction time (as will be discussed later). We further employed energy-dispersive spectroscopy (EDS) analysis to confirm the gradient Cl/Br ratio from the regions

contacted with $CsPbCl_3$ to the ends of the $CsPbBr_3$ NW (Figure 2.2F-H). A clear trend of decreasing Cl concentration (Figure 2.2G) and corresponding increasing Br concentration (Figure 2.2H) were observed near the contacting region, while Pb concentration retained uniform across the whole NW (Figure 2.2F). Note that the $CsPbCl_3$ microplate was originally located at the position marked by the white dashed box, but was blown away by electron beam before the EDS measurement. These results show that the anion interdiffuion across the perovskite heterojunction can readily occur even at RT due to the remarkably high diffusivity of the halide ions.

Before performing quantitative analysis of the ion exchange kinetics, it is necessary to discuss the underlying mechanism(s) for ion exchange. We believe the bromide-chloride anion exchange reaction takes place through the following mechanism: a "reaction zone" is first formed at the interface between $CsPbCl_3$ microplate and $CsPbBr_3$ NW, where fast ion exchange between the two objects happens because the abrupt halide concentration difference. Once the reaction zone is formed, the anion exchange reaction would proceed along the NW toward the remaining unexchanged segment of the NW via solid-state ion diffusion of both Cl^- and Br^- ions in the opposite directions. Such mechanism is analogous to that of the extensively studied cation interdiffusions in transition metal chalcogenides[44-46] or oxides.[47-49] On the atomistic level, the solid-state ion diffusion probably occurs through a vacancy-assisted diffusion mechanism, as is supported by several recent works[30, 36, 50] that reported very low formation energy and high concentration of intrinsic vacancies in halide perovskites. Moreover, because $CsPbBr_3$ and $CsPbCl_3$ are completely miscible,[51] the concentration gradient will keep driving the diffusion reaction, as is favored by entropic gain, until the system reaches equilibrium (i.e. evenly mixed anions). Kinetically, as the replacement of halide anion is very fast, this solid-state ion exchange reaction can be treated as a diffusion-controlled reaction, i.e. the ion diffusion is the rate-limiting

step. Therefore, by modeling the reaction dynamics in real time, we can quantify the kinetics to determine the ion interdiffusion coefficient and activation energy.

The strong photoluminescence of the perovskite NWs throughout the exchange reaction allows us to spatially resolve the structural transformation via PL imaging in real time. Figure 2.3A shows a set of evolving PL images of gradient $CsPbBr_{3-3x}Cl_{3x}$ NWs captured at different exchange times at 200 °C. Here we only took the time during heating into account for the reaction time since the diffusion at RT is relatively slow and negligible, as will be shown later. The evolution of emission color provided a direct visualization of the changing halide composition and it can be correlated with the spatial change of halide composition. After a reaction time of 5 min, a significant amount of chloride ions has diffused into the NWs, as evidenced by the appearance of blue emission in the NWs close to the $CsPbCl_3$ microplate. The blue emission continuously propagates along the NW as reaction time increases, and within 25 min the blue emission has reached as far as 10 μm away from the initial contact region (Figure A1.2). By tracking the front of the Cl^- diffusion, namely the distance at which the PL emission peak of the NW retained 525 nm (i.e. pure $CsPbBr_3$), we found the diffusion length (L) is linearly correlated with the square root of reaction time (t) ($L \propto \sqrt{t}$, Figure 2.3B). Such kinetic behaviors are consistent with the diffusion theories involving a constant diffusion coefficient.[52]

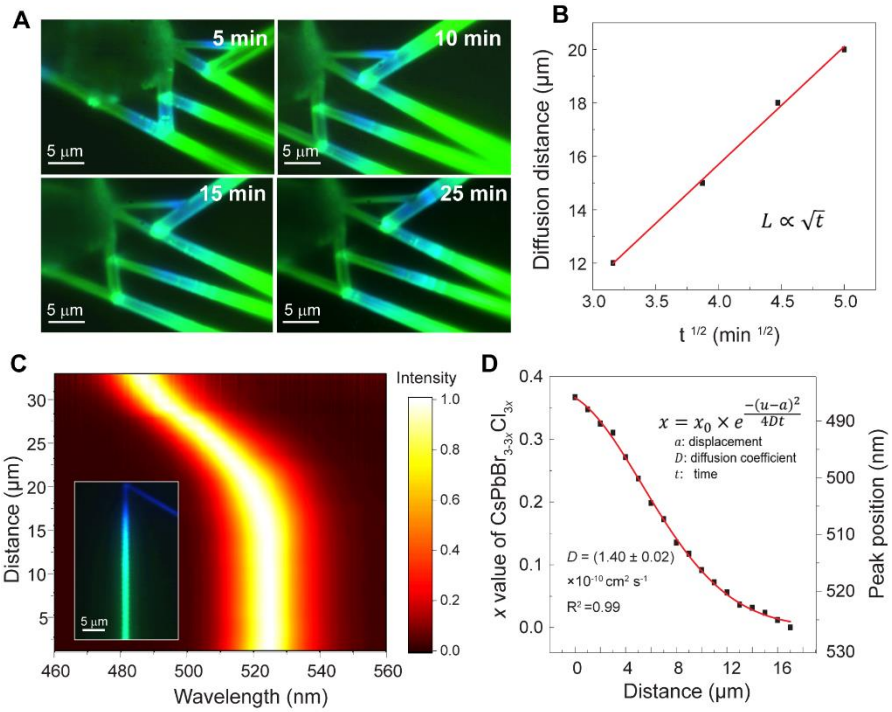

Figure 2.3 Temporal evolution of anion diffusion and the resulting composition distribution profile analysis in $CsPbBr_{3-3x}Cl_{3x}$ NWs

(A) A set of time-dependent PL images of $CsPbCl_3/CsPbBr_3$ heterostructures showing the evolution of anion interdiffusion. (B) Plot and fitting of diffusion length against square root of reaction time ($t^{1/2}$). (C) Normalized PL line mapping of a gradient $CsPbBr_{3-3x}Cl_{3x}$ NW. The y-axis shows the distance from the edge of the $CsPbCl_3$ microplate. The inset is a real-color PL image of the NW under broad laser excitation. (D) Compositions and PL peak positions as a function of distance (black dots) of the corresponding NW, together with the kinetic fitting of the composition-distance profile using 1D diffusion equation (red curve).

We then quantified the reaction dynamics during the exchange reactions by examining the composition profiles extracted from PL mapping using a confocal micro-PL setup. Specifically, the NW of interest was locally excited by a 442 nm laser along the axial direction of the NW at 1 μm intervals, and a series of PL spectra of the corresponding spots were then collected to construct a line mapping spectrum. Figure 2.3C shows a representative 2D pseudo-color plot of the PL

spectra of a transformed NW with a reaction time of 30 min at 200 °C. The y-axis in the plot denotes the distance away from the edge of the $CsPbCl_3$ microplate, i.e. the effective starting point of the ion diffusion. The intensity of each PL spectrum was locally normalized. The PL peak position gradually shifts from ~485 nm to ~525 nm as the excitation spot moves away from the $CsPbCl_3$ microplate, which correlates well with the evolution of real emission color of the corresponding NW (see inset in Figure 2.3C). The local PL peak positions were then converted to the compositions at each point by assuming a linear Vegard's law approximation of the bandgap-composition relationship. After this conversion a half Gaussian-like curve of the composition versus diffusion distance plot can be obtained (Figure 2.3D). The composition profile can be well described by the Fick's second law[53]:

$$\frac{\partial c(x,t)}{\partial t} = D\frac{\partial^2 c(x,t)}{\partial x^2}$$

where D is the interdiffusion coefficient of the diffusion couple, which was assumed to be independent of concentration, and $c(x,t)$ is the percent concentration of Cl^- at the position x (the distance from the effective center of the diffusion) and time t (the time since the start of heating). By applying appropriate boundary conditions in the fitting (see Appendix), we obtained a bromide-chloride interdiffusion coefficient of 1.40×10^{-10} $cm^2\,s^{-1}$ at 200 °C. The good fitting in turn supports that the bromide-chloride exchange reaction indeed follows a diffusion-limiting mechanism and the associated diffusion model. In fact, similar simulation models based on Fick's law have been developed to study much slower ion interdiffusion in other material systems, such as compound III-V semiconductors,[54, 55] and metal oxides.[48, 56]

Having established the diffusion model for extracting the interdiffusion coefficients, we then turned to find the activation energy barrier for the diffusion by temperature-dependent

measurements. Figure 2.4A and 2.4B show two representative results of the diffusion kinetics and the associated fittings at RT and 150 °C, respectively. The average interdiffusion coefficient at RT is found to be (2.1±1.2) × 10^{-13} cm^2 s^{-1}. At each temperature, we examined 5 NW samples (the full data for all temperatures are tabulated in Table A1 in the Appendix) and the average diffusion coefficients are also summarized in the inset table of Figure 2.4C. The diffusion coefficient decreases nearly three orders of magnitude from 200 °C to 25 °C, hence the extremely long reaction time of 50 h at RT as shown in Figure 2.4A. Because the ion diffusion in halide perovskites follows the vacancy-assisted mechanism,[30, 36, 50] the diffusion coefficient can be expressed by the Arrhenius equation:

$$D = D_0 \exp(E_a / k_b T)$$

where E_a is the activation energy for the vacancy-assisted ion migration, k_b is the Boltzmann constant, D_0 is a constant, and T is the temperature. By fitting the plot of ln(D) versus 1/T (Figure 2.4C), an activation energy of (0.44 ± 0.02) eV was obtained. This value is significant lower than the activation energy required for the ion diffusion in classic III-V semiconductors (e.g. 3.0 eV for $In_xGa_{1-x}As$/GaAs at 900 – 1150 °C[55]), confirming relatively soft crystal lattice of halide perovskites. Such a huge difference also explains why chemical transformation in the halide perovskite nanocrystals usually results in homogeneous alloys even at low temperatures, but it leads to the formation of core-shell structures in other semiconductor nanostructures.[44] Moreover, the activation energy here is larger than the previously reported value (0.33 ± 0.01 eV) extracted from liquid-solid chloride-bromide ion exchange reaction in colloidal nanocrystals.[37] In addition the difference of liquid-solid there vs. solid-solid ion exchange herein, this difference may also be due to the even higher surface-to-volume ratio of the nanocrystals that provide more defects and further

facilitate the exchange reaction. Last but not least, this activation energy value falls in the same magnitude of the values reported for the self-diffusion of halide ions in both $CsPbX_3$ and $MAPbX_3$ perovskites,[22, 30, 32] which may suggest that the mechanisms involved in self-diffusion of halide ions and interdiffusion of halide couples are closely related.

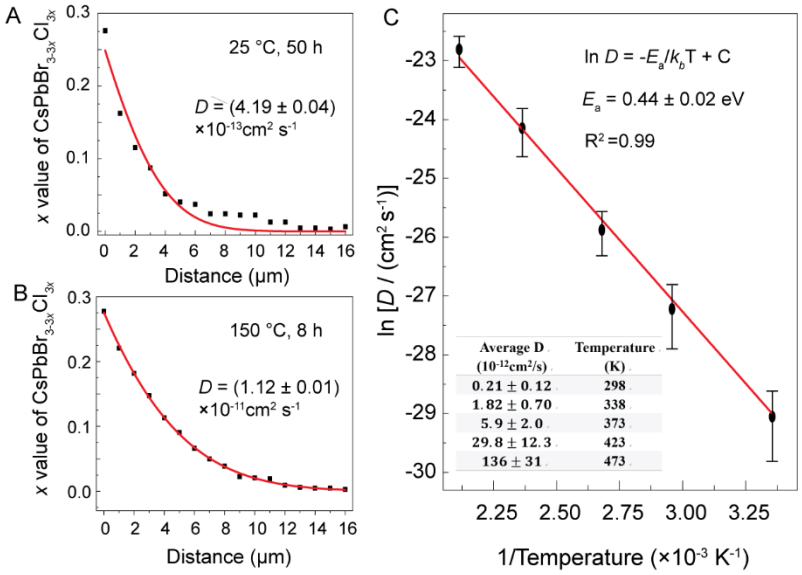

Figure 2.4 Determination of the activation energy for ion diffusion from temperature dependent experiments of $CsPbBr_{3-3x}Cl_{3x}$ NWs.

Composition profiles and kinetic fittings of the anion exchange reactions at (A) 25 °C for 50 h and (B) 150 °C for 8 h. (C) Plot of ln (*D*) versus 1/*T* and the corresponding fitting using Arrhenius equation. The average diffusion coefficients at different temperatures are summarized in the inset table. The error bars of D indicate the standard deviation of the 5 examined samples for each temperature, while the error of E_a comes from fitting.

We also examined the anion interdiffusion dynamics between $CsPbBr_3$ and $MAPbI_3$ and observed only marginal extent of bromide-iodide interdiffusion. We chose $MAPbI_3$ instead of $CsPbI_3$ microplates as the iodine source because the latter is known to undergo fast phase transition from perovskite polymorph to the non-perovskite phase at RT[12]. The cation interdiffusion is

negligible, as will be shown later. After as long as 10 days of exchange reaction at RT, the diffusion of iodide into the $CsPbBr_3$ NW can be observed, as shown by the slightly red-shifted emission of a transformed NW (Figure 2.5A, 2.5C, and 2.5D). However, the maximum peak shift was only ~ 9 nm (corresponding to an estimated ~ 5.4% iodide in molar ratio) at the segment of the $CsPbBr_3$ NW closest to the $MAPbI_3$ microplate, with no further development within the time investigated**.** This is probably due to the complex phase diagram of $CsPb(Br, I)_3$. First, previous experimental and theoretical studies have suggested a miscibility gap between the perovskite phases of $CsPbI_3$ and $CsPbBr_3$;[51] second, the perovskite structure of mixed $CsPbBr_{3x}I_{3-3x}$ with high iodine content is structurally unstable.[57] In fact, spinodal decomposition of mixed analogous $MAPb(Br, I)_3$ into Br-rich and I-rich segments have been utilized to create perovskite heterostructures.[58] These factors can impose additional chemical constraints to hinder the bromide-iodide interdiffusion to result in significant alloying at RT. We further collected the PL from the "back side" of the transparent mica substrate (Figure 2.5B), and this allowed measurement on the part of the $CsPbBr_3$ NW that was covered by the $MAPbI_3$ microplate and thus not observable from the top. The two distinctive PL emission peaks (one near 540 nm and one near 700 nm) indicate that the interface of the heterojunction remains quite sharp without any intermediate emission, which is in stark contrast to the gradual shift in PL observed in the $CsPbCl_3/CsPbBr_3$ system. Nevertheless, within the miscible range close to the $CsPbBr_3$-rich compositions (Figure 2.5C), the iodide diffusion distance is determined to be ~12 μm. This leads to an estimated RT diffusion coefficient of ~ 10^{-12} $cm^2\ s^{-1}$ by simply using the equation of $L = \sqrt{Dt}$, where L is the diffusion distance. This value is two order of magnitude lower than the previously reported bromide-iodide interdiffusion coefficients in organic-inorganic hybrid perovskites,[59] suggesting the ion migration is slower in the all-inorganic Cs perovskites, as is also supported by other studies.[22]

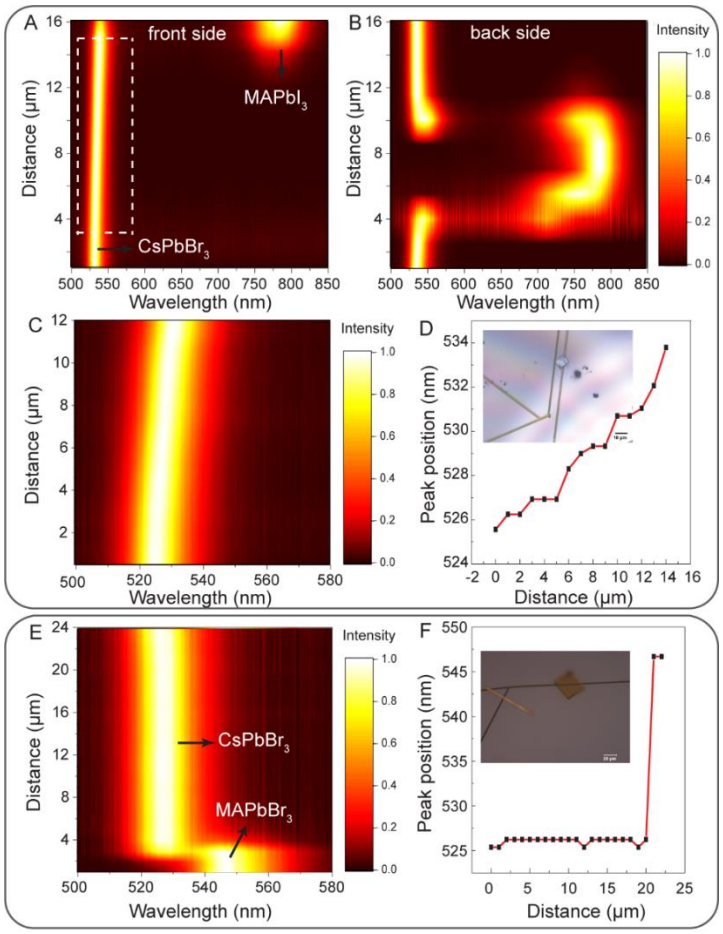

Figure 2.5 Studies of Br^--I^- diffusion in $CsPbBr_3/MAPbI_3$ and cation diffusion in $CsPbBr_3/MAPbBr_3$

Normalized PL line mapping of a $MAPbI_3/CsPbBr_3$ heterostructure collected from (A) front side and (B) back side of the mica substrate after a reaction time of 10 days at RT. (C) Magnified spectra of the region marked by the white dashed box in panel A. (D) PL peak center as function of distance extracted from Figure 4C. The inset shows an optical image of a $MAPbI_3$ microplate placed on $CsPbBr_3$ NWs. (E) PL line mapping of $MAPbI_3/CsPbBr_3$ heterostructure after a reaction time of 10 days at RT. (F) PL peak center position as function of distance extracted from Figure 4E. The inset shows an optical image of a $MAPbBr_3$ microplate placed on $CsPbBr_3$ NWs.

In contrast to the mobile halide anions, the A-site cations are relatively less mobile in the perovskite lattices. We note that $MAPbBr_3$ and $CsPbBr_3$ are completely miscible at RT, as shown

in the powder X-ray diffraction patterns of a series of solution-grown $(MA_xCs_{1-x})PbBr_3$ alloy samples we made (Figure A1.3). However, PL characterization of $MAPbBr_3$ microplates placed on $CsPbBr_3$ NWs shows no detectable change of the $CsPbBr_3$ NWs even after 10 days of reaction at RT (Figure 2.5E and 2.5F). Two distinct PL emission peaks corresponding to pure $MAPbBr_3$ microplates and $CsPbBr_3$ NWs remained. The negligible cation interdiffusion between $MAPbBr_3$ and $CsPbBr_3$ agrees well with previous calculation[30] that showed much higher migration activation energy for MA^+ than that for halide anions, potentially leading to orders of magnitude lower diffusivity as compared to the halide anions.

2.6 Conclusion

In summary, we have visualized and studied the solid-state anion and cation interdiffusion kinetics in lead halide perovskite nanowires by monitoring composition-dependent photoluminescence in real time. We found that the diffusion behaviors are influenced by the phase diagrams of the perovskite alloys and the activation energy for ionic diffusion. In $CsPbCl_3/CsPbBr_3$ system, due to complete phase miscibility, the anion interdiffusion significantly broaden the heterojunction by forming halide gradient $CsPbBr_{3-3x}Cl_{3x}$ NWs. By examining the time evolution of the composition profiles, we revealed the diffusion-driven nature of the chloride-bromide exchange reaction with kinetics obeying Fick's law. Quantitative analysis of such composition profiles yields the interdiffusion coefficients ($\sim 10^{-13}$ cm^2 s^{-1} at RT) and the activation energy (0.44 eV) of the chloride-bromide couple based on temperature dependent studies. In the $MAPbI_3/CsPbBr_3$ system, however, only limited extent of halide diffusion was observed, probably due to the limited miscibility and complex phase stability, resulting in a distinctive Br-rich and I-rich heterojunction. In contrast to the anions, A-site cation interdiffusion in $MAPbBr_3/CsPbBr_3$ system was very slow, a consequence of its higher migration activation energy. Our work not only

provides a model system for the mechanistic studies of the solid-state ion exchange, but also sheds additional insights to understanding the nature of ion mobility in lead halide perovskite materials. More importantly, these results can provide general guidelines for rationally designing heterostructures of halide perovskites with new optical properties and practical applications.

2.7 References

1. Lee, M. M.; Teuscher, J.; Miyasaka, T.; Murakami, T. N.; Snaith, H. J. *Science* **2012,** *338*, 643-647.
2. Burschka, J.; Pellet, N.; Moon, S. J.; Humphry-Baker, R.; Gao, P.; Nazeeruddin, M. K.; Gratzel, M. *Nature* **2013,** *499*, 316-319.
3. Zhu, H. M.; Fu, Y. P.; Meng, F.; Wu, X. X.; Gong, Z. Z.; Ding, Q.; Gustafsson, M. V.; Trinh, M. T.; Jin, S.; Zhu, X. Y. *Nat. Mater.* **2015,** *14*, 636-642.
4. Stranks, S. D.; Snaith, H. J. *Nat. Nanotechnol.* **2015,** *10*, 391-402.
5. Xing, G.; Mathews, N.; Sun, S.; Lim, S. S.; Lam, Y. M.; Grätzel, M.; Mhaisalkar, S.; Sum, T. C. *Science* **2013,** *342*, 344-347.
6. Huang, J.; Yuan, Y.; Shao, Y.; Yan, Y. *Nat. Rev. Mater.* **2017,** *2*, 17042.
7. Zhu, H.; Miyata, K.; Fu, Y.; Wang, J.; Joshi, P. P.; Niesner, D.; Williams, K. W.; Jin, S.; Zhu, X.-Y. *Science* **2016,** *353*, 1409-1413.
8. Dong, Q.; Fang, Y.; Shao, Y.; Mulligan, P.; Qiu, J.; Cao, L.; Huang, J. *Science* **2015,** *347*, 967-970.
9. Manser, J. S.; Saidaminov, M. I.; Christians, J. A.; Bakr, O. M.; Kamat, P. V. *Acc. Chem. Res.* **2016,** *49*, 330-338.
10. Eperon, G. E.; Ginger, D. S. *ACS Energy Lett.* **2017,** *2*, 1190-1196.
11. Akkerman, Q. A.; D'Innocenzo, V.; Accornero, S.; Scarpellini, A.; Petrozza, A.; Prato, M.; Manna, L. *J. Am. Chem. Soc.* **2015,** *137*, 10276-10281.
12. Fu, Y.; Zhu, H.; Stoumpos, C. C.; Ding, Q.; Wang, J.; Kanatzidis, M. G.; Zhu, X.; Jin, S. *ACS Nano* **2016,** *10*, 7963-7972.
13. Dou, L.; Lai, M.; Kley, C. S.; Yang, Y.; Bischak, C. G.; Zhang, D.; Eaton, S. W.; Ginsberg, N. S.; Yang, P. *Proc. Natl. Acad. Sci.* **2017,** *114*, 7216-7221.
14. Guhrenz, C.; Benad, A.; Ziegler, C.; Haubold, D.; Gaponik, N.; Eychmuller, A. *Chem. Mater.* **2016,** *28*, 9033-9040.
15. Pellet, N.; Teuscher, J.; Maier, J.; Gratzel, M. *Chem. Mater.* **2015,** *27*, 2181-2188.
16. Solis-Ibarra, D.; Smith, I. C.; Karunadasa, H. I. *Chem. Sci.* **2015,** *6*, 4054-4059.
17. Mizusaki, J.; Arai, K.; Fueki, K. *Solid State Ionics* **1983,** *11*, 203-211.
18. Narayan, R. L.; Suryanarayana, S. *Materials letters* **1991,** *11*, 305-308.
19. Snaith, H. J.; Abate, A.; Ball, J. M.; Eperon, G. E.; Leijtens, T.; Noel, N. K.; Stranks, S. D.; Wang, J. T.;

Wojciechowski, K.; Zhang, W. *J. Phys. Chem. Lett.* **2014,** *5*, 1511-1515.

20. Unger, E. L.; Hoke, E. T.; Bailie, C. D.; Nguyen, W. H.; Bowring, A. R.; Heumüller, T.; Christoforo, M. G.; McGehee, M. D. *Energy Environ. Sci.* **2014,** *7*, 3690-3698.
21. Chen, H. W.; Sakai, N.; Ikegami, M.; Miyasaka, T. *J. Phys. Chem. Lett.* **2015,** *6*, 164-169.
22. Meloni, S.; Moehl, T.; Tress, W.; Franckevicius, M.; Saliba, M.; Lee, Y. H.; Gao, P.; Nazeeruddin, M. K.; Zakeeruddin, S. M.; Rothlisberger, U.; Graetzel, M. *Nat. Commun.* **2016,** *7*, 10334.
23. Gottesman, R.; Haltzi, E.; Gouda, L.; Tirosh, S.; Bouhadana, Y.; Zaban, A.; Mosconi, E.; De Angelis, F. *J. Phys. Chem. Lett.* **2014,** *5*, 2662-2669.
24. Juarez-Perez, E. J.; Sanchez, R. S.; Badia, L.; Garcia-Belmonte, G.; Kang, Y. S.; Mora-Sero, I.; Bisquert, J. *J. Phys. Chem. Lett.* **2014,** *5*, 2390-2394.
25. Hoke, E. T.; Slotcavage, D. J.; Dohner, E. R.; Bowring, A. R.; Karunadasa, H. I.; McGehee, M. D. *Chem. Sci.* **2015,** *6*, 613-617.
26. Xiao, Z.; Yuan, Y.; Shao, Y.; Wang, Q.; Dong, Q.; Bi, C.; Sharma, P.; Gruverman, A.; Huang, J. *Nat. Mater.* **2015,** *14*, 193-198.
27. Li, C.; Tscheuschner, S.; Paulus, F.; Hopkinson, P. E.; Kiessling, J.; Kohler, A.; Vaynzof, Y.; Huettner, S. *Adv. Mater.* **2016,** *28*, 2446-2454.
28. Yuan, Y. B.; Chae, J.; Shao, Y. C.; Wang, Q.; Xiao, Z. G.; Centrone, A.; Huang, J. S. *Adv. Energy Mater.* **2015,** *5*, 1500615.
29. Yang, T. Y.; Gregori, G.; Pellet, N.; Gratzel, M.; Maier, J. *Angew. Chem. Int. Edit.* **2015,** *54*, 7905-7910.
30. Eames, C.; Frost, J. M.; Barnes, P. R.; O'Regan, B. C.; Walsh, A.; Islam, M. S. *Nat. Commun.* **2015,** *6*, 7497.
31. De Bastiani, M.; Dell'Erba, G.; Gandini, M.; D'Innocenzo, V.; Neutzner, S.; Kandada, A. R. S.; Grancini, G.; Binda, M.; Prato, M.; Ball, J. M.; Caironi, M.; Petrozza, A. *Adv. Energy. Mater.* **2016,** *6*.
32. Mosconi, E.; De Angelis, F. *ACS Energy Lett.* **2016,** *1*, 182-188.
33. Yuan, Y. B.; Huang, J. S. *Acc. Chem. Res.* **2016,** *49*, 286-293.
34. Shao, Y. C.; Fang, Y. J.; Li, T.; Wang, Q.; Dong, Q. F.; Deng, Y. H.; Yuan, Y. B.; Wei, H. T.; Wang, M. Y.; Gruverman, A.; Shielda, J.; Huang, J. S. *Energ Environ. Sci.* **2016,** *9*, 1752-1759.
35. Yun, J. S.; Seidel, J.; Kim, J.; Soufiani, A. M.; Huang, S. J.; Lau, J.; Jeon, N. J.; Seok, S. I.; Green, M. A.; Ho-Baillie, A. *Ad.v Energy. Mater* **2016,** *6*.
36. Haruyama, J.; Sodeyama, K.; Han, L. Y.; Tateyama, Y. *J. Am. Chem. Soc.* **2015,** *137*, 10048-10051.
37. Koscher, B. A.; Bronstein, N. D.; Olshansky, J. H.; Bekenstein, Y.; Alivisatos, A. P. *J. Am. Chem. Soc.* **2016,** *138*, 12065-12068.
38. Fu, Y. P.; Zhu, H. M.; Schrader, A. W.; Liang, D.; Ding, Q.; Joshi, P.; Hwang, L.; Zhu, X. Y.; Jin, S. *Nano Lett.* **2016,** *16*, 1000-1008.
39. Chen, J.; Fu, Y. P.; Samad, L.; Dang, L. N.; Zhao, Y. Z.; Shen, S. H.; Guo, L. J.; Jin, S. *Nano Lett.* **2017,** *17*, 460-466.

40. Wang, Y.; Sun, X.; Shivanna, R.; Yang, Y.; Chen, Z.; Guo, Y.; Wang, G.-C.; Wertz, E.; Deschler, F.; Cai, Z.; Zhou, H.; Lu, T.-M.; Shi, J. *Nano Lett.* **2016,** *16*, 7974-7981.
41. Shoaib, M.; Zhang, X.; Wang, X.; Zhou, H.; Xu, T.; Wang, X.; Hu, X.; Liu, H.; Fan, X.; Zheng, W.; Yang, T.; Yang, S.; Zhang, Q.; Zhu, X.; Sun, L.; Pan, A. *J. Am. Chem. Soc.* **2017,** *139*, 15592-15595.
42. Xing, J.; Liu, X. F.; Zhang, Q.; Ha, S. T.; Yuan, Y. W.; Shen, C.; Sum, T. C.; Xiong, Q. *Nano Lett.* **2015,** *15*, 4571-4577.
43. Wang, Y. P.; Sun, X.; Shivanna, R.; Yang, Y. B.; Chen, Z. Z.; Guo, Y. W.; Wang, G. C.; Wertz, E.; Deschler, F.; Cai, Z. H.; Zhou, H.; Lu, T. M.; Shi, J. *Nano Lett.* **2016,** *16*, 7974-7981.
44. De Trizio, L.; Manna, L. *Chem. Rev.* **2016,** *116*, 10852-10887.
45. Groeneveld, E.; Witteman, L.; Lefferts, M.; Ke, X. X.; Bals, S.; Van Tendeloo, G.; Donega, C. D. *ACS Nano* **2013,** *7*, 7913-7930.
46. Justo, Y.; Sagar, L. K.; Flamee, S.; Zhao, Q.; Vantomme, A.; Hens, Z. *ACS Nano* **2014,** *8*, 7948-7957.
47. Zhao, Y. J.; Li, J.; Dahn, J. R. *Chem. Mater.* **2017,** *29*, 5239-5248.
48. Li, J.; Doig, R.; Camardese, J.; Plucknett, K.; Dahn, J. R. *Chem. Mater.* **2015,** *27*, 7765-7773.
49. Sakka, Y.; Oishi, Y.; Ando, K. *B Chem. Soc. Jpn.* **1982,** *55*, 420-422.
50. Yin, W. J.; Shi, T. T.; Yan, Y. F. *Appl. Phys. Lett.* **2014,** *104*.
51. Yin, W. J.; Yan, Y. F.; Wei, S. H. *J. Phys. Chem. Lett.* **2014,** *5*, 3625-3631.
52. Crank, J., *The mathematics of diffusion*. Clarendon Press: Oxford, **1956**, p347.
53. Fick, A. *Annalen der Physik* **1855,** *170*, 59-86.
54. Bradley, I.; Gillin, W.; Homewood, K.; Webb, R. *J. Appl. Phys.* **1993,** *73*, 1686-1692.
55. Gillin, W. P.; Dunstan, D. J.; Homewood, K. P.; Howard, L. K.; Sealy, B. J. *J. Appl. Phys.* **1993,** *73*, 3782-3786.
56. Rockenhauser, C.; Butz, B.; Schichtel, N.; Janek, J.; Oberacker, R.; Hoffmann, M. J.; Gerthsen, D. *J. Eur. Ceram. Soc.* **2014,** *34*, 1235-1242.
57. Cottingham, P.; Brutchey, R. L. *Chem. Mater.* **2016,** *28*, 7574-7577.
58. Wang, Y. P.; Chen, Z. Z.; Deschler, F.; Sun, X.; Lu, T. M.; Wertz, E. A.; Hu, J. M.; Shi, J. *ACS Nano* **2017,** *11*, 3355-3364.
59. Shewmon, N. T.; Yu, H.; Constantinou, I.; Klump, E.; So, F. *ACS Appl. Mater. Interfaces* **2016,** *8*, 33273-33279.

Chapter 3 Epitaxial Growth of ultrasmooth $CsPbBr_3$ Single-Crystalline Thin Films on Gadolinium Gallium Garnet Substrate

3.1 Abstract

Halide perovskite single crystals merit the excellent photophysical properties and are less susceptible to detrimental effects brought by defects or grain boundaries. Single crystal in the form of thin films would be particularly desired due to the ease of integration with other materials and device fabrication. However, growth of large area single-crystalline halide perovskite continuous thin film is challenging. Here we report the epitaxial growth of ultra-smooth $CsPbBr_3$ single-crystal thin films (SCTFs) on gallium gadolinium garnet (GGG) (100) substrates by chemical vapor deposition. Despite the lattice mismatch, good incommensurate epitaxy was achieved between $CsPbBr_3$ and GGG, with $CsPbBr_3$ [100] || GGG [100] and $CsPbBr_3$ [010] || GGG [010]. The resulting $CsPbBr_3$ SCTFs exhibit excellent crystal quality, surface smoothness, and high environmental stability, which make it an ideal building block for integration with other materials or fabrication of heterostructure devices. This success of this growth demonstrates the versatility of halide perovskites for epitaxial growth on various multi-functional oxide substrates, and the potential of halide perovskite SCTFs as building blocks for future optoelectronic applications.

3.2 Introduction

In the recent years, metal halide perovskite (MHPs), as an emerging class of solution-processed semiconductors, have drawn great research interest. The general formula of MHPs is ABX_3, where A represents a monovalent cation, B is usually Pb or Sn, and X corresponds to a halogen. They were first reported as promising visible-light sensitizers in PV cells with a power conversion efficiency (PCE) of 3.9% in 2009[1], which has now exceeded 25% in 2021 in MHPs-based solar cells[2]. They have also shined in optoelectronic applications including lasers[3,4],

photodetectors[5], and light-emitting diodes (LEDs)[6], have demonstrated decent performance. The outstanding performance of MHPs can be attributed to their superior characteristics, such as large optical absorption coefficient, high and balanced carrier mobility, long carrier diffusion length and great defect tolerance. However, most of the devices are based on polycrystalline thin films due to the ease of fabrication and manipulation. Single-crystalline thin films with fewer grain boundaries and lower trap densities may further boost the device performance of halide perovskites by increasing the carrier mobilities and lifetimes.

Although various synthetical approaches have been developed for the growth of halide perovskite single-crystals, such as antisolvent vapor-assisted crystallization[7,8], slow crystallization from saturated solutions[9-11], and inverse crystallization[12,13], the growth of large-area single-crystal thin films of halide perovskite is still scarce. In the past, vapor-phase epitaxy growth has proven to be a powerful technique for growing high quality thin films of traditional semiconductors[14-16]. Vapor-phase epitaxial growth of halide perovskite nanostructures have been widely reported[17,18]. In fact, in many of these works, relaxed lattice matching has been reported in halide perovskite epitaxial growth due to the ionic nature of their lattice.[19] Previously, our group found the $CsPbBr_3$ SCTFs can be epitaxially grown on $SrTiO_3$ (STO) (100)[20], a common oxide perovskite substrate. The success of this epitaxial growth was attributed to similar perovskite structural type and small lattice mismatch between 2 unit cells of $CsPbBr_3$ and 3 unit cells of STO. The epitaxial growth halide perovskite on other multi-functional oxide substrates is of great interest and has not been explored yet.

Here we report a facile method to grow large-are ultra-smooth $CsPbBr_3$ SCTFs on GGG (100) substrates by chemical vapor deposition. The crystal quality of the as-grown thin film is attested by PXRD and the mirror-like reflection from the thin film surface. XRD pole figures and *phi*-scans

are employed to confirm good incommensurate epitaxy between $CsPbBr_3$ and GGG, with $CsPbBr_3$ [100] || GGG [100] and $CsPbBr_3$ [010] || GGG [010]. We found the key to achieving high-quality continuous growth was the reaction temperature and crucial GGG pre-treatment. The resulting $CsPbBr_3$ SCTFs are ideal candidates for integration with other materials and fabrication of heterostructure devices.

3.3 Experimental section

3.3.1 Synthesis

All chemicals were purchased from Sigma-Aldrich and used as received unless otherwise noted. The GGG (100) single-crystal substrates (10 mm × 10 mm × 0.5 mm) were purchased from MTI Corporation, USA, which were cut in halves for each growth. The GGG substrate was first immersed in hot water (80 °C, 60 min) before etched by a buffered HF solution (2 min) and then washed by deionized water. It was then annealed for 30 min at 1000 °C in N_2 atmosphere, before crystal growth, to achieve an atomically flat surface.

The epitaxial growth of $CsPbBr_3$ single crystal thin films was carried out in a home-built chemical vapor deposition furnace equipped with mass flow controllers and pressure control. The growth happens in a "tube-in-tube" manner (Figure A2.1), where the $CsPbBr_3$ precursor ingots were placed in the inner quarts tube (diameter ~ 1.2 cm) with the sealed end facing the carrier gas flow direction, which helps maintain a steady laminar flow favorable for controlled epitaxial growth. The inner tube was then placed in the outer tube (diameter ~ 2.1 cm) with its sealed end close to the center of the heating zone. The treated GGG (100) substrate was placed downstream about 12 cm away from the $CsPbBr_3$ ingots. The CVD reaction was carried out at an optimal temperature of 450 °C for the continuous growth $CsPbBr_3$ SCTFs for 15-30 min, depending on the desired thickness. The furnace was turned off and allowed to cool naturally to room temperature.

3.3.2 Structural characterization

The optical images were obtained on an Olympus BX51M optical microscope. The scanning electron microscopy (SEM) images were collected on a LEO SUPRA 55 VP field-emission scanning electron microscope operated at 3kV. The PXRD data were collected on a Bruker D8 Advance Powder X-ray Diffractometer with the Cu Kα radiation. The XRD rocking curve and pole figures were obtained on a Bruker D8 Discovery Diffractometer equipped with a specimen rotating holder. Atomic Force Microscope (AFM) imaging was performed on an Agilent 5500 in the contact mode with SNL-10 tips (k: 0.12 N/m). The root mean-squared roughness (S_q) was estimated from analysis of the AFM image by Gwyddion. The photoluminescence (PL) spectrum was collected with an Aramis Confocal Raman microscope using a 442 nm laser.

3.4 Results and Discussion

Gadolinium gallium garnet ($Gd_3Ga_5O_{12}$, or GGG) is a well-studied frustrated magnet material[21-23]. It has a cubic lattice ($Ia\bar{3}d$, a = 12.383 Å) in which the magnetic Gd^{3+} ions are on two interpenetrating corner-sharing triangular sublattices within the garnet structure (Figure 3.1a). We recognized that the lattice constant of GGG is roughly two times that of $CsPbBr_3$ ($Pm\bar{3}m$, a = 5.830 Å). Therefore, two unit cells of $CsPbBr_3$ could potentially match one unit cell of GGG in an incommensurate fashion with a mismatch factor of 5.8% in both $CsPbBr_3$[100] || GGG [100] and $CsPbBr_3$[010] || GGG [010] directions (Figure 3.1b,c). This moderate lattice mismatch may not prevent the epitaxial growth, as halide perovskites have been reported to grow on dissimilar substrates with large lattice mismatch, thanks to their soft and ionic nature (termed “ionic epitaxy”).

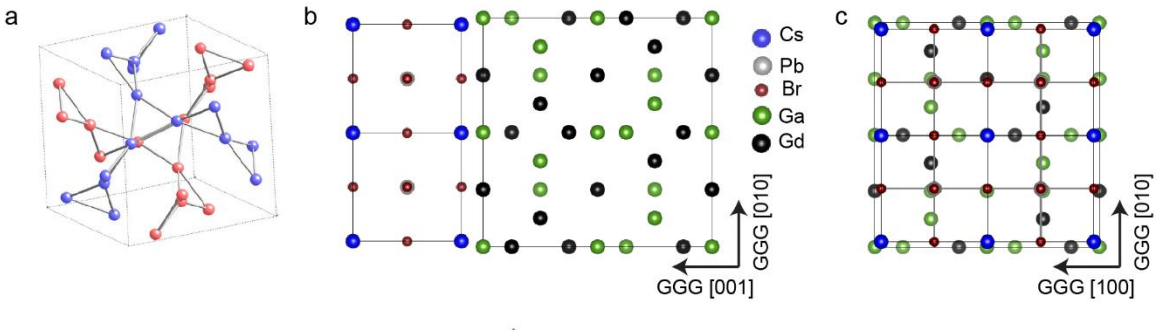

Figure 3.1 Illustration of the heteroepitaxy of $CsPbBr_3$ on GGG (100)

(a) The two interpenetrating Gd sublattices in GGG. The nearest neighbors forming the triangles are indicated. Ga and O are omitted for clarity. Side view (b) and top view (c) of the incommensurate lattice match between $CsPbBr_3$ (100) and GGG (100) crystallographic planes, where 2 x 2 $CsPbBr_3$ (100) unit cells match 1 x 1 GGG (100) unit cell.

We found $CsPbBr_3$ single-crystalline thin films (SCTFs) could be epitaxially grown on GGG (100) substrates by chemical vapor deposition (CVD) following procedures modified from our previous work.[20] Lower temperature led to the growth of $CsPbBr_3$ nanoplate arrays, indicating a Volmer-Weber island formation heteroepitaxial growth mode (Figure A2.2). With the optimal reaction temperature of 450 °C, large-area continuous $CsPbBr_3$ SCTFs can be grown. Another key to the success of high-quality epitaxial growth is to treat the GGG substrate before each growth. Specifically, the GGG substrate is immersed in hot water (80 °C, 60 min) before etched with a buffered HF solution (2 min) and then washed by deionized water. It is then annealed for 30 min at 1000 °C in N_2 atmosphere, before crystal growth, to achieve an atomically flat surface. The optical microscope (Figure 3.2a) and scanning electron microscope (SEM) images (Figure 3.2b) show the as-grown $CsPbBr_3$ thin film surface is ultrasmooth, with no apparent grain boundaries or holes at high magnification. The smoothness is further demonstrated by the mirror-like reflection (Figure 3.2a inset) from the as-grown thin film under light. The surface roughness (*Sq*) of the film

was measured by AFM to be around 0.7 nm (Supporting Figure A3), much smaller than that grown on STO (26 nm) previously.[20] A reaction time of 20 min yielded a film thickness of approximately 8 μm, as shown in the cross-section SEM image (Figure 3.2c). No obvious grain boundaries were observed in the cross-section SEM. The $CsPbBr_3$ SCTFs shows a bright photoluminescence (PL) emission centered around 525 nm with a FWHM of ~ 18 nm, consistent with previous reports.

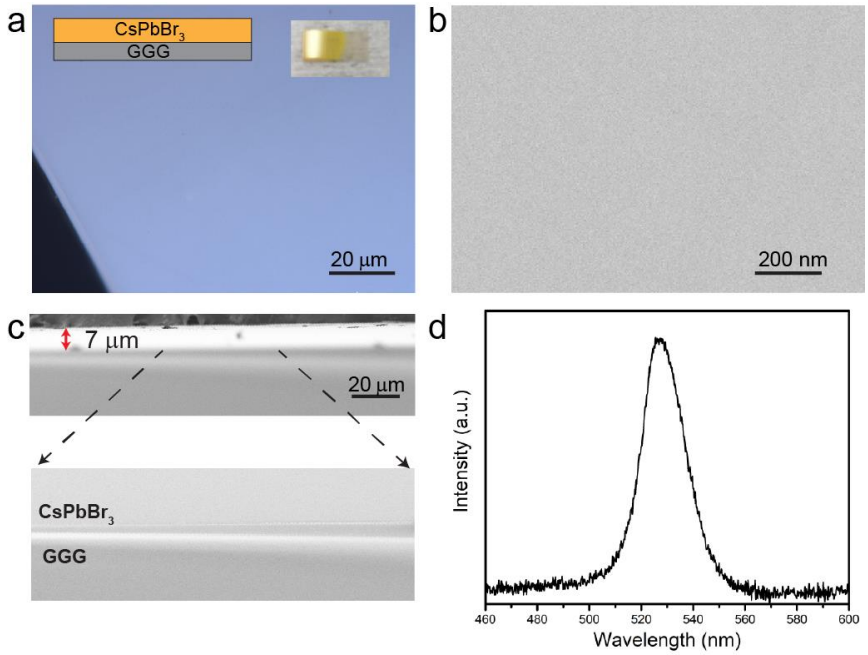

Figure 3.2 Characterization of the ultrasmooth $CsPbBr_3$ single-crystal thin film on GGG (100) substrate

(a) Schematic (top left) and optical image of the as-grown $CsPbBr_3$ single-crystal thin film on GGG substrate. The inset is a photograph of the thin film that shows a clear mirror-like reflection, which indicates the smoothness. (b) SEM image of the as-grown $CsPbBr_3$ thin film. (c) Cross-sectional SEM image of the $CsPbBr_3$ single-crystal thin film on GGG substrate. The thickness of $CsPbBr_3$ is estimated to be ~ 8 μm. (d) PL spectrum of the $CsPbBr_3$ thin film.

The XRD 2θ scans for the as grown 8 μm $CsPbBr_3$ SCTFs on GGG (100) substrate shows only (100) and (200) peaks of $CsPbBr_3$, in addition to GGG (400) and (800) peaks (Figure 3.3a).

The rocking curve for the $CsPbBr_3$ (200) diffraction peak has a narrow full width at half-maximum (FWHM) of 0.10°, lower than that of the previously reported SCTF grown on STO (100) substrate. The (101) pole figure of the sample showed 4 poles with 90° intervals, corresponding to planes with equivalent symmetry to (101) plane (Figure 3.2b). Lastly, the *Phi*-scans around GGG {048} and $CsPbBr_3$ {024} planes showed that diffraction peaks occur at the same *phi* angles. These results conclusively confirm there is only one single-crystal domain in the as-grown $CsPbBr_3$ SCTFs, and the epitaxial alignments between the two cubic structures are $CsPbBr_3$ [100] || GGG [100] and $CsPbBr_3$ [010] || GGG [010], as shown in Figure 3.1.

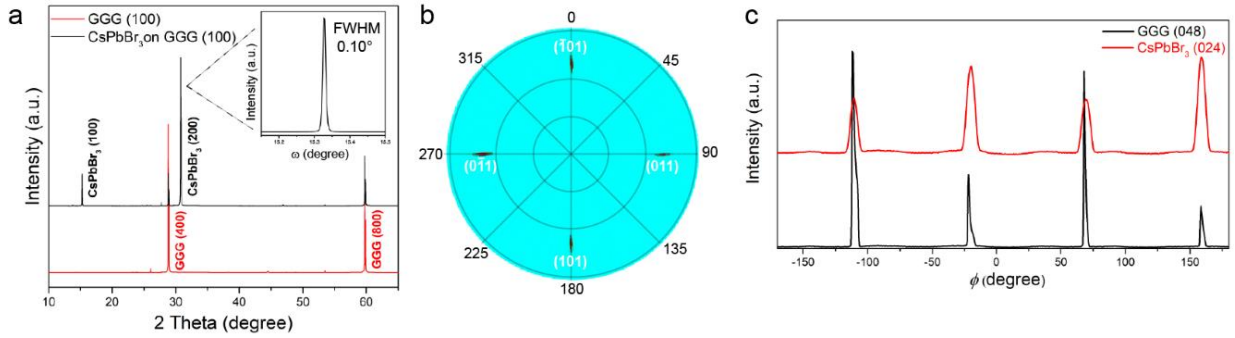

Figure 3.3 Structural characterization of $CsPbBr_3$ single-crystal thin film epitaxially grown on GGG (100) substrate

(a) XRD 2θ scans of the as-grown $CsPbBr_3$ thin film on GGG (100) substrate. The inset shows the ω-rocking curve of the $CsPbBr_3$ (200) peak. (b) The (101) pole figure of the $CsPbBr_3$ thin film. (c) *Phi*-scan around GGG {048} and $CsPbBr_3$ {024} showing diffractions appear at the same *Phis*.

3.5 Conclusion

In conclusion, we show that ultra-smooth SCTFs of $CsPbBr_3$ can be epitaxially grown on GGG (100) substrate by chemical vapor deposition. Despite the lattice mismatch, good incommensurate epitaxy was achieved between $CsPbBr_3$ and GGG, with $CsPbBr_3$ [100] || GGG [100] and $CsPbBr_3$ [010] || GGG [010]. The resulting $CsPbBr_3$ SCTFs exhibit excellent crystal

quality and stability, and is an ideal candidate for integration with other materials and fabrication of heterostructure devices. This demonstrates the versatility of halide perovskites for epitaxial growth on various oxide substrates with diverse semiconducting, magnetic and ferroelectric properties, and the potential of halide perovskite SCTFs as building blocks for future optoelectronic applications.

3.6 References

1 Kojima, A., Teshima, K., Shirai, Y. & Miyasaka, T. Organometal Halide Perovskites as Visible-Light Sensitizers for Photovoltaic Cells. *Journal of the American Chemical Society* **131**, 6050-+, doi:10.1021/ja809598r (2009).

2 Jeong, J. *et al.* Pseudo-halide anion engineering for alpha-FAPbI(3) perovskite solar cells. *Nature*, doi:10.1038/s41586-021-03406-5 (2021).

3 Xing, G. C. *et al.* Low-temperature solution-processed wavelength-tunable perovskites for lasing. *Nat Mater* **13**, 476-480, doi:10.1038/Nmat3911 (2014).

4 Zhu, H. M. *et al.* Lead halide perovskite nanowire lasers with low lasing thresholds and high quality factors. *Nat Mater* **14**, 636-U115, doi:10.1038/Nmat4271 (2015).

5 Dou, L. T. *et al.* Solution-processed hybrid perovskite photodetectors with high detectivity. *Nat Commun* **5**, doi:ARTN 540410.1038/ncomms6404 (2014).

6 Sutherland, B. R. & Sargent, E. H. Perovskite photonic sources. *Nat Photonics* **10**, 295-302, doi:10.1038/Nphoton.2016.62 (2016).

7 Shi, D. *et al.* Low trap-state density and long carrier diffusion in organolead trihalide perovskite single crystals. *Science* **347**, 519-522, doi:10.1126/science.aaa2725 (2015).

8 Rakita, Y. *et al.* Low-Temperature Solution-Grown CsPbBr3 Single Crystals and Their Characterization. *Cryst Growth Des* **16**, 5717-5725, doi:10.1021/acs.cgd.6b00764 (2016).

9 Baikie, T. *et al.* Synthesis and crystal chemistry of the hybrid perovskite (CH3NH3) PbI3 for solid-state sensitised solar cell applications. *J Mater Chem A* **1**, 5628-5641, doi:10.1039/c3ta10518k (2013).

10 Dang, Y. Y. *et al.* Bulk crystal growth of hybrid perovskite material CH3NH3PbI3. *Crystengcomm* **17**, 665-670, doi:10.1039/c4ce02106a (2015).

11 Lian, Z. P. *et al.* Perovskite CH3NH3PbI3(Cl) Single Crystals: Rapid Solution Growth, Unparalleled Crystalline Quality, and Low Trap Density toward 10(8) cm(-3). *Journal of the American Chemical Society* **138**, 9409-9412, doi:10.1021/jacs.6b05683 (2016).

12 Saidaminov, M. I. *et al.* High-quality bulk hybrid perovskite single crystals within minutes by inverse temperature crystallization. *Nat Commun* **6**, doi:ARTN 758610.1038/ncomms8586 (2015).

13 Dirin, D. N., Cherniukh, I., Yakunin, S., Shynkarenko, Y. & Kovalenko, M. V. Solution-Grown CsPbBr3 Perovskite Single Crystals for Photon Detection. *Chem Mater* **28**, 8470-8474, doi:10.1021/acs.chemmater.6b04298 (2016).

14 Meyerson, B. S. Low-Temperature Silicon Epitaxy by Ultrahigh-Vacuum Chemical Vapor-Deposition. *Appl Phys Lett* **48**, 797-799, doi:Doi 10.1063/1.96673 (1986).

15 Tsukazaki, A. *et al.* Repeated temperature modulation epitaxy for p-type doping and light-emitting diode based on ZnO. *Nat Mater* **4**, 42-46, doi:10.1038/nmat1284 (2005).

16 Yoon, J. *et al.* GaAs photovoltaics and optoelectronics using releasable multilayer epitaxial assemblies. *Nature* **465**, 329-U380, doi:10.1038/nature09054 (2010).

17 Chen, J. *et al.* Vapor-Phase Epitaxial Growth of Aligned Nanowire Networks of Cesium Lead Halide Perovskites (CsPbX3, X = Cl, Br, I). *Nano Lett* **17**, 460-466, doi:10.1021/acs.nanolett.6b04450 (2017).

18 Oksenberg, E., Sanders, E., Popovitz-Biro, R., Houben, L. & Joselevich, E. Surface-Guided CsPbBr3 Perovskite Nanowires on Flat and Faceted Sapphire with Size-Dependent Photoluminescence and Fast Photoconductive Response. *Nano Lett* **18**, 424-433, doi:10.1021/acs.nanolett.7b04310 (2018).

19 Wang, Y. P. *et al.* High-Temperature Ionic Epitaxy of Halide Perovskite Thin Film and the Hidden Carrier Dynamics. *Adv Mater* **29**, doi:ARTN 170264310.1002/adma.201702643 (2017).

20 Chen, J. *et al.* Single-Crystal Thin Films of Cesium Lead Bromide Perovskite Epitaxially Grown on Metal Oxide Perovskite (SrTiO3). *Journal of the American Chemical Society* **139**, 13525-13532, doi:10.1021/jacs.7b07506 (2017).

21 Wen, D., Gmelin, E. & Kremer, R. Magnetothermal Properties of Sintered Gd3ga5o12. *J Phys D Appl Phys* **21**, 628-635 (1988).

22 Paddison, J. A. M. *et al.* Hidden order in spin-liquid Gd3Ga5O12. *Science* **350**, 179-181, doi:10.1126/science.aaa5326 (2015).

23 Woo, N., Silevitch, D. M., Ferri, C., Ghosh, S. & Rosenbaum, T. F. Interplay of disorder and geometrical frustration in doped gadolinium gallium garnet. *J Phys-Condens Mat* **27**, doi:Artn 29600110.1088/0953-8984/27/29/296001 (2015).

Chapter 4 Deterministic Fabrication of Arbitrary Vertical Heterostructures of 2D-Ruddlesden-Popper Halide Perovskites[2]

4.1 Abstract

Ruddlesden-Popper (RP) lead halide perovskites have emerged as a new class of 2D semiconductors with tunable optoelectronic properties, potentially offering unlimited heterostructure configurations for exploration. However, the practical realization of such heterostructures is challenging because of the difficulty in controllable direct synthesis or van der Waals integration of halide perovskites due to their mobile and fragile crystal lattices. Here, we report direct growth of large-area nanosheets of diverse phase-pure RP perovskites with thickness down to a monolayer at the solution-air interface and a reliable approach for gently transferring and stacking these nanosheets. These advances enable the deterministic fabrication of arbitrary vertical heterostructures and multi-heterostructures of RP perovskites with unprecedented structural degrees of freedom that define the electronic structures of the heterojunctions. Such rationally designed heterostructures exhibit interesting interlayer properties, such as interlayer carrier transfer and reduction of photoluminescence linewidth, and could enable the exploration of exciton physics and optoelectronic applications.

4.2 Introduction

Ruddlesden-Popper (RP) lead halide perovskites have emerged as a new class of tunable two-dimensional (2D) semiconductors that demonstrate high performance in optoelectronics[1-3]. They have the general formula of $(LA)_2(A)_{n-1}Pb_nX_{3n+1}$, where LA is a long-chain alkylammonium cation, A is a small cation such as methylammonium (MA) and formamidinium (FA), X is a halide

[2] This chapter was originally published in *Nat. Nanotech.*, **2021**, 16(2), 159-165, in collaboration with Y. Fu, N. Spitha, Y. Zhao, C. R. Roy, D. J. Morrow, D. D. Kohler, J. C. Wright, and S. Jin

anion, and *n* is an integer. Their crystal structures consist of stacked 2D layers of $[(A)_{n-1}Pb_nX_{3n+1}]^{2-}$ inorganic framework charge balanced by the organic LA cations in the interlayer space. These structures can be regarded as natural multiple-quantum-wells in which the nanometer thick inorganic layers act as potential "wells" and the interlayer organic layers act as potential "barriers"[4], akin to III–V semiconductor quantum wells[5-8]. Due to the low dielectric constant of the interlayer cations, the excitons residing in the well experience significantly enhanced Coulomb interaction with exciton binding energies up to a few hundred meV[9]. Unique to RP perovskites, such inherent quantum and dielectric confinement can be readily tuned at the molecular level, in addition to the composition-dependent bandgap. These make RP perovskites a diverse and versatile 2D materials platform[10-13] for exploring exciton physics and high-performance optoelectronic devices, as demonstrated in van der Waals heterostructures of transition metal dichalcogenides (TMDs)[14-17].

Fulfilling the promises of 2D RP perovskite heterostructures, however, demands deterministic fabrication capability to achieve rationally designed electronic structures. Mechanical stacking is commonly used for creating van der Waals heterostructures of 2D materials such as graphene, hexagonal boron nitride (hBN) and TMDs[14,15]. However, the fragile nature of halide perovskite materials and the limited lateral dimension make transferring and mechanically stacking of exfoliated 2D RP perovskite thin sheets[10] or those directly grown on substrates[12] much less effective and reliable. Attempts on direct solution growth of heterostructures of 2D RP perovskites lack control over composition and morphology[18,19], and have so far only led to mixtures consisting of neighboring *n* phases[20-23]. Moreover, heterostructures of perovskites with different halides are synthetically forbidden because of the facile formation of mixed halide alloy phases[24,25] due to interdiffusion of halide anions[26,27]. Lateral heterostructures of thin layer $n = 1$ 2D perovskites have recently been realized through a sequential growth method[28]. Here, we report

a hybrid approach to deterministically fabricate arbitrary vertical heterostructures of 2D RP lead halide perovskites with different halides, *n* phases, LA and/or A cations, which is enabled by controllable growth of large-area molecularly thin nanosheets of various phase-pure RP perovskites at the solution-air interface and a facile method for gently transferring and stacking the as-grown sheets. Such capabilities not only enabled the fabrication of several types of vertical heterostructures and multi-heterostructures of RP perovskites previously inaccessible, but also led to the observation of interlayer carrier transfer and reduction of photoluminescence linewidth in rationally designed heterostructures with intimate interlayer electronic interaction.

4.3 Results and discussion

4.3.1 Floating growth of nanosheets

We developed a simple but general crystallization method at the air-solution interface of precursor solution droplets (Fig. 4.1a) to synthesize large-area free-standing nanosheets of various RP perovskites (see Methods for details). Briefly, a warm saturated aqueous solution containing perovskite precursors dissolved in concentrated hydroiodic (or hydrobromic) acid is dropped onto a glass slide. The droplet becomes supersaturated upon cooling, initiating nucleation and crystal growth. The amphiphilic LA cations self-assemble at the solution-air interface and serve as a soft template that lowers the nucleation barrier at the solution surface (than in the solution) and facilitates the highly anisotropic 2D growth in a “soft epitaxy” fashion. Supplementary Video 1 (available online) shows that nucleation rapidly occurs on water surface followed by crystallization along the basal plane, leading to the growth of floating nanosheets with lateral size up to a few hundred micrometers within seconds.

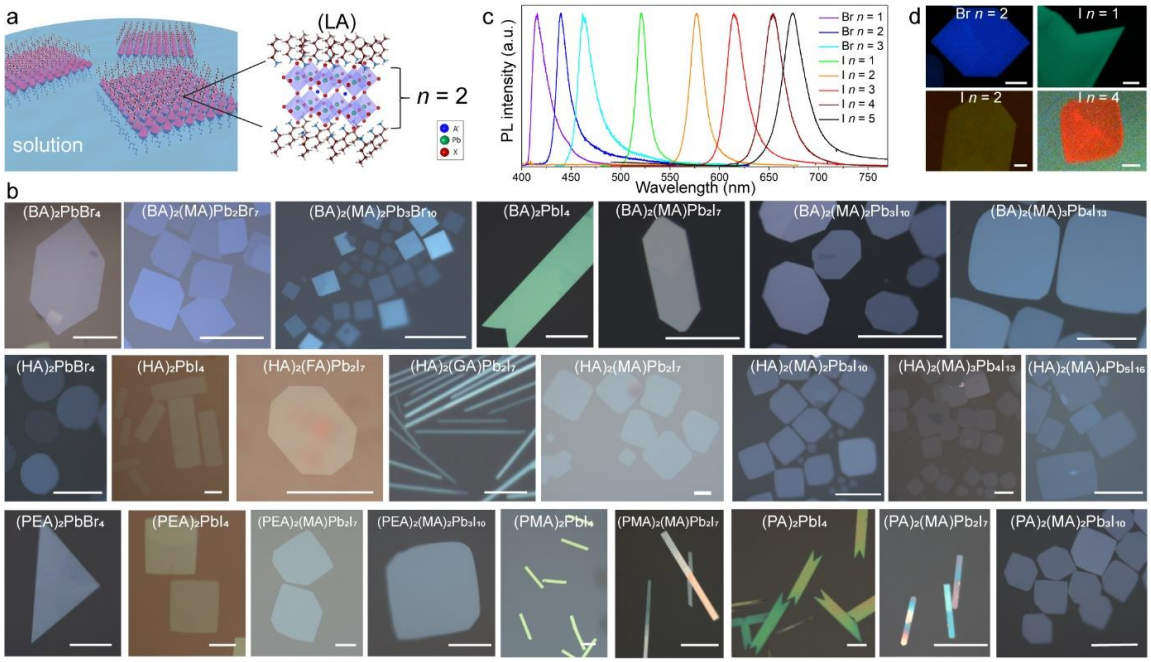

Figure 4.1 Floating growth of large area nanosheets of various phases of 2D RP perovskites **a,** Scheme for the solution floating growth of 2D RP perovskite nanosheets at the solution-air interface, using the example of an $n = 2$ RP perovskite $(LA)_2(A)Pb_2I_7$**. b,** Optical images of various phases of RP perovskite nanosheets (or occasionally nanoribbons) still floating on water surface. All scale bars are 50 μm. **c,** PL characterization of the nanosheets of $(BA)_2PbBr_4$, $(BA)_2(MA)Pb_2Br_7$, $(BA)_2(MA)_2Pb_3Br_{10}$, $(HA)_2PbI_4$, $(HA)_2(MA)Pb_2I_7$, $(HA)_2(MA)_2Pb_3I_{10}$, $(HA)_2(MA)_3Pb_4I_{13}$, $(HA)_2(MA)_4Pb_5I_{16}$, respectively, which give access to light emission from 413 nm to 678 nm. **d**, Real-color PL images of selective RP perovskite phases under UV LED excitation. Scale bar: 25 μm.

The key to achieving monolayer or few-layer thickness while maximizing lateral growth is maintaining a proper supersaturation, which is carefully optimized by tuning the concentrations of each precursor and the temperatures from which the solution is cooled. At concentrations greatly exceeding saturation, new nuclei are continuously generated on the existing sheets, which quickly increases the thickness. At concentrations just above saturation, only a few nuclei are generated,

and screw dislocation-driven growth is promoted to produce thick spiral microplates. Only at the optimized conditions (specified in Appendix Table A3.1), the crystal growth follows the layer-by-layer growth mechanism to produce large-area thin and flat sheets (Figure A3.1a). As the supersaturation decreases with the growth time, dislocation-driven growth emerges and dominates the crystal growth (Figure A3.1b), resulting in the formation of thick microplates and dissolution of existing thin sheets (i.e. Ostwald ripening, Supplementary Video 2, available online). These observations agree with the classical crystal growth theory[29] and demonstrate the critical roles of controlling supersaturation and growth time in obtaining atomically thin 2D materials. Carefully controlled synthesis conditions yield reproducible growth in terms of nanosheet size and thickness (Figure A3.2).

One of the most attractive attributes of RP perovskites is the ability to tune the electronic and optical properties through composition engineering[1-4]. By changing the stochiometric ratios of (LA)X, AX, and PbX_2 in precursor solutions (Table A1), we were able to synthesize thin sheets of diverse RP perovskite phases (Fig. 4.1b), where LA is *n*-butylammonium (BA), *n*-pentylammonium (PA), *n*-hexylammonium (HA), phenylmethylammonium (PMA) or phenethylammonium (PEA), A is MA, FA or guanidinium (GA), X is Br, or I, with *n* from 1 upto 5 (for some compositions). Interestingly, the resulting nanostructure of each phase has its own characteristic shape and apparent color, and some phases clearly prefer to grow into nanoribbons. The ease of acquiring large-area (hundreds of μm) sheets also varies (Figure A3.3). The phase purity (i.e. single *n*-value phase) of these sheets was confirmed by micro-photoluminescence (PL) measurements (Fig. 4.1c), power-dependent low temperature PL (Figure A3.4) and powder X-ray diffraction of selected phases (Figure A3.5). Notably the PL emission wavelength can be tuned from 413 nm with Br as the halide, $n = 1$ (referred to as Br $n = 1$, similarly for other phases

thereafter) to 678 nm with I n = 5, because of the composition-dependent bandgap and varying degree of quantum confinement. The bright real-color PL images of selected phases (Fig. 4.1d) under a handheld UV LED flashlight excitation (400 nm) suggest the relatively high PLQY of these 2D RP perovskties[12,30,31] as compared to other 2D semiconductors, such as monolayer TMDs. The estimated PLQY for 7 representative RP perovskite nanosheets (Figure A3.6) reveal that the n = 1 phases generally exhibit higher PLQY owing to their high exciton binding energies and the PEA-homologous series are brighter than other LA-series, with the $(PEA)_2PbI_4$ showing ~ 36 % average PLQY, consistent with previous reports[17, 32].

4.3.2 Pick-up and transfer of the floating nanosheets

We can pick up these floating thin sheets and transfer them onto arbitrary substrates including glass, quartz and Si/SiO_2, via a soft transfer method without compromising the sheets' structural integrity. Briefly, a polydimethylsiloxane (PDMS) film was gently placed in contact with the droplet surface and then lifted (Fig. 4.2a). The floating sheets were brought onto the PDMS film while the solution was expelled due to the hydrophobicity of both PDMS and LA ligands. Subsequently, the perovskite sheets were released and laminated on Si/SiO_2 substrates via elastomeric transfer printing[32]. Although the perovskites are fragile especially when they are atomically thin, the transferred sheets remained mostly intact and the surface appeared to be clean, smooth, and free of liquid over tens of micrometers (Fig. 4.2b-e, Figure A3.7). PL mapping further confirms the uniformity of the sheets after transfer (Figure A3.8). The ease and success of this transfer process are facilitated by the hydrophobic nature of PDMS as well as the soft/compliant character of water droplets and the PDMS film.

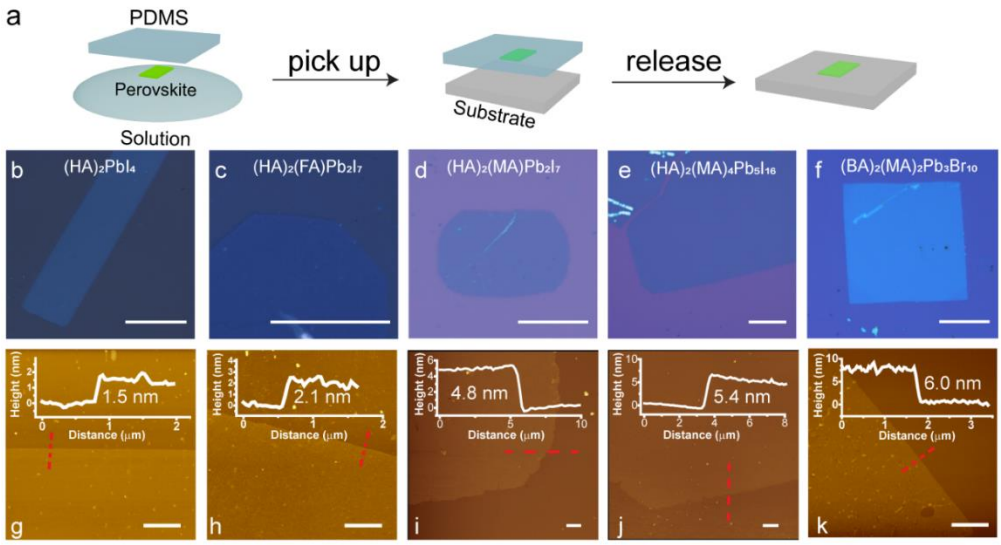

Figure 4.2 Pick-up of the floating RP perovskite thin sheets and characterization after transfer onto Si/SiO_2 substrates

a, Schematic illustration for the process of picking up the floating thin sheets with PDMS and transferring onto other substrates. **b-f,** Optical images showing representative transferred nanosheets on Si/SiO_2 substrates. Scale bar: 25 μm. **g-k,** Corresponding AFM images of the nanosheets and height profiles extracted along the red dotted lines demonstrating the smoothness and the thicknesses down to monolayer or single unit cell. Scale bar: 2 μm.

The thickness of these sheets varies from ~1 μm down to a few nm (Figure A3.9) depending on the growth time. The smallest thickness obtained (Fig. 4.2g-k) corresponds to a monolayer [for examples, 1.9 nm for $(HA)_2PbI_4$, 2.4 nm for $(HA)_2(FA)Pb_2I_7$] or a single unit cell of the RP perovskite crystal structures. The optical contrast of the as-grown sheets and their apparent color after transferred to Si/SiO_2 substrates vary with their thickness (Figure A3.10) and the addition of a monolayer can often be optically resolved (Figure A3.11), which are indicative of ultrathin materials[33]. This correlation allows facile estimation of the sheets' thickness based on optical images without damaging the sample during AFM measurements. Moreover, the surface roughness of these sheets is as small as ~0.4 nm, which is comparable to the underlying substrate.

A clean and smooth surface over large areas (Figure A3.9, A3.10) is a prerequisite for fabricating intimate heterojunctions via mechanical stacking described later. Therefore, these directly grown nanosheets have advantages over exfoliated flakes of RP perovskites that usually come with many fragments and loose particles. These thin perovskite sheets are volatile and unstable under intense laser illumination, but their photostability can be significantly improved by coating with a protective polystyrene film. The optical studies presented in the rest of this work were thus carried out on encapsulated samples.

4.3.3 Deterministic fabrication of arbitrary vertical heterostructures of RP perovskites

The facile and reliable transfer technique allows deterministic fabrication of arbitrary vertical heterostructures via sequential transfer and stacking processes with control over alignment under an optical microscope (see details in Methods and Figure A3.12). We take advantage of the great diversity of RP perovskites (Fig. 4.1b) and create a range of vertical heterostructures using different RP perovskites that vary in halide anion, *n* phase, LA (Fig. 4.3a-c) and/or A cations (Figure A3.16). In contrast to TMDs, the 2D quantum confinement in RP perovskites are rendered by the organic cations, and the physical behaviors arising from the heterointerfaces are not impacted even if the component sheets are not monolayers, so long as they are not too thick (such as in bulk single crystals) to drown out the effects of the heterointerfaces. We demonstrate several previously inaccessible representative types of heterostructures that exhibit interesting interlayer properties.

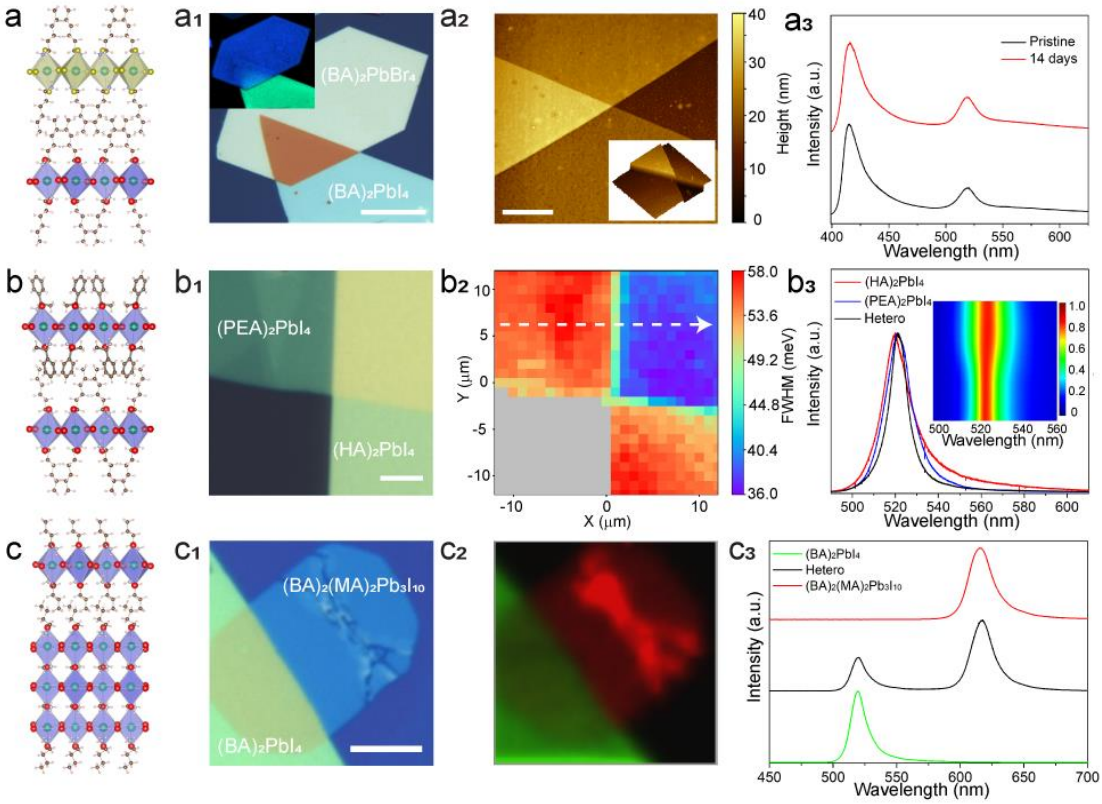

Figure 4.3 Fabrication and characterization of several types of vertical heterostructures of 2D RP perovskite

Schematic for vertical heterostructures of 2D RP perovskite $(LA)_2(A)_{n-1}Pb_nX_{3n+1}$ with varied X **(a)**, LA **(b),** *n* phase **(c)**. Note the schemes do not imply there is only one layer of each component phase, but the number of layers does not change the electronic structure and PL properties of 2D perovskites. **a_1,** Optical image of a $(BA)_2PbBr_4/(BA)_2PbI_4$ heterostructure on Si/SiO_2 substrate. Inset shows a real-color image of the heterostructure under UV LED excitation. Scale bar: 25 μm. **a_2,** AFM image of the heterostructure. Inset shows the 3D height landscape. Scale bar: 2 μm. **a_3,** PL spectra of the as-fabricated heterostructure (black) and after 14 days (red). **b_1,** Optical image of a $(PEA)_2PbI_4/(HA)_2PbI_4$ heterostructure on Si/SiO_2 substrate. Scale bar: 10 μm. **b_2,** PL line width mapping on this heterostructure. **b_3,** Normalized PL spectra taken at the $(HA)_2PbI_4$ region (red), $(PEA)_2PbI_4$ region (blue) and heterostructure (black). The inset shows a PL line-scan taken along the dashed arrow in **(b_2)**. Optical image **c_1,** and the corresponding PL mapping **c_2,** of a

$(BA)_2PbI_4/(BA)_2(MA)_2Pb_3I_{10}$ heterostructure. In the PL mapping, green represents emission integrated from 515 to 525 nm; red represents emission integrated from 615 to 625 nm. Scale bar: 10 μm. **c3,** Normalized confocal PL spectra taken at $(BA)_2PbI_4$ region (green), $(BA)_2(MA)_2Pb_3I_{10}$ region (red) and heterostructure (black), respectively.

An atomically clean and sharp interface is essential to achieving the desired heterostructure properties. The soft crystal lattice of RP perovskites, the flexible LA ligands at the surface, as well as the large-area smooth sheets from the floating growth, ensure intimate interaction in the stacked van der Waals heterostructures. Fig. 4.3a_1 shows an optical image of a heterostructure made of a thin sheet of $(BA)_2PbBr_4$ stacked on top of $(BA)_2PbI_4$. Such heterostructures of different halide anions were previously impossible due to the facile formation of mixed halide alloys[24,25]. The uniform PL (inset) of the heterostructure confirms the integrity of the two quantum wells after stacking. Previous studies in heterostructures of 2D materials showed that the van der Waals forces between adjacent layers can effectively squeeze out water molecules or other contaminants that are inevitably present on individual layers before integration[34]. Compared to TMDs with rigid covalent backbones, we expect this effect to be more pronounced in the RP perovskites, because their labile ionic lattices render them molecularly soft and easy to laminate[35]. In addition, the hydrophobic tails of the LA ligands that face away from the $[PbX_6]$ layers help ensure the expulsion of water. Indeed, the corresponding AFM image (Fig. 4.3a_2) exhibits a smooth heterostructure region with no obvious observation of air/water bubble inclusions. The 3D landscape (inset) shows a sharp heterointerface, further demonstrating the softness and compliance of perovskite sheets. SEM on a different heterostructure (Figure A3.13) also confirms the conformal contact between these perovskite thin sheets. Furthermore, the 2D heterojunctions here are stable for weeks when stored in desiccators at room temperature. The PL spectrum collected

on the heterostructure region (Fig. 4.3a$_3$) shows dual emission peaks at 413 nm and 520 nm, corresponding to $(BA)_2PbBr_4$ and $(BA)_2PbI_4$, respectively. These two emission peaks did not shift over time, indicating negligible ion interdiffusion. This is in sharp contrast to the fast anion interdiffusion across the 3D $CsPbX_3$ heterostructures with different halides[26,27]. We attribute the stable junction to the presence of organic LA cations acting as diffusion barriers to prevent ion migration[36].

The excitonic emission that results in narrow PL emissions in RP perovskites is influenced by structural disorder, exciton-phonon interactions and dielectric environment, all of which are affected by the identity of LA cations and their packing interactions between the soft RP perovskite layers[37]. To explore this molecular tunability unique to RP perovskites quantum wells, we fabricated a heterostructure of $(PEA)_2PbI_4/(HA)_2PbI_4$ (Fig. 4.3b). Because both phases have a single PbI_4^{2-} layer (i.e. n = 1), their emissions occur at around 520 nm with a slight difference. However, PL mapping on the heterostructure and the subsequent PL peak analysis (Fig. 4.3b$_2$, Figure A3.14) reveal that the FWHM in the heterostructure is significantly reduced (~40 meV) compared to those in the individual perovskite layers (~60 meV). This change is further illustrated in the confocal PL spectra (Fig. 4.3b$_3$) collected from respective regions and the line-scan along the white dashed arrow in Fig. 4.3b$_2$. Similarly, some reduction in the PL linewidth is also observed in the heterostructure of $(PEA)_2PbI_4/(BA)_2PbI_4$, but is absent in the control samples of $(PEA)_2PbI_4/(PEA)_2PbI_4$ or stacked $(HA)_2PbI_4/(HA)_2PbI_4$ homolayers (Figure A3.15), which confirms that the linewidth narrowing is due to the special hetero-interface instead of any effect brought about by mechanical stacking or the presence of the underlying substrate. Previous reports correlated the PL linewidth in n =1 2D perovskites with molecular rigidity of the LA cations[31,38]. We postulate that the combination of the more ordered crystal structure due to strong π–π

interaction between PEA and a suitable interlayer distance enabled by the more flexibile HA may reduce the overall structural and dielectric disorders in the heterostructure, leading to narrower PL emission. Another notable change is the more symmetric PL profile in the heterostructure region. The tail of the emission peak in RP perovskites has been attributed to strong exciton-phonon coupling[39]. The loss of asymmetry indicates changes in the exciton-phonon interaction, consistent with the hypothesis of reduced structural and dielectric disorders in the heterostructure. More in-depth studies are needed to fully explore the origin of such phenomenon. Lastly, the A cations can affect the structure dynamics and thus the optoelectronics properties of RP perovskites[40-42]. To represent heterostructures with varied A cations, a $(HA)_2(FA)Pb_2I_7/(HA)_2(GA)Pb_2I_7$ heterostructure was fabricated (Figure A3.16).

We also show heterostructures comprising quantum wells of two nonconsecutive *n* numbers (Fig. 4.3c). The PL spectra (Fig. 4.3c$_3$) clearly show distinctive dual-peak emission, corresponding to $n = 1$ and $n = 3$ RP perovskite phases. Previously, heterostructures can only be made with *n* and $n \pm 1$ RP perovskite phases or *n*-phase mixtures with an average *n* value[20-23]. In contrast, we can assemble arbitrary RP phases with the desired *n* phase (bandgap), thicknesses (color intensity) and sequences (Figure A3.17). These heterostructures are capable of the multiple color emissions and full-color tunability necessary for applications involving white-light emission or multiple color lasing. Note that for all of these stacked heterostructures, the exact crystallographic alignment between the two layers at the heterojunction and the effects of such alignment remain unclear, and are intriguing to explore in the future.

4.3.4 Assembly of complex multi-heterostructures

The capability to assemble arbitrary RP perovskite phases with pristine interfaces enables us to fabricate complex multi-heterostructures with rational control over their electronic structures.

Previously, carrier funneling from lower *n* RP phase to higher *n*-phase has been proposed to increase the efficiency in the LEDs made with polycrystalline thin films of those heterostructures[20-22]. However, those junctions are poorly defined because the exact RP phase compositions, stacking sequences, and layer orientations are unknown. Here we demonstrate the fabrication (see details in Figure A3.18) of a unusual tri-layer multi-heterostructure that has shuffled *n*-phases $(BA)_2PbI_4/(BA)_2(MA)_2Pb_3I_{10}/(BA)_2(MA)Pb_2I_7$ (n = 1/ n = 3/n = 2) with well-defined junctions and stacking sequence (Fig. 4.4a) by repeating the transfer and staking procedures described above (Figure A3.12). Fig. 4.4b shows an optical image of the as-fabricated heterostructure in an area where heterojunctions of all combinations are visible and outlined. Confocal PL spectra (Fig. 4.4g) taken in different regions (i-iv) of the heterostructure clearly show a total of three different PL peaks at 520 nm, 575 nm and 618 nm in various combinations, which correspond to the excitonic emissions of n = 1, n = 2, and n = 3 RP phases, respectively. Interestingly, confocal PL mapping on the heterostructure (Fig. 4.4d-f) clearly reveals dramatic changes in the steady-state PL intensities of these three PL peaks in different regions. The 520 nm (green) emission is the strongest (Fig. 4.4d) in region i in Fig. 4.4c, which consists of the topmost n = 1 phase only. This emission decreases in region ii and iii, where additional n = 2 and n = 3 phases are beneath the n = 1 layer, respectively, and eventually becomes marginal in region iv, where all three phases are stacked as n = 1/ n = 3/ n = 2 from top to bottom. Similar trend is observed in the 575 nm (orange) emission mapping (Fig. 4.4e), where the intensity drops from region ii to region iv. In contrast, the 618 nm (red) emission intensity (associated with the n = 3 phase) apparently increases from region iii to region iv (Fig. 4.4f). We could attribute such phenomena to energy transfer from the low *n*-phases to high *n*-phases due to the decreasing bandgaps and type-I band alignments[43] following previous reports[20-23] (illustrated in Fig. 4.4g inset). Furthermore, photoluminescence excitation

(PLE) measurements (see Methods) show enhanced emission from the n = 3 phase when the excitation is in resonance with the n = 1 and n = 2 excitonic energies (Figure A3.19). Time-resolved photoluminescence (TRPL) measurements show the PL lifetimes of the n = 2 and n = 3 phases decreased significantly when they are in the heterostructures (Figure A3.20). While the detailed carrier transfer mechanism(s) entail further investigations and could be dependent on the nature of LA spacer cations, the combination of steady-state PL, TRPL and PLE results strongly supports that the pristine hetero-interfaces present in these vertical heterostructures can efficiently allow carrier transfer between layers. Notably, this phase stacking arrangement of n = 1/ n = 3/ n = 2 with non-neighboring n phases is not "natural" and would not have been possible to control from direct synthesis. As a comparative example, we could also readily fabricate a more "natural" tri-layer multi-heterostructure of n = 1/ n = 2/ n = 3 phases (Figure A3.21). These clearly defined multi-heterostructures with full control over the compositions (n phase, LA and A cations) and sequences can serve as ideal platforms to study the interlayer carrier dynamics.

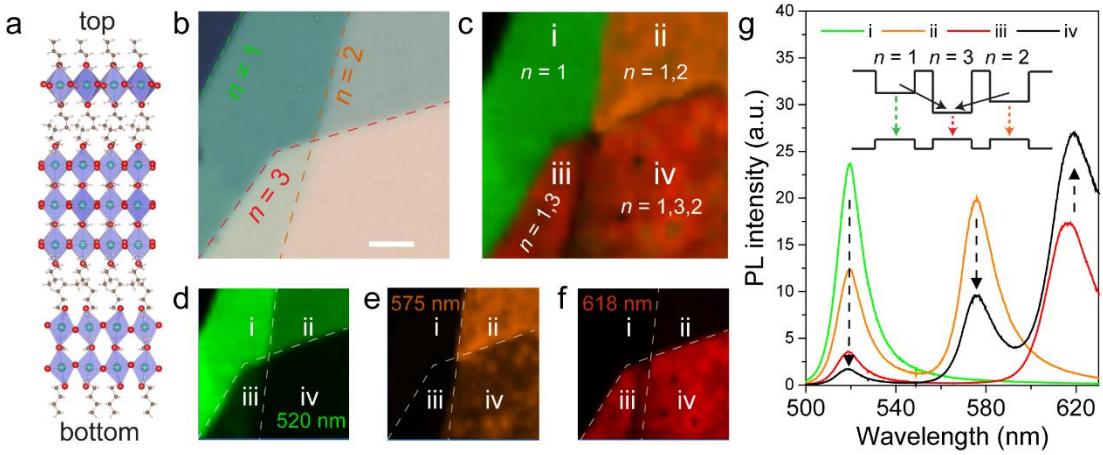

Figure 4.4 Fabrication and characterization of a $(BA)_2PbI_4/(BA)_2(MA)_2Pb_3I_{10}/(BA)_2(MA)Pb_2I_7$ multi-heterostructure.

a, Schematic structure for the multi-heterostructure (abbreviated as n = 1/n = 3/n = 2). Note this scheme illustrates the RP phase sequence but does not imply that there is only one monolayer for

each phase. **b,** Optical image of the heterostructure fabricated on a Si/SiO_2 substrate. The n = 2 layer is at the bottom, whose shape is outlined by orange dashed line. The n = 3 layer is in the middle with the edge marked by red dashed line. The n = 1 layer is on the top covering the other two layers, and its edge is marked by green dashed line. Scale bar: 5 μm. **c-f,** PL mappings of this heterostructure: **c)** Overview mapping image with the four different regions (i-iv) marked together with the n phase found in those regions; **d**) green represents emission integrated from 515 to 525 nm (n = 1); **e**) orange from 570 to 580 nm (n = 2); and **f**) red from 613 to 623 nm (n = 3). **g**, Confocal PL spectra collected in the regions labeled as i-iv in (**c**) more clearly show the PL intensity evolution between different single phase (i) and double layer (ii,iii) and triple layer (iv) structures. Inset shows the schematic band energy diagram of the 3 phases illustrating one possible scenario of energy transfer processes among them.

Our methodology also allows the integration of 2D RP perovskites with conventional 2D materials, such as graphene, hBN, or TMDs. As a proof-of-concept, we fabricated a heterostructure of $(HA)_2PbI_4$ on top of a monolayer of WS_2 grown by chemical vapor deposition[44] (Figure A3.22). Confocal PL spectra confirm the integrity of both layers post-fabrication. The much wider tunability of bandgaps and electronic structures of RP perovskites (see Fig. 4.1c) could enable new heterostructure electronic structure configurations in combinations with TMDs[45]. The more inert 2D materials could also serve as the encapsulation layers to protect the perovskite layers beneath[10].

4.4 Conclusions

We report a floating solution growth method for synthesizing large-area atomically thin sheets of diverse 2D RP lead halide perovskites and show that these floating sheets can be reliably transferred and stacked into 2D vertical heterostructures with clean interfaces. These advances allow the fabrication of arbitrary vertical heterostructures of RP perovskites with unprecedented

degrees of compositional freedom (the halide anions, *n* value, LA and A cations) that in turn control the electronic structure. Furthermore, multi-heterostructures of RP perovskites can be assembled with full control over the compositions and sequence, with the potential addition of other 2D materials such as graphene, hBN, or TMDs. The tunability of the electronic structure (the *n* value and halide anions) and dielectric environments (LA cations) enable the observation of interlayer carrier transfer and narrowing of photoluminescence linewidth, and make these RP perovskite heterostructures a new and versatile platform to explore exciton physics, such as exciton-exciton interactions and Bose-Einstein condensation of excitons[7,8]. This work gives access to a diverse library of 2D building blocks based on RP perovskites and represents an important technological breakthrough for fabricating artificial semiconductor quantum well heterostructures. It also opens up opportunities for studying the intrinsic properties and unusual photophysics, and eventually exploiting the high-performance optoelectronic applications of these heterostructures.

4.5 Methods

4.5.1 Growth of large-area thin sheets of 2D RP perovskites

All chemicals were purchased from Sigma-Aldrich and used as received unless otherwise stated.

2D RP perovskite thin sheets were synthesized using an interfacial growth method, with the precursor species, concentrations, and ratios carefully optimized and the crystallization temperature carefully controlled in order to promote layer-by-layer growth, avoid dislocation formation, maximize lateral growth, and maintain phase purity. An exemplary synthesis for $(HA)_2PbI_4$ (n = 1) (HA is *n*-hexylammonium) is described below:

PbI_2 (0.45 M) and HAI (0.05 M) precursors were dispersed in a concentrated aqueous solution of HI and H_3PO_2 mixture (10:1 vol/vol), and then heated at 130 °C in a closed glass vial until a

clear yellow solution was obtained. The solution was cooled down to 28 °C and kept at that temperature in a closed vial in a convention oven as the stock solution. 2 μL of this warm supernatant solution was collected and dispensed with a 10 μL pipette onto a glass slide placed in open ambient environment (22 °C). Nucleation and growth quickly initiated on the surface of the precursor solution droplet and perovskite thin sheets floating on the solution droplets were obtained within a few seconds up to 30 s. Such growth process on the surface of the droplet on glass slides can be observed directly under an optical microscope to monitor the growth process, which resulted in the Supplementary Videos.

The recipes for other RP perovskite phases and the temperatures from which the supernatant was cooled from are summarized in Appendix Table A3.1. The lateral size and thickness of representative nanosheet products are presented in Figure A3.2 and A3.3. Occasionally the sheets of some lower *n*-phase RP perovskites can grow to up to mm size, limited by the lateral dimensions of the water droplets.

4.5.2 Transfer and fabrication of 2D RP perovskite heterostructures.

Step 1: *Pick-up of the perovskite thin sheets (refer to Fig. 4.2a).* Thin sheets of 2D RP perovskites grown at the solution-air interface are picked up by gently touching the droplet surface with a polydimethylsiloxane (PDMS) stamp (purchased from GelPak, PF-30-X4). The PDMS stamp was kept approximately horizontally before contact to better receive the perovskite thin sheets and minimize mechanical damage to the sheets.

Step 2: Transferring the perovskite thin sheets. The thin perovskite sheets can be transferred onto arbitrary receiving substrates including glass, quartz or Si/SiO_2 substrates using a home-built transfer stage apparatus (Figure A3.12e) through a simple lamination process. Specifically, the substrate is first fixed onto a Z stage, and PDMS stamp with perovskite phase 1 is mounted on the

XY stage and placed above the substrate with the perovskite side facing down. The substrate is then brought up by the Z stage. After the perovskite thin sheets are completely laminated on the substrate, retracting the substrate slowly results in the transfer of these sheets from PDMS onto the substrate.

Step 3: Fabrication of heterostructures. Following step 2 which yields perovskite phase 1 sheet on the substrate (Figure A3.12a), a second PDMS stamp covered with the sheets of perovskite phase 2 that are picked up from another droplet synthesis is aligned over a chosen phase 1 flake under the optical microscope (Figure A3.12b) with some separation between the surfaces. (The perovskite sheets are visible through the transparent PDMS stamp under optical microscope). The substrate is then brought up again until the polymer comes into contact with the substrate and the two perovskite sheets meet (Figure A3.12c). When fully in contact, the substrate is retracted slowly and the heterostructures of two perovskite phases remain on the substrate (Figure A3.12d). Moving the Z-stage too fast may result in non-conformal contact between the two perovskites, as well as damage to the thin sheets.

A polystyrene (average M_w 280,000, 4 wt% in toluene, Sigma-Aldrich) protection layer is spin-coated onto the substrate at 3000 rpm for 30 s to encapsulate the transferred perovskite sheets before optical characterizations.

4.5.3 Structural characterizations

The optical images were obtained on an Olympus BX51M optical microscope. The real-color PL images were acquired on the same microscope with UV illumination from a household handheld UV LED flashlight (400 nm, 3 W). The scanning electron microscopy (SEM) images were collected on a LEO SUPRA 55 VP field-emission scanning electron microscope operated at 3 kV. The PXRD patterns were collected on crystals settled at the bottom of the growth vials using

a Bruker D8 Advance X-ray diffractometer with Cu Kα radiation. Atomic force microscopy (AFM) was performed using an Agilent 5500 AFM in tapping mode using NCHV-A tips from Bruker AFM Probes (k: 40 N/m).

4.5.4 Steady-state photoluminescence (PL) characterization

Point PL spectra, PL line scans, and PL mappings were collected with a Horiba Labram Aramis confocal Raman microscope at ambient conditions in PL mode using a 442 nm CW He/Cd laser. The laser beam was attenuated by neutral filters and focused on to the sample via a 50× objective, producing a spot diameter of ~1 μm, giving an estimated laser power of 300 W/cm^2. The samples are protected by polystyrene, and are stored in desiccators at room temperature between measurements.

The low-temperature power dependent PL measurements were performed on a home-built far-field epifluorescence microscope set-up (Olympus IX73 inverted microscope) with a 450 nm continuous wave laser (MDL-III-450-1W) as the excitation source. Each sample was mounted in a cryostat (Cryo Industries of America, RC102-CFM Microscopy Cryostat) which was evacuated to pressures $<10^{-7}$ mbar using a turbo pump (Varian). The measurements were taken at 77 K with an active flow of liquid nitrogen. The excitation was focused onto the sample by a 40× objective (NA 0.6) with correction collar (Olympus, LUCPLFLN40X). The emission was collected by the same objective and focused into a spectrograph (Princeton Instruments, Acton SP2300i) and detected by a liquid-nitrogen-cooled CCD camera (Princeton Instruments, InGaAs PyLoN-IR 1024-1.7).

4.5.5 PL quantum yield (PLQY) measurements

For estimation of PLQY of the nanosheets, a standard dye (Rhodamine 6G, R6G) with known PLQY was dispersed in PMMA matrix and used as a reference sample film. Confocal PL

measurements on the reference thin film and perovskite nanosheets were conducted with a Horiba Labram Aramis confocal PL/Raman microscope using a 442 nm laser. The laser was attenuated by neutral filters and focused to the sample via a 50× objective, producing a spot with a diameter of ~ 1 μm and an excitation power ~ 100 W/cm^2. The absorbance of RP perovskite nanosheets and the reference thin film was obtained from the attenuation of excitation light measured by a standard photodiode (Thorlabs S120 VC). The PLQY of the of the RP perovskite nanosheets was thus estimated using the following equation:

$$\emptyset_{RP} = \emptyset_{ref} \frac{I_{RP}^{PL}/A_{RP}}{I_{ref}^{PL}/A_{ref}} F_{sp}$$

Where $\emptyset_{RP}$ is PLQY of the RP perovskite nanosheet of interest; $\emptyset_{ref}$ is PLQY of the reference dye (R6G) obtained from the literature[46] (9%); I_{RP}^{PL} and I_{ref}^{PL} are the PL intensity of the RP perovskite nanosheet and the reference dye measured under the microscope, respectively; A_{RP} and A_{ref} are the absorbance of the RP perovskite nanosheet and the reference dye, respectively, obtained by measuring the excitation attenuation; F_{sp} is the calibration factor due to the wavelength dependence of the sensitivity of the CCD spectrometer. Here, because the emission wavelength of the reference dye (555 nm) is very close to the RP perovskites phases (520 nm for n = 1, 570 nm for n = 2), *Fsp* is approximated as 1.

4.5.6 Time-resolved PL (TRPL) spectroscopy

An 800-nm output of a mode-locked Ti:Sapphire laser (Coherent Vitesse) was doubled in frequency using a BBO crystal to produce pulses at 400 nm, 100-fs FWHM, and 80 MHz. Light was slightly de-collimated and through a 20× Olympus objective lens, such that a spot size of about 80 μm^2 was created on the sample surface. PL emission was collected through the same lens, and a 410 nm long pass filter was placed before the monochromator slit. The PL output was

spectrally resolved by a spectrograph (Princeton Instruments, Acton SP2300i, 150 grooves/mm, 800-nm blaze wavelength) and directed either towards a 2D array detector (Andor, Neo sCMOS) for steady-state PL or an avalanche photodiode (IDQ ID-100) connected to a time-correlated single-photon counting module (Becker & Hickl, SPC-130) for TRPL.

4.5.7 Photoluminescence excitation (PLE) spectroscopy

Discrete-wavelength PLE spectroscopy was performed at room temperature using a Xenon arc lamp (Varian, Eimac, 300 W) fitted with a series of 10-nm FWHM band pass filters to produce light ranging from 490 to 570 nm in wavelength. For each desired excitation wavelength, a primary band pass filter and, when necessary for additional filtering, a secondary short-pass filter were placed on the exit of the chamber containing the light source. In addition, to selectively excite the n = 3, but not the n = 2, RP perovskite phase, a 590-nm bandpass filter and a 580-nm bandpass filter were combined to yield light at 584 nm (FWHM = 4 nm). Light was directed to the sample via a 100× Olympus objective, and photoluminescence was collected through the same objective and focused onto the slit of a spectrograph (Princeton Instruments, Acton SP2300i), where it was detected by a 2D array detector (Andor, Neo sCMOS). A 620-nm bandpass filter was placed in front of the spectrograph entrance slit to isolate the emission from the $n = 3$ RP perovskite phase.

4.6 References

1 Mao, L., Stoumpos, C. C. & Kanatzidis, M. G. Two-Dimensional hybrid halide perovskites: principles and promises. *J. Am. Chem. Soc.* **141**, 1171-1190 (2019).

2 Fu, Y. *et al.* Metal halide perovskite nanostructures for optoelectronic applications and the study of physical properties. *Nat. Rev. Mater.* **4**, 169-188 (2019).

3 Stranks, S. D. & Snaith, H. J. Metal-halide perovskites for photovoltaic and light-emitting devices. *Nat. Nanotechnol.* **10**, 391-402 (2015).

4 Katan, C., Mercier, N. & Even, J. Quantum and dielectric confinement effects in lower-dimensional hybrid perovskite semiconductors. *Chem. Rev.* **119**, 3140-3192 (2019).

5 Charbonneau, S., Thewalt, M. L., Koteles, E. S. & Elman, B. Transformation of spatially direct to

spatially indirect excitons in coupled double quantum wells. *Phys. Rev. B Condens. Matter.* **38**, 6287-6290 (1988).

6 Golub, J. E., Kash, K., Harbison, J. P. & Florez, L. T. Long-lived spatially indirect excitons in coupled GaAs/AlxGa1-xAs quantum wells. *Phys. Rev. B Condens. Matter.* **41**, 8564-8567 (1990).

7 Butov, L. V., Zrenner, A., Abstreiter, G., Bohm, G. & Weimann, G. Condensation of indirect excitons in coupled AlAs/GaAs quantum wells. *Phys. Rev. Lett.* **73**, 304-307 (1994).

8 Butov, L. V. *et al.* Stimulated scattering of indirect excitons in coupled quantum wells: signature of a degenerate Bose-gas of excitons. *Phys. Rev. Lett.* **86**, 5608-5611 (2001).

9 Blancon, J. C. *et al.* Scaling law for excitons in 2D perovskite quantum wells. *Nat. Commun.* **9**, 2254 (2018).

10 Leng, K. *et al.* Molecularly thin two-dimensional hybrid perovskites with tunable optoelectronic properties due to reversible surface relaxation. *Nat. Mater.* **17**, 908-914 (2018).

11 Wang, J. *et al.* Room temperature coherently coupled exciton-polaritons in two-dimensional organic-inorganic perovskite. *ACS Nano* **12**, 8382-8389 (2018).

12 Dou, L. T. *et al.* Atomically thin two-dimensional organic-inorganic hybrid perovskites. *Science* **349**, 1518-1521 (2015).

13 Gao, Y. *et al.* Molecular engineering of organic-inorganic hybrid perovskites quantum wells. *Nat. Chem.* **11**, 1151-1157 (2019).

14 Novoselov, K. S., Mishchenko, A., Carvalho, A. & Castro Neto, A. H. 2D materials and van der Waals heterostructures. *Science* **353**, aac9439 (2016).

15 Liu, Y., Huang, Y. & Duan, X. F. Van der Waals integration before and beyond two-dimensional materials. *Nature* **567**, 323-333 (2019).

16 Rivera, P. *et al.* Interlayer valley excitons in heterobilayers of transition metal dichalcogenides. *Nat. Nanotechnol.* **13**, 1004-1015 (2018).

17 Mak, K. F. & Shan, J. Opportunities and challenges of interlayer exciton control and manipulation. *Nat. Nanotechnol.* **13**, 974-976 (2018).

18 Wang, J. *et al.* Controllable synthesis of two-dimensional Ruddlesden-Popper-type perovskite heterostructures. *J. Phys. Chem. Lett.* **8**, 6211-6219 (2017).

19 Wang, J. *et al.* Controllable growth of centimeter-sized 2D perovskite heterostructures for highly narrow dual-band photodetectors. *ACS Nano* **13**, 5473-5484 (2019).

20 Yuan, M. *et al.* Perovskite energy funnels for efficient light-emitting diodes. *Nat. Nanotechnol.* **11**, 872-877 (2016).

21 Proppe, A. H. *et al.* Synthetic control over quantum well width distribution and carrier migration in low-dimensional perovskite photovoltaics. *J. Am. Chem. Soc.* **140**, 2890-2896 (2018).

22 Wang, N. N. *et al.* Perovskite light-emitting diodes based on solution-processed self-organized multiple quantum wells. *Nat. Photon.* **10**, 699-704 (2016).

23 Fu, Y. *et al.* Multicolor heterostructures of two-dimensional layered halide perovskites that show interlayer energy transfer. *J. Am. Chem. Soc.* **140**, 15675-15683 (2018).

24 Zhu, H. *et al.* Lead halide perovskite nanowire lasers with low lasing thresholds and high quality factors. *Nat. Mater.* **14**, 636-642 (2015).

25 Ma, D. *et al.* Single-crystal microplates of two-dimensional organic–inorganic lead halide layered perovskites for optoelectronics. *Nano Research* **10**, 2117-2129 (2017).

26 Pan, D. *et al.* Visualization and studies of ion-diffusion kinetics in cesium lead bromide perovskite nanowires. *Nano Lett.* **18**, 1807-1813 (2018).

27 Lai, M. L. *et al.* Intrinsic anion diffusivity in lead halide perovskites is facilitated by a soft lattice. *P. Natl. Acad. Sci. USA* **115**, 11929-11934 (2018).

28 Shi, E. Z. *et al.* Two-dimensional halide perovskite lateral epitaxial heterostructures. *Nature* **580**, 614-620 (2020).

29 Meng, F., Morin, S. A., Forticaux, A. & Jin, S. Screw dislocation driven growth of nanomaterials. *Acc. Chem. Res.* **46**, 1616-1626 (2013).

30 Liang, D. *et al.* Color-Pure Violet-light-emitting diodes based on layered lead halide perovskite nanoplates. *ACS Nano* **10**, 6897-6904 (2016).

31 Gong, X. W. *et al.* Electron-phonon interaction in efficient perovskite blue emitters. *Nat. Mater.* **17**, 550-556 (2018).

32 Meitl, M. A. *et al.* Transfer printing by kinetic control of adhesion to an elastomeric stamp. *Nat. Mater.* **5**, 33-38 (2005).

33 Blake, P. *et al.* Making graphene visible. *Appl. Phys. Lett.* **91**, 063124 (2007).

34 Haigh, S. J. *et al.* Cross-sectional imaging of individual layers and buried interfaces of graphene-based heterostructures and superlattices. *Nat. Mater.* **11**, 764-767 (2012).

35 Tu, Q. *et al.* Out-of-plane mechanical properties of 2D hybrid organic-inorganic perovskites by nanoindentation. *ACS Appl. Mater. Interfaces* **10**, 22167-22173 (2018).

36 Lin, Y. *et al.* Suppressed ion migration in low-dimensional perovskites. *ACS Energy Lett.* **2**, 1571-1572 (2017).

37 Mauck, C. M. & Tisdale, W. A. Excitons in 2D organic–inorganic halide perovskites. *Trends in Chemistry* **1**, 380-393 (2019).

38 Zhang, S. *et al.* Synthesis and optical properties of novel organic–inorganic hybrid nanolayer structure semiconductors. *Acta. Mater.* **57**, 3301-3309 (2009).

39 Ni, L. M. *et al.* Real-time observation of exciton-phonon coupling dynamics in self-assembled hybrid perovskite quantum wells. *ACS Nano* **11**, 10834-10843 (2017).

40 Fu, Y. *et al.* Incorporating large A cations into lead iodide perovskite cages: Relaxed Goldschmidt tolerance factor and impact on exciton-phonon interaction. *ACS Cent. Sci.* **5**, 1377-1386 (2019).

41 Herz, L. M. How lattice dynamics moderate the electronic properties of metal-halide perovskites. *J.*

Phys. Chem. Lett. **9**, 6853-6863(2018).

42 Hautzinger, M. P. *et al.* Band edge tuning of two-dimensional Ruddlesden–Popper perovskites by A cation size revealed through nanoplates. *ACS Energy Lett.* **5**, 1430-1437 (2020).

43 Spanopoulos, I. *et al.* Uniaxial expansion of the 2D Ruddlesden-Popper perovskite family for improved environmental stability. *J. Am. Chem. Soc.* **141**, 5518-5534 (2019).

44 Zhao, Y. & Jin, S. Controllable water vapor assisted chemical vapor transport synthesis of WS_2–MoS_2 heterostructure. *ACS Mater. Lett.* **2**, 42-48 (2019).

45 Chen, Y. *et al.* Robust interlayer coupling in two-dimensional perovskite/monolayer transition metal dichalcogenide heterostructures. *ACS Nano* **14**, 10258-10264 (2020).

Chapter 5 Structural and Property Modulation in 2D Ruddlesden-Popper Lead Iodide Perovskites by Large A-cations[3]

5.1 Abstract

Two-dimensional (2D) Ruddlesden halide perovskites merit the excellent optoelectronic properties from the 3D halide perovskites, and exhibit great structural tunability that in turn determines the properties thanks to their unique modular structures. Particularly, it has been shown that the Goldschmidt tolerance factor is relaxed in 2D perovskite which allows large A-cations to be incorporated into the structures. It is thus of great interest to investigate how the A-cations modulate crystal structures which significantly impact the materials' electronic and optical properties. Herein, we report the synthesis of 3 new 2D iodide perovskites Here we report the synthesis of 3 new *n* = 2D RP lead iodide perovskites $(PA)_2(EA)Pb_2I_7$, $(PA)_2(DMA)Pb_2I_7$, and $(PA)_2(AA)Pb_2I_7$ (PA = pentylammonium, EA = ethylammonium, DMA = dimethylammonium, AA = acetamidinium), and the crystal structures of the latter two. Structural analysis in combination with other previously reported $(PA)_2(A)Pb_2I_7$ perovskites reveal size of the A-cation is not the sole determining factor, and the polarity and shape of the A-cation also affect how they interact and distort the inorganic lattice. This is clearly manifested by the largest-cation-containing $(PA)_2(AA)Pb_2I_7$ showing shorter average Pb-I bonds and smaller cage volume that those of $(PA)_2(FA)Pb_2I_7$. Additionally, we found the bandgaps of the materials increases as the average Pb-I length increases and average Pb-I-Pb bond angles further deviate from 180°, in agreement with DFT calculations. The large A-cations also cause decreased PL lifetimes and larger PL FWHM. Finally, we investigated symmetry of the crystal structures and analyzed the level of distortion in

[3] Dongxu Pan, Kyana M. Sanders, Willa Mihalyi-Koch, Zhenbang Dai, David Lafayette, Ilia Guzei, Andrew M. Rappe, J. C. Wright, and S. Jin, *In preparation*

the inorganic lattice in each $(PA)_2(A)Pb_2I_7$, and supplemented by second-harmonic generation (SHG) measurements, in order to examine the potential ferroelectricity.

5.2 Introduction

Metal halide perovskites have drawn significant research interest in the past decade as promising semiconductors for photovoltaic and optoelectronic applications due to their excellent optical and electronic properties.[1,2] The three-dimensional (3D) lead iodide perovskites $APbI_3$ feature a corner sharing Pb-I octahedral framework with an A-cation, usually a small monovalent cation, occupying the cuboid formed by 8 $[PbI_6]^{4-}$ octahedra, referred to here as the "perovskite cage". It is commonly believed that the A-cation component does not contribute directly to the band structure of halide perovskite.[3,4] However, the A-cation can modulate the inorganic lattice and induce local structural fluctuations which significantly impact the materials' electronic and optical properties, including carrier lifetimes and carrier diffusion lengths.[5-7] For example, incorporation of mixed cations has been shown to boost solar conversion efficiency and stability of perovskite solar cells.[8-11]

The range of A-cations that can be incorporated into 3D lead iodide perovskites is limited. The Goldschmidt tolerance factor $t = (r_A + r_X)/\sqrt{2}(r_B + r_X)$[12,13], where r_A, r_B and r_X are the ionic radii of the A, B, and X ions, respectively, predicts that only structures with $0.8 < t < 1$ will form stable perovskites. Within the 3D lead iodide perovskites widely used for photovoltaic applications, only $MAPbI_3$ (t~0.912) is considered a stable perovskite structure, while the $FAPbI_3$ (t~0.99) and $CsPbI_3$ (t~0.81) phases are at the upper and lower limits in this range and are only metastable at room temperature.[14]

Recently, it has been shown that A-cations that are too large to be incorporated into the 3D perovskite cage, including ethylammonium (EA), dimethylammonium (DMA), guanidinium (GA),

can form stable 2D Ruddlsden-Popper (RP) perovskites.[15] The crystal structures of 2D RP perovskite can be derived by slicing the 3D perovskite along the (100) with long-chain organic cations. The successful accommodation of these large cation is enabled by the addition of flexible long-chain organic cations in between the inorganic lattice which can readily compensate the tensile strain exerted by the expanded perovskite cage by applying compressive strain.[16] This relaxation on the Goldschmidt tolerance factor has been unambiguously demonstrated by quite a few crystallographically well-characterized 2D iodide lead perovskites such as (n-$C_6H_{13}NH_3)_2(GA)Pb_2I_7$[16], ($n$-$C_4H_9NH_3)_2(A)Pb_2I_7$ (A = GA, DMA)[17], and (n-$C_4H_9NH_3)_2(EA)_2Pb_3I_{10}$[18,19]. These 2D perovskites with large A-cations exhibit intriguing structural characteristics such as lattice expansion and highly distorted Pb-I octahedra, which lead to decreased PL intensities, shorter PL lifetimes and increased bandgaps.[16-18] It is also predicted that the incorporation of large A-cations would induce ferroelectricity, exemplified experimentally in (n-$C_4H_9NH_3)_2(EA)_2Pb_3I_{10}$[19], which is a topic under intense investigation. Ferroelectric disorder arises from the Pb^{2+}-off-centering due to stereochemical expression of the Pb^{2+} $6s^2$ electron pairs and the tendency towards this distortion increases with A-cation size .[20] However, observation of ferroelectricity is still uncommon in 2D RP lead iodide perovskites and it remains unclear the specific mechanism by which different A-cations modulate the lattice resulting in ferroelectricity. In addition, there have been several proposed explanations of the high-performance of halide perovskites, such as local ferroelectric domains[21], large polaron formation[22,23], and Rashba effect[24] that are closely related to the dynamic disorder, polarity and size of the A-cation. Therefore, a materials system that allows systematic study of impact of A-cations and the structure-property relationships in these 2D RP perovskite is highly desired.

Here we report the synthesis of 3 new *n* = 2D RP lead iodide perovskites $(PA)_2(EA)Pb_2I_7$, $(PA)_2(DMA)Pb_2I_7$, and $(PA)_2(AA)Pb_2I_7$, with the crystal structures of the latter two solved. In combination with previously reported $(PA)_2(MA)Pb_2I_7$[25], $(PA)_2(FA)Pb_2I_7$[26,27], and $(PA)_2(GA)Pb_2I_7$[27] structures, we obtained a whole series of 6 different $(PA)_2(A)Pb_2I_7$, which allowed us to systematically study how the A-cations influence the crystal structures and thereby the optoelectronic and ferroelectric properties in halide perovskites in general. We found that in contrast to commonly observed Pb-I elongation and cage expansion, the largest-cation-containing $(PA)_2(AA)Pb_2I_7$ shows shorter average Pb-I bonds and smaller cage volume that those of $(PA)_2(FA)Pb_2I_7$. Accompanying the shorter bonds is highly bent axial and equatorial Pb-I-Pb bonds, and most distorted $[PbI_6]$ octahedra, characterized by the largest bond length and bond angle variances. Further analysis reveals that in contrast to the non-polar GA cation, DMA and AA cause the perovskite cage to adapt to their shape and dipole, and stretch unevenly, which lead to the highly distorted Pb-I framework and anisotropic lattice parameters. As a result, large "Pb-off-centering" is observed in DMA and AA, but the presence of ferroelectricity is still unclear. We also found as the Pb-I length increases and average Pb-I-Pb bond angles further deviate from 180°, the bandgap of the materials increases in agreement with DFT calculation, and the PL lifetime decreases and the PL width increases. These results confirm that tolerance factor based on spherical A-cation size estimations works less effectively in halide perovskites, and the shape and dipole of the organic cations also play important role in the structural and subsequent property modulations.

5.3 Results and Discussion

Synthesis. Single crystals of $(PA)_2(A)Pb_2I_7$ (PA = pentylammonium, A = methylammonium (MA), formamidinium (FA), dimethylammonium (DMA), ethylammonium (EA), guanidinium

(GA), and acetamidinium (AA)) were synthesized via a solution growth method reported previously[15] with optimized recipes and conditions specified in Table S1. Briefly, PbO and AI salts were dissolved in a concentrated HI solution at 125 °C in a silicone oil bath before certain amount of pentylamine was added. After a clear solution was obtained, it was cooled to room temperature, which led to the precipitation of red $n = 2$ flaky crystals, photos of which are shown in Figure 5.1b. Powder X-ray diffraction (PXRD) on the crystals (Figure 5.1c) clearly show the characteristic (00*l*) peaks at around 4.3°, 8.6°, etc., corresponding to the $n = 2$ phases. There are no other peaks observed in each pattern, indicating the layered nature of these crystals and the absence of other *n* phases. The confocal PL spectra (Figure 5.1d) taken on the crystals reveal a dominant excitonic peak located at ~560 nm, as expected from the quantum-confined $n = 2$ $(PA)_2(A)Pb_2I_7$. The PL peak energy and peak width vary slightly in different compounds, which will be discussed extensively below. For the following discussions, we will abbreviate $(PA)_2(A)Pb_2I_7$ as A for brevity (For example, $(PA)_2(MA)Pb_2I_7$ will be referred to as MA).

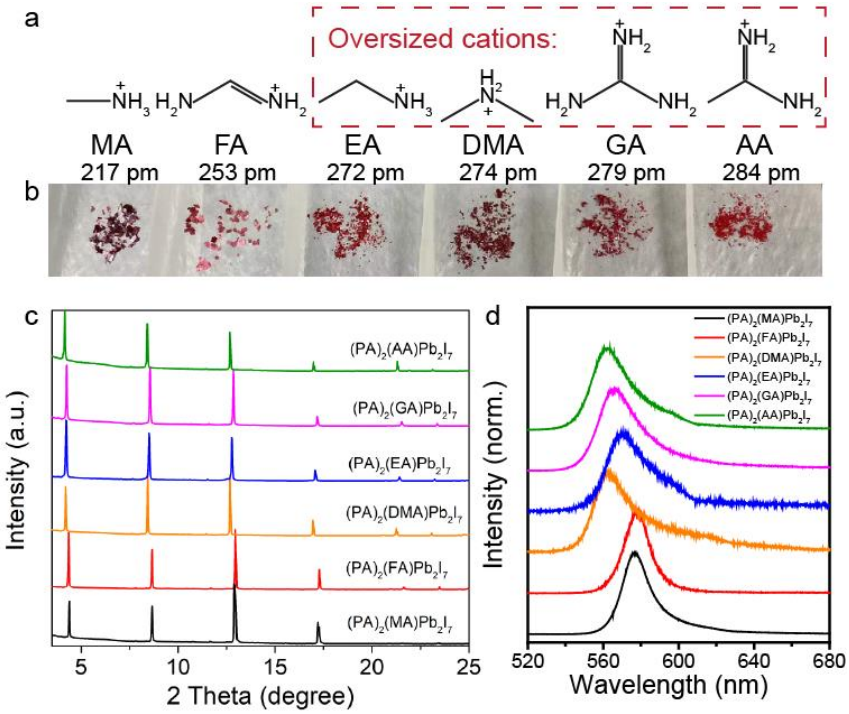

Figure 5.1 Formation of $(PA)_2(A)Pb_2I_7$ 2D RP perovskites.
(a) Structure and size of the various A-cations used. The oversized cations as dictated by the Goldschmidt Tolerance factor are marked by the red-dashed box. (b) Photos of the corresponding $(PA)_2(A)Pb_2I_7$ red crystals. (c) PXRD patterns of the $(PA)_2(A)Pb_2I_7$ reported here. (c) PL spectra of $(PA)_2(A)Pb_2I_7$ reported here.

We found controlling the relative concentrations of PA and A cations was the key to obtaining phase-pure $n = 2$ crystals. Due to the delicate thermodynamic equilibria and crystallization kinetics, $n = 1$ or $n = 3$ crystals may form under non-ideal conditions. To efficiently find the optimal synthetic window for obtaining the $n = 2$ phase in such complex system, we kept the concentration of Pb^{2+} to be 0.5 M, and tuned [PA] and [A] (Figure A4.1). Overall, the tendency to form $n > 1$ phases increases as [A] increase, and an excess amount of [PA] favors the formation of $n = 1$ phase. The optimal [A] to [Pb] ratio we found for getting phase-pure $n = 2$ crystals deviate from that dictated by their chemical formulae, and the range of suitable synthetic window varies for each A-cation. For MA and FA, the suitable windows for getting $n = 2$ crystals are quite broad, owing to

the large solubilities of MAI and FAI in HI and ease of their n = 2 phases formation. For EA, even though EAI is similarly soluble, the window for getting the pure n = 2 phase without n = 3 impurities is pretty narrow, indicating the n = 3 phases may be thermodynamically more favorable. We would like to note that we attempted to grow $(BA)_2(EA)Pb_2I_7$ and $(HA)_2(A)Pb_2I_7$ (BA=butylammonium, HA=hexylammonium), but only the n = 3 phases were observed across wide synthetic condition windows. This is in agreement with the fact that all EA-containing RP perovskites reported so far have been of n = 3 phase,[18,19,28] and may be due to the unique ability of PA to accommodate the strain induced by EA. More crystallographic data are needed to elucidate the mechanism. DMA, GA and AA salts are much less soluble in HI, and we found more PA are needed to dissolve similar amount of AI, by forming the more soluble $(PA)_2(A)Pb_2I_7$ perovskites. We did not observe any n > 3 $(PA)_2(A)_{n-1}Pb_nI_{3n+1}$ formation when varying the precursor concentrations in DMA, GA and AA syntheses (Figure A4.1).

Crystal structures. The two new crystal structures of DMA and AA were refined in the space group of $P2_1$ (noncentrosymmetric), and $C2/c$ (centrosymmetric), respectively. (Table 5.1, see crystallographic details in Supporting Information), which unequivocally confirm the capture of these cations. We are still working on solving the EA structure, which once solved, will be the first example of n = 2 EA-containing RP perovskite. We obtained previously reported MA[25], FA[26], GA[27] structures and conducted structural analysis on the series of $(PA)_2(A)Pb_2I_7$ perovskites. It is worth of noting that AA represents the largest A-cation (tolerance factor 1.05) that has been incorporated into the halide perovskite lattice. It is therefore a very interesting materials system to the systematic study on how the A-cations influence the crystal structures and thereby the optoelectronic and ferroelectric properties in halide perovskites in general.

Table 5.1 Crystal and Refinement Data for $(PA)_2(A)Pb_2I_7$ (A = DMA, AA)

	$(PA)_2(DMA)Pb_2I_7$	$(PA)_2(AA)Pb_2I_7$
crystal system	monoclinic	monoclinic
space group	$P2_1$	$C2/c$
***a*/Å; α/°**	8.605(2); 90	40.927(16); 90
***b*/Å; β/°**	9.124(2); 97.947(7)	9.205(3); 92.520(14)
***c*/Å; γ/°**	20.774(5); 90	8.587(3); 90
volume/ Å^3	1615.35	3232
Z	2	4
density (calc.) / g/cm^3	3.135	3.161
reflections collected	11083	23360
independt reflectinons	11083	3327
	[R_{int} = 0.0850, R_{sigma} = 0.0621]	[(R_{int} = 0.0607, R_{sigma} = 0.0397]
No. of data/restraints/params.	11083/153/226	3327/69/93
Goodness-of-fit on F^2	1.033	1.182
Final *R* indexes [I ≥ 2σ(I)]	R_1 = 0.0506, wR_2 = 0.1105	R_1 = 0.0891, wR_2 = 0.1844
Final *R* indexes [all data]	R_1 = 0.0670, wR_2 = 0.1177	R_1 = 0.0983, wR_2 = 0.1879
Largest diff. peak /hole / e Å^{-3}	5.34/-3.93	3.91/-5.63

Table 5.2 Structural analysis of $(PA)_2(A)Pb_2I_7$

	$(PA)_2(MA)Pb_2I_7$	$(PA)_2(FA)Pb_2I_7$	$(PA)_2(DMA)Pb_2I_7$	$(PA)_2(GA)Pb_2I_7$	$(PA)_2(AA)Pb_2I_7$
$R_{A,\ eff}$ (pm)	217	253	272	279	284
tolerance factor	0.91	0.99	1.03	1.04	1.05
V_{cage} (Å^3)	257.7	269.7	262.9	276.9	264.2
interlayer spacing (Å)	8.07	7.94	7.93	7.88	7.82
av. eq. Pb-I (Å)	3.179	3.202	3.210	3.218	3.189
av. Pb-I (Å)	3.176	3.201	3.211	3.217	3.198
axial Pb-I_{int} (Å)	3.254	3.336	3.391	3.396	3.412
	3.282	3.336	3.365	3.386	3.336
axial Pb-I_{ext}(Å)	3.073	3.060	3.049	3.038	3.059
axial Pb-I-Pb angle	163.99	170.68	167.11	171.95	162.45
av. eq. Pb-I-Pb angle	166.54	168.64	163.21	167.61	162.27
PA N-head penetration (Å)	2.133	2.072	2.118	1.952	1.739

Generally speaking, structures accommodating large A-cations are expected to exhibit elongated Pb-I bonds and an expanded perovskite cage.[16-18] The induced tensile strain can be offset by the compressive strain in flexible ligand layer, resulting in a shorter interlayer distance (Figure 5.2g), defined by planes crossing terminal iodine atoms as well as further penetration of the PA nitrogen-head into the inorganic lattice as the A-cation size increases (Figure 5.2d and Table 5.2). Surprisingly, the AA structure breaks the trend of lattice expansion within the $(PA)_2(A)Pb_2I_7$ series, containing shorter average Pb-I bonds and a smaller cage volume than FA (Figure 5.2f). The Pb-I bonds can be further categorized into equatorial and axial bonds, corresponding to the bonds perpendicular and parallel to the stacking direction, respectively (Figure 5.2e). The AA structure exhibits an extra-long external axial Pb-I bond but the shortest equatorial Pb-I bonds in the entire

series except for MA, which contains the smallest A-cation in the list (Figure 5.2f). Closer examination of the equatorial Pb-I bonds in AA reveals 2 long bonds (3.234 Å) and 2 abnormally short bonds (3.133 Å), the latter of which are responsible for unsually short average Pb-I bond length. Accompanying the shorter equatorial Pb-I bonds are highly bent axial Pb-I-Pb bonds with angles deviating the most from 180° in the series (Figure 5.2g). Observing decreased axial bond angles with a larger A-cation is counter-intuitive and is in contradiction to the trend observed in the $(BA)_2(A)Pb_2I_7$ series, in which the axial and equatorial Pb-I-Pb bonds straighten to accommodate the large A-cations.[17,29] As AA is the largest A-cation reported to date, we hypothesize that AA is too large to be included by simply expanding the cage isotropically; instead, the perovskite cage adapts to the shape and orientation of the AA cations and becomes highly distorted. The cage is stretched along the b axis in alignment with the AA cation to better accommodate the extra-large A-cation, resulting in a simultaneous compression along the c axis. This anisotropic stretching is partly supported by the unusual anisotropic in-plane lattice parameters in AA (Figure 5.2c). Isotropic in-plane lattice parameters that are roughly $\sqrt{2} \times 2 \times (Pb - I)$ are commonly observed in 2D RP perovskites.[15,30] The large anisotropic lattice parameters and $[PbI_6]^{4-}$ octahedra distortion are also observed in DMA (Figure 5.2a), which similarly exhibits a shrunken cage that is smaller than that of FA (Figure 5.2g), and highly bent axial Pb-I-Pb bonds.

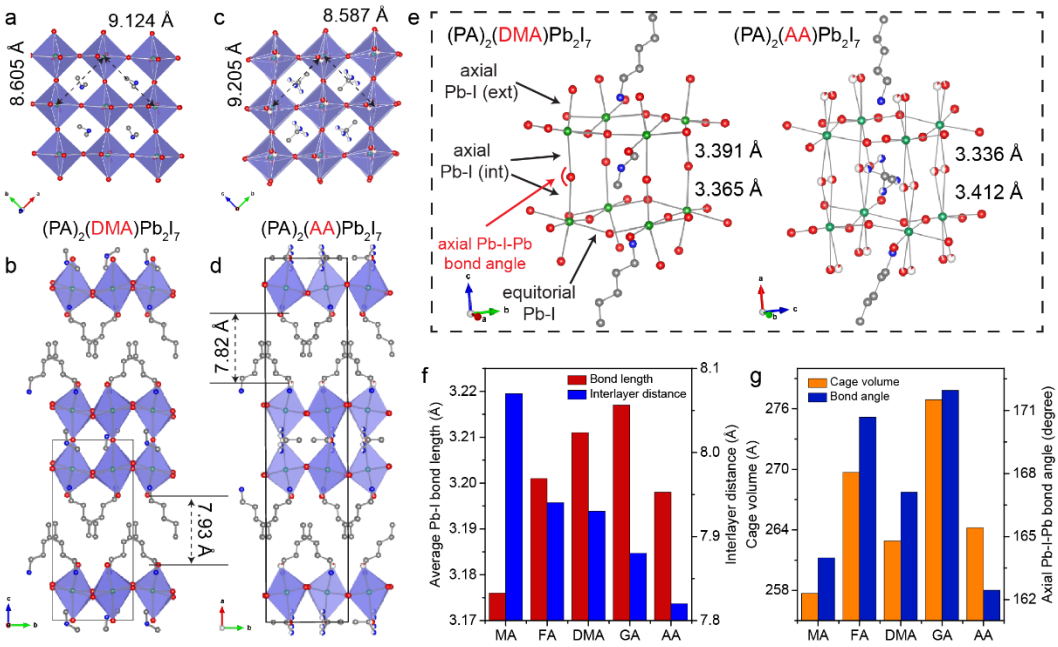

Figure 5.2 Crystal structures of $(PA)_2(DMA)Pb_2I_7$, $(PA)_2(AA)Pb_2I_7$ and structure analysis of series of $(PA)_2(A)Pb_2I_7$.

Top view (a, c) and side view (b,d) of the $(PA)_2(DMA)Pb_2I_7$ and $(PA)_2(AA)Pb_2I_7$ structures, respectively. The anisotropic lattice parameters and interlayer distances are marked by dashed arrows. (e) The perovskite cages of $(PA)_2(DMA)Pb_2I_7$, $(PA)_2(AA)Pb_2I_7$. Average Pb-I bond lengths, interlayer distances (f), cage volume and axial Pb-I-Pb bond angles (g) for series of $(PA)_2(A)Pb_2I_7$.

To further confirm our hypothesis that DMA and AA introduce anisotropic strain to the lattice and thus large distortion to the Pb-I framework, we examined the extent of distortion in each individual $(PA)_2(A)Pb_2I_7$ lead iodide octahedron, quantified by calculating the equatorial Pb-I bond length variance (Δd) and bond angle variances (σ_1^2) defined as below[31]:

$$\Delta d = (\frac{1}{4}) \sum [\frac{d_i - d}{d}]^2$$

$$\sigma_1^2 = \frac{1}{11} \sum_{i=1}^{12} (\alpha_i - 90)^2$$

where d_i is the equatorial Pb-I lengths, d is the average equatorial Pb-I lengths, and α_i is the neighboring I-Pb-I bond angle (Figure 5.3c). DMA and AA exhibit Δd and σ_1^2 vales that are orders of magnitudes larger than the rest of $(PA)_2(A)Pb_2I_7$ compounds, attesting to the highly asymmetric equatorial Pb-I bonds and tilted $[PbI_6]^{4-}$ octahedra in their structures. This high level of distortion is notably absent in GA, which has small Δd and σ_1^2 despite a large cation size (Figure 5.3a). This observation reveals that the size of the A-cation is not the sole determining factor, and the polarity and shape of the A-cation also affect how they interact and distort the inorganic lattice. Accordingly, while we are still trying to solve the EA structure, we predict it is likely to exhibit similarly large distortion because of the linear shape and polarity of the EA cation (Figure A4.2).

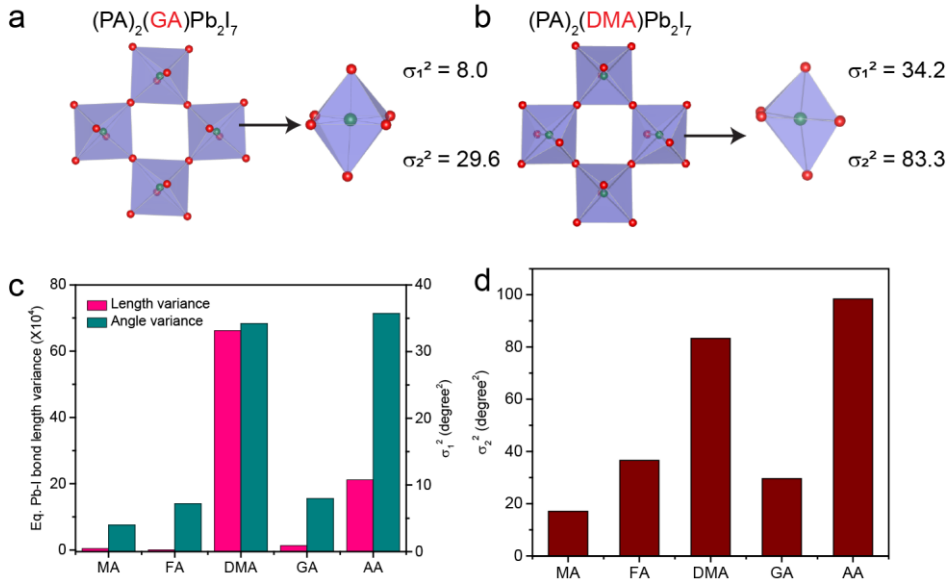

Figure 5.3 Structural distortion analysis

(a) The Pb-I framework in $(PA)_2(GA)Pb_2I_7$ viewed in the out-of-plane direction, and the distortion of individual $[PbI_6]^{4-}$ octahedron. (a) The Pb-I framework in $(PA)_2(DMA)Pb_2I_7$ viewed in the out-of-plane direction, and the distortion of individual $[PbI_6]^{4-}$ octahedron. (c) The equatorial Pb-I bond length variance and neighboring I-Pb-I bond angle variance. (d) The non-neighboring I-Pb-I bond variance.

One possible consequence of large octahedral distortion is the transition of crystal structure to a non-centrosymmetric space group[32], and the possible emergence of ferroelectricity, which arises from stereochemical expression of the $6s^2$ electron pair into lone pair in Pb^{2+} cation.[20] Specifically, when the tolerance factor *t* of a perovskite structure is greater than 1, the B-cations become off-centered in the octahedron due to the second-order Jahn-Teller effect[33], resulting polar structure, as exampled by $BaTiO_3$.[34] Halide perovskite ferroelectrics are very attractive because of the potential coupling of ferroelectricity with the excellent semiconducting properties.[35] Empirically, in halide perovskites, the tendency towards ferroelectric distortion increases as the A-cation size increases, due to the expansion of Pb-I bonds.[17,18,36] However, previous exploration of such effect was hindered by the limited choice of A-cations to Cs^+, MA^+, FA^+, which all have $t < 1$ and non-polar structures. Here we investigate the potential emergence of ferroelectricity in the series of $(PA)_2(A)Pb_2I_7$ perovskites with $t > 1$.

Table 5.3 Structural distortions of $(PA)_2(A)Pb_2I_7$

	$(PA)_2(MA)Pb_2I_7$	**$(PA)_2(FA)Pb_2I_7$**	**$(PA)_2(DMA)Pb_2I_7$**	**$(PA)_2(GA)Pb_2I_7$**	**$(PA)_2(AA)Pb_2I_7$**
$R_{A,\,eff}$ (pm)	217	253	272	279	284
tolerance factor	0.91	0.99	1.03	1.04	1.05
σ_1^2 (degree^2)	4.0	7.2	34.2	8.0	35.7
σ_2^2 (degree^2)	17.10	36.63	83.28	29.63	98.39
Δd (10^{-4})	0.47	0.04	66.2	1.35	21.2
space group	***Cc***	*Pnma*	***$P2_1$***	***Cc***	*C2/c*

The stereochemical expression of the $6s^2$ electron pair and subsequent Pb^{2+} off-centering can be quantified by calculating the bond angle variances (σ_2^2) between the non-neighboring I-Pb-I bonds (Table 5.3):[20]

$$\sigma_2^2 = \frac{1}{2}\sum_{i=1}^{3}(\beta_i - 180)^2$$

All compounds show none-zero σ_2^2, indicating the presence of Pb^{2+} off-centering. AA and DMA exhibit the largest σ_2^2, in agreement with the structural analyses. However, AA and FA both crystalize in centrosymmetric space groups, eliminating the possibility of ferroelectricity. Analysis of the crystal structures reveals an antipolar alignment between layers in these structures, resulting in the cancellation of the local dipoles.

Based on the crystallographic space group assignments, only MA, GA and DMA crystallize into polar space groups (Table 5.3). To confirm this assignment, we screened all compounds using second harmonic generation (SHG) (Figure 5.4), a technique that is commonly used to screen for non-centrosymmetric and ferroelectric materials.[37] In the case of both MA and GA, although the structures have positive σ_2^2 values and have been assigned the polar space group *Cc*, we did not observe detectable SHG, a discrepancy of which may be explain by the ambiguity when assigning proper space groups in halide perovskites.[37] DMA crystallizes in a polar space group of $P2_1$, and exhibits large σ_2^2 and collective Pb^{2+} off-centering as shown in the top view of its lattice (Figure 5.3b). However, we also did not observe detectable SHG from the DMA crystal. This could be due to the weak SHG activity as the polarization for the DMA structure calculated based on point-charge model[38] is quite small (1.2 $\mu C/cm^2$) (Table A4.2). The EA compound exhibited the strongest SHG response, from which we can predict the crystal structure will be non-centrosymmetric. Because of this non-centrosymmetry and the large, polar EA cation, we also predict that this phase maybe highly distorted with the potential for ferroelectricity. These results confirm that that size of the A-cation is not the sole determining factor for resultant lattice distortion and tolerance factor based on spherical estimations works less efficiently in halide

perovskites. The shape and dipole of the organic cations also play important role in the structural modulation

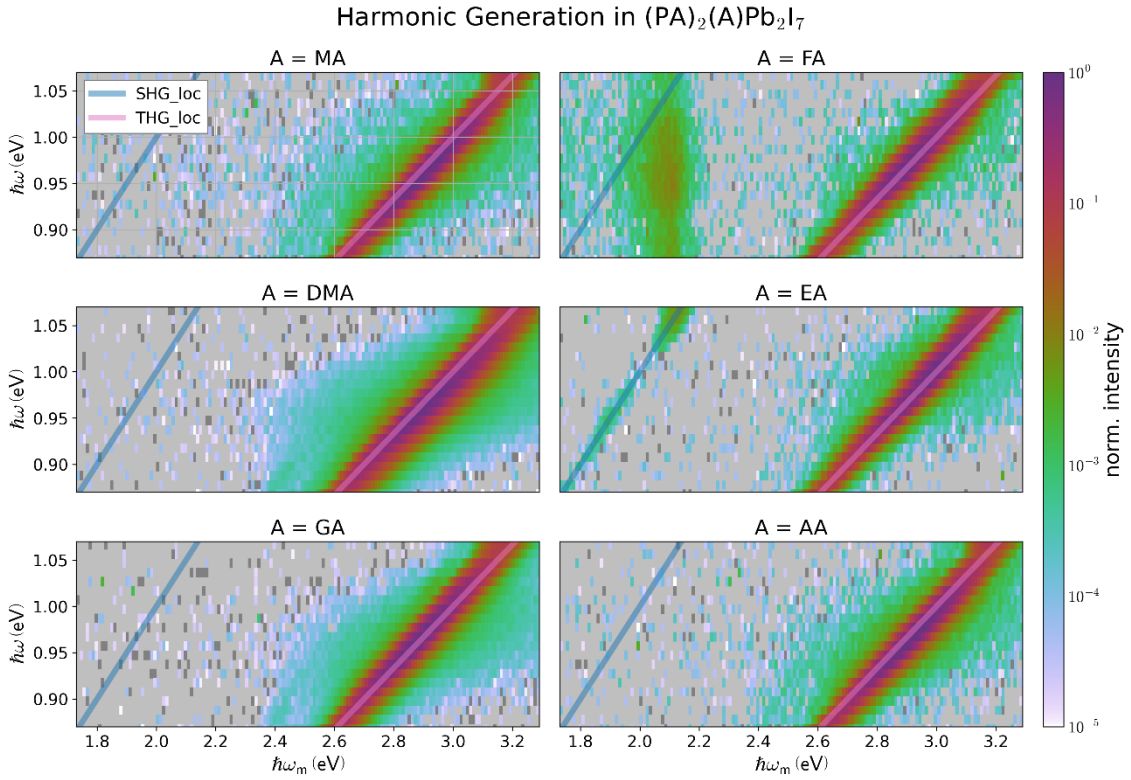

Figure 5.4 Multidimensional harmonic generation[2] for six $(PA)_2(A)Pb_2I_7$ 2D RP perovskite samples.

The x-axis is the monochromator set point (emission color), and the y-axis is the excitation laser set point; the colormap (in logarithmic scale, shown on the right-hand side) corresponds to measured output intensity. Blue overlines indicate the SHG emission frequency. The excitation laser has a smooth variation in its spectrum which is maximized at $\hbar\omega \approx 0.96$ eV with a fluence of ~1400 μJ/cm2; this variation is not corrected for in these spectra. Gray pixels indicate values that are negative and therefore unable to be represented on a logarithmic scale. These pixels characterize the noise floor of our measurement.

Optical properties. In order to study the structure-property relationship in these compounds, we conducted optical property characterizations. Room temperature absorption and PL spectra of the exfoliated sheets are shown in Figure 5.5a. All variants exhibit a single sharp excitonic peak around ~ 579 nm, corresponding to the $n = 2$ quantum wells. The optical absorption spectra exhibit a high-energy absorption edge and a lower-energy exciton peak. The bandgaps are estimated by extrapolation, which reveals the trend $E_{g,AA} > E_{g,DMA} > E_{g,GA} > E_{g,EA} > E_{g,FA} > E_{g,MA}$.

Previous studies showed that the Pb-I-Pb angle variation and Pb-I bond length stretching are determining factors for the bandgap energy in lead halide perovskites by changing the lead s- and halogen p-orbital overlaps.[39-41] This trend is consistent with our experimental data: DMA and AA show the largest bandgap across all phases, in coincidence with fact that they exhibit the most distorted structures (Table 5.4). Overall, the bandgap increases as the average Pb-I bond length increases and average Pb-I-Pb bond angle further deviates from 180° (Figure 5.5b). We modeled such dependence with DFT calculation using a simplified structure "$Cs_3Pb_2I_7$" (Figure 5.5c)[17], and the calculated trend matches the experimentally determined values well. Besides changes in bandgap energies, the PL intensity is apparently quenched in the structures with larger A-cation size (Table 5.4). Given the similar quantum and dielectric confinement of the structures, the decreased PL intensity and increased PL asymmetry in compounds with large A-cations can be attributed to a higher nonradiative decay rate caused by more exciton-phonon interactions[16,17], which is supported by the shorter PL lifetime and larger PL FWHM (Table 5.4).

Table 5.4 Comparison of optical properties and structural parameters

	$(PA)_2(MA)Pb_2I_7$	**$(PA)_2(FA)Pb_2I_7$**	**$(PA)_2(DMA)Pb_2I_7$**	**$(PA)_2(EA)Pb_2I_7$**	**$(PA)_2(GA)Pb_2I_7$**	**$(PA)_2(AA)Pb_2I_7$**
PL emission (eV)	2.152	2.162	2.206	2.176	2.199	2.208
Relative PL intensity	1	0.76	0.05	0.02	0.08	0.08
PL FWHM (nm)	22	21	27	31	26	28

Ave. Pb-I length (A)	3.176	3.201	3.192	*N/A*	3.216	3.198
Ave. Pb-I-Pb angle	166.5	168.6	163.2	*N/A*	167.6	162.2

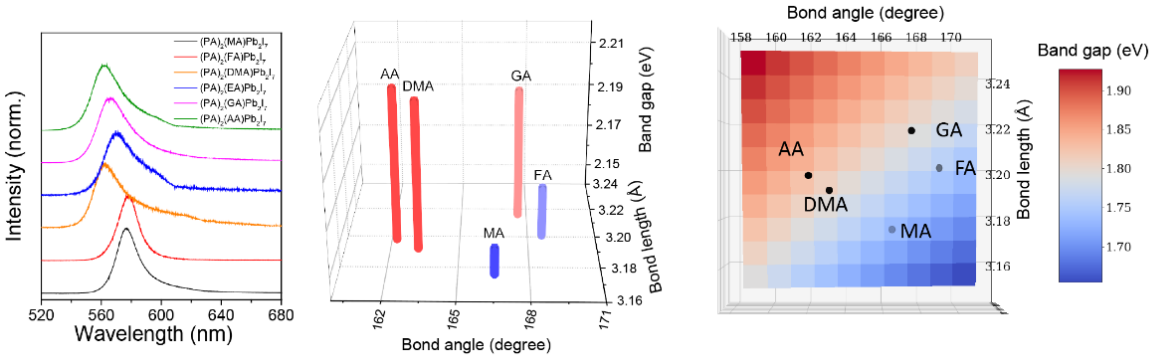

Figure 5.5 Optical characterization

(a) PL spectra of the compounds. (b) 3D maps of the extract bandgaps plotted against the average Pb-I bond length and average equatorial Pb-I-Pb bond angles. (c) 2D color maps of the computed electronic bandgap energies (Eg) for different average Pb-I bond length and average equatorial Pb-I-Pb bond angles, overlaid by the calculated bandgaps based on experimental crystal structures.

5.4 Conclusion

Our study suggests that large A-cations in 2D perovskite cause significant structural distortion to the inorganic lattice, including expansion of the perovskite cage and large octahedra tilting, and Pb^{2+} off-centering. Significantly, we found such modulation effect depends not only on the size of the A-cations, but also their shape and polarity. This is manifested by the short average Pb-I bond lengths and small cage volumes in AA despite the largest A-cation, and the most distorted and anisotropic inorganic lattices in both AA and DMA. These structural changes influence the optical properties: specifically, the bandgap increases as the Pb-I bond length increases and the average Pb-I-Pb bond angle deviates from 180°. The PL intensity also lowers and the PL lifetime shortens in these highly distorted structures, likely due to more exciton-phonon interactions. Finally, Pb off-centering is observed in all 6 $(PA)_2(A)Pb_2I_7$ examined here, but the potential emergence of

ferroelectricity further depends on how the induced dipoles are aligned in each structure and the overall symmetry of the crystal. Our work improves the understanding of the structure−property relationship of 2D perovskites and could help future design of more optimal materials for specific optoelectronic applications as well as open up new opportunities to tune the crystal structure and symmetry of halide perovskites as functional materials for non-linear optical, ferroelectric, and spintronics applications.

5.5 References

1 Kojima, A., Teshima, K., Shirai, Y. & Miyasaka, T. Organometal Halide Perovskites as Visible-Light Sensitizers for Photovoltaic Cells. *Journal of the American Chemical Society* **131**, 6050-+, doi:10.1021/ja809598r (2009).

2 Fu, Y. *et al.* Metal halide perovskite nanostructures for optoelectronic applications and the study of physical properties. *Nature Reviews Materials* **4**, 169-188, doi:10.1038/s41578-019-0080-9 (2019).

3 Zhu, H. *et al.* Organic Cations Might Not Be Essential to the Remarkable Properties of Band Edge Carriers in Lead Halide Perovskites. *Adv Mater* **29**, 1603072, doi:https://doi.org/10.1002/adma.201603072 (2017).

4 Fu, Y. *et al.* Broad Wavelength Tunable Robust Lasing from Single-Crystal Nanowires of Cesium Lead Halide Perovskites (CsPbX3, X = Cl, Br, I). *ACS Nano* **10**, 7963-7972, doi:10.1021/acsnano.6b03916 (2016).

5 Zhu, H. *et al.* Screening in crystalline liquids protects energetic carriers in hybrid perovskites. *Science* **353**, 1409-1413, doi:doi:10.1126/science.aaf9570 (2016).

6 Miyata, K., Atallah, T. L. & Zhu, X.-Y. Lead halide perovskites: Crystal-liquid duality, phonon glass electron crystals, and large polaron formation. *Sci Adv* **3**, e1701469, doi:doi:10.1126/sciadv.1701469 (2017).

7 Frost, J. M. & Walsh, A. What Is Moving in Hybrid Halide Perovskite Solar Cells? *Accounts Chem Res* **49**, 528-535, doi:10.1021/acs.accounts.5b00431 (2016).

8 Pellet, N. *et al.* Mixed-Organic-Cation Perovskite Photovoltaics for Enhanced Solar-Light Harvesting. *Angewandte Chemie International Edition* **53**, 3151-3157, doi:https://doi.org/10.1002/anie.201309361 (2014).

9 Turren-Cruz, S.-H., Hagfeldt, A. & Saliba, M. Methylammonium-free, high-performance, and stable perovskite solar cells on a planar architecture. *Science* **362**, 449-453, doi:doi:10.1126/science.aat3583 (2018).

10 Lee, J.-W. *et al.* Formamidinium and Cesium Hybridization for Photo- and Moisture-Stable Perovskite

Solar Cell. *Adv Energy Mater* **5**, 1501310, doi:https://doi.org/10.1002/aenm.201501310 (2015).

11 Saliba, M. *et al.* Cesium-containing triple cation perovskite solar cells: improved stability, reproducibility and high efficiency. *Energ Environ Sci* **9**, 1989-1997, doi:10.1039/C5EE03874J (2016).

12 Kieslich, G., Sun, S. J. & Cheetham, A. K. Solid-state principles applied to organic-inorganic perovskites: new tricks for an old dog. *Chem Sci* **5**, 4712-4715, doi:10.1039/c4sc02211d (2014).

13 Travis, W., Glover, E. N. K., Bronstein, H., Scanlon, D. O. & Palgrave, R. G. On the application of the tolerance factor to inorganic and hybrid halide perovskites: a revised system. *Chem Sci* **7**, 4548-4556, doi:10.1039/c5sc04845a (2016).

14 Fu, Y. *et al.* Stabilization of the Metastable Lead Iodide Perovskite Phase via Surface Functionalization. *Nano Lett* **17**, 4405-4414, doi:10.1021/acs.nanolett.7b01500 (2017).

15 Stoumpos, C. C. *et al.* Ruddlesden-Popper Hybrid Lead Iodide Perovskite 2D Homologous Semiconductors. *Chem Mater* **28**, 2852-2867, doi:10.1021/acs.chemmater.6b00847 (2016).

16 Fu, Y. P. *et al.* Incorporating Large A Cations into Lead Iodide Perovskite Cages: Relaxed Goldschmidt Tolerance Factor and Impact on Exciton-Phonon Interaction. *Acs Central Sci* **5**, 1377-1386, doi:10.1021/acscentsci.9b00367 (2019).

17 Li, X. T. *et al.* Negative Pressure Engineering with Large Cage Cations in 2D Halide Perovskites Causes Lattice Softening. *Journal of the American Chemical Society* **142**, 11486-11496, doi:10.1021/jacs.0c03860 (2020).

18 Fu, Y. P. *et al.* Cation Engineering in Two-Dimensional Ruddlesden-Popper Lead Iodide Perovskites with Mixed Large A-Site Cations in the Cages. *Journal of the American Chemical Society* **142**, 4008-4021, doi:10.1021/jacs.9b13587 (2020).

19 Han, S. G. *et al.* High-Temperature Antiferroelectric of Lead Iodide Hybrid Perovskites. *Journal of the American Chemical Society* **141**, 12470-12474, doi:10.1021/jacs.9b05124 (2019).

20 Fu, Y., Jin, S. & Zhu, X. Y. Stereochemical expression of ns2 electron pairs in metal halide perovskites. *Nature Reviews Chemistry* **5**, 838-852, doi:10.1038/s41570-021-00335-9 (2021).

21 Frost, J. M. *et al.* Atomistic Origins of High-Performance in Hybrid Halide Perovskite Solar Cells. *Nano Lett* **14**, 2584-2590, doi:10.1021/nl500390f (2014).

22 Zhu, X. Y. & Podzorov, V. Charge Carriers in Hybrid Organic–Inorganic Lead Halide Perovskites Might Be Protected as Large Polarons. *The Journal of Physical Chemistry Letters* **6**, 4758-4761, doi:10.1021/acs.jpclett.5b02462 (2015).

23 Miyata, K. & Zhu, X. Y. Ferroelectric large polarons. *Nat Mater* **17**, 379-381, doi:10.1038/s41563-018-0068-7 (2018).

24 Stranks, S. D. & Plochocka, P. The influence of the Rashba effect. *Nat Mater* **17**, 381-382, doi:10.1038/s41563-018-0067-8 (2018).

25 Spanopoulos, I. *et al.* Uniaxial Expansion of the 2D Ruddlesden-Popper Perovskite Family for Improved Environmental Stability. *Journal of the American Chemical Society* **141**, 5518-5534,

doi:10.1021/jacs.9b01327 (2019).

26 Han, S. *et al.* Highly Oriented Thin Films of 2D Ruddlesden-Popper Hybrid Perovskite toward Superfast Response Photodetectors. *Small* **15**, e1901194, doi:10.1002/smll.201901194 (2019).

27 Xu, Z. *et al.* Highly Sensitive and Ultrafast Responding Array Photodetector Based on a Newly Tailored 2D Lead Iodide Perovskite Crystal. *Adv Opt Mater* **7**, 1900308, doi:10.1002/adom.201900308 (2019).

28 Li, L. N. *et al.* Tailored Engineering of an Unusual (C4H9NH3)(2)(CH3NH3)(2)Pb3Br10 Two-Dimensional Multilayered Perovskite Ferroelectric for a High-Performance Photodetector. *Angew Chem Int Edit* **56**, 12150-12154, doi:10.1002/anie.201705836 (2017).

29 Li, X. *et al.* Expanding the Cage of 2D Bromide Perovskites by Large A-Site Cations. *Chem Mater*, doi:10.1021/acs.chemmater.1c03605 (2022).

30 Li, X. T. *et al.* Two-Dimensional Dion-Jacobson Hybrid Lead Iodide Perovskites with Aromatic Diammonium Cations. *Journal of the American Chemical Society* **141**, 12880-12890, doi:10.1021/jacs.9b06398 (2019).

31 Robinson, K., Gibbs, G. V. & Ribbe, P. H. Quadratic Elongation: A Quantitative Measure of Distortion in Coordination Polyhedra. *Science* **172**, 567-570, doi:doi:10.1126/science.172.3983.567 (1971).

32 Fu, Y. Stabilization of Metastable Halide Perovskite Lattices in the 2D Limit. *Adv Mater*, e2108556, doi:10.1002/adma.202108556 (2022).

33 Walsh, A., Payne, D. J., Egdell, R. G. & Watson, G. W. Stereochemistry of post-transition metal oxides: revision of the classical lone pair model. *Chem Soc Rev* **40**, 4455-4463, doi:10.1039/c1cs15098g (2011).

34 Benedek, N. A. & Fennie, C. J. Why Are There So Few Perovskite Ferroelectrics? *The Journal of Physical Chemistry C* **117**, 13339-13349, doi:10.1021/jp402046t (2013).

35 Rappe, A. M., Grinberg, I. & Spanier, J. E. Getting a charge out of hybrid perovskites. *Proc Natl Acad Sci U S A* **114**, 7191-7193, doi:10.1073/pnas.1708154114 (2017).

36 Gao, L. L. *et al.* Incorporated Guanidinium Expands the CH3NH3PbI3 Lattice and Enhances Photovoltaic Performance. *Acs Appl Mater Inter* **12**, 43885-43891, doi:10.1021/acsami.0c14925 (2020).

37 Morrow, D. J. *et al.* Disentangling Second Harmonic Generation from Multiphoton Photoluminescence in Halide Perovskites using Multidimensional Harmonic Generation. *J Phys Chem Lett* **11**, 6551-6559, doi:10.1021/acs.jpclett.0c01720 (2020).

38 Li, L. N. *et al.* Bilayered Hybrid Perovskite Ferroelectric with Giant Two-Photon Absorption. *Journal of the American Chemical Society* **140**, 6806-6809, doi:10.1021/jacs.8b04014 (2018).

39 Mao, L. L. *et al.* Tunable White-Light Emission in Single-Cation-Templated Three-Layered 2D Perovskites (CH3CH2NH3)(4)Pb3Br10-xClx. *Journal of the American Chemical Society* **139**, 11956-11963, doi:10.1021/jacs.7b06143 (2017).

40 Knutson, J. L., Martin, J. D. & Mitzi, D. B. Tuning the Band Gap in Hybrid Tin Iodide Perovskite Semiconductors Using Structural Templating. *Inorg Chem* **44**, 4699-4705, doi:10.1021/ic050244q (2005).

41 Pedesseau, L. *et al.* Advances and Promises of Layered Halide Hybrid Perovskite Semiconductors. *ACS Nano* **10**, 9776-9786, doi:10.1021/acsnano.6b05944 (2016).

Appendix 1. Supporting Information for Chapter 2

Description of models used to extract diffusion coefficients:

We measured the spatially resolved PL spectra of the $CsPbBr_{3-3x}Cl_{3x}$ NW after diffusion and converted the PL information to the halide compositions by assuming a linear Vegard's law. Because of the unique 1D geometry of the NWs, the composition profile along the NW developed after anion interdiffusion can be well described by the Fick's second law[4]:

$$\frac{\partial c(x,t)}{\partial t} = D\frac{\partial^2 c(x,t)}{\partial x^2}$$

where *D* is the interdiffusion coefficient of the diffusion couple, which was assumed to be independent of concentration, and $c(x,t)$ is the percent concentration of Cl^- at time, *t*, and position, *x*, where *x* is the distance from the effective center of the diffusion and *t* is the time since the start of heating. To solve the above partial differential equation, we assumed that within the reaction zone, the anion exchange reaction is fast and in equilibrium. Then there are two sets of possible boundary conditions:

First, if the halide-source microplate of $CsPbCl_3$ is large and thick enough, which is mostly the case, the concentration of Cl^- at $x = 0$ would stay constant, i.e.

$$c = 0 \quad at \quad t = 0$$

$$c = c_0 \quad at \quad x = 0$$

$$\lim_{x\to+\infty} c = \lim_{x\to-\infty} c = 0$$

Where c_0 is the equilibrium concentration of Cl^- at the center of the diffusion. Imposing the conditions above leads to a solution to diffusion equation:

$$c(x,t) = c_0[1 - \mathrm{erf}\left(\frac{x}{\sqrt{4Dt}}\right)]$$

Alternatively, if the halide-source microplate of $CsPbCl_3$ is not sufficiently large to maintain Cl^- concentration at the center of diffusion, we would expect:

$$c(x = 0) = c_0\delta(x) \ \ at\ t = 0$$

$$\lim_{x\to+\infty} c = \lim_{x\to-\infty} c = 0$$

Then the solution to these conditions is:

$$c(x,t) = At^{-1/2}\exp\left(-\frac{x^2}{4Dt}\right)$$

Fitting the composition profiles by the above expressions, whichever fits the best, readily yields the interdiffusion coefficients (D), which are then used in the Arrhenius plot to extract the activation energy for the diffusion process. The fitting results can be found in Table S1 below.

Table A1.1 Diffusion coefficients measured at different temperatures

Temperature (K)	**D** (10^{-12} cm^2s^{-1})	**D** (10^{-12} cm^2s^{-1})	**D** (10^{-12} cm^2s^{-1})	**D** (10^{-12} cm^2s^{-1})	**D** (10^{-12} cm^2s^{-1})	**Aver. D** (10^{-12} cm^2s^{-1})	**σ** (10^{-12} cm^2s^{-1})
273	0.419	0.185	0.085	0.274	0.092	0.21	0.12
338	1.48	2.14	1.28	1.11	3.11	1.82	0.7
373	4.3	9.3	5.6	6.6	3.6	5.9	2.0
423	1.12×10^1	3.90×10^1	4.70×10^1	2.70×10^1	2.50×10^1	29.8	12.3
473	1.4×10^2	1.04×10^2	1.5×10^2	1.02×10^2	1.85×10^2	136	31

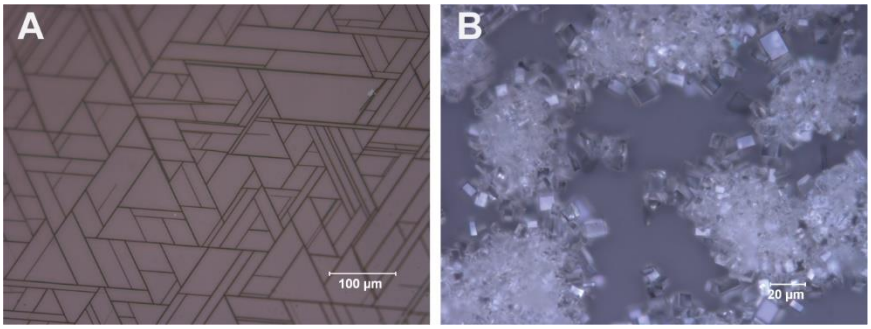

Figure A1.1. Optical images of the as synthesized nanostructures

(A) aligned $CsPbBr_3$ NWs on F-mica substrates, and (B) free-standing $CsPbCl_3$ microplates

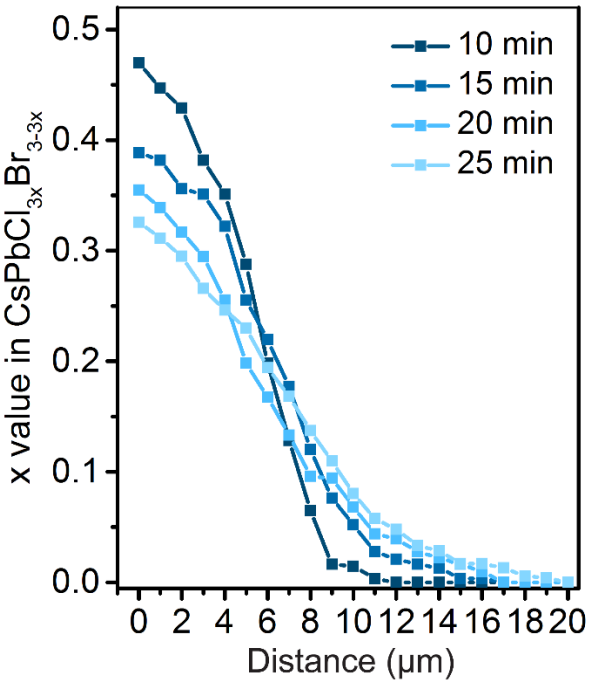

Figure A1.2. Time evolution of the composition profiles of the $CsPbBr_{3-3x}Cl_{3x}$ NWs.

The compositions were obtained from the PL peak positions by assuming a linear Vegard's law. The diffusion proceeded at 200 ℃.

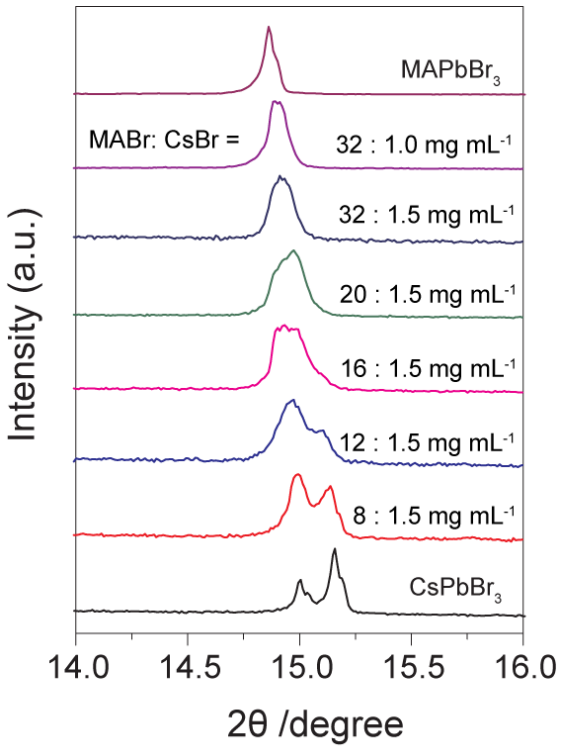

Figure A3. PXRD patterns of a series of direct solution-grown $(MA_xCs_{1-x})PbBr_3$ alloys.

Appendix 2. Supporting information for Chapter 3

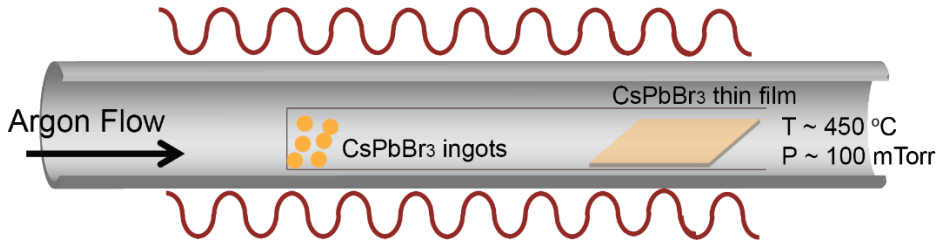

Figure A2.1 The tube-in-tube setup for the vapor phase epitaxial growth of CsPbBr3 single-crystal thin film on GGG (100) substrate.

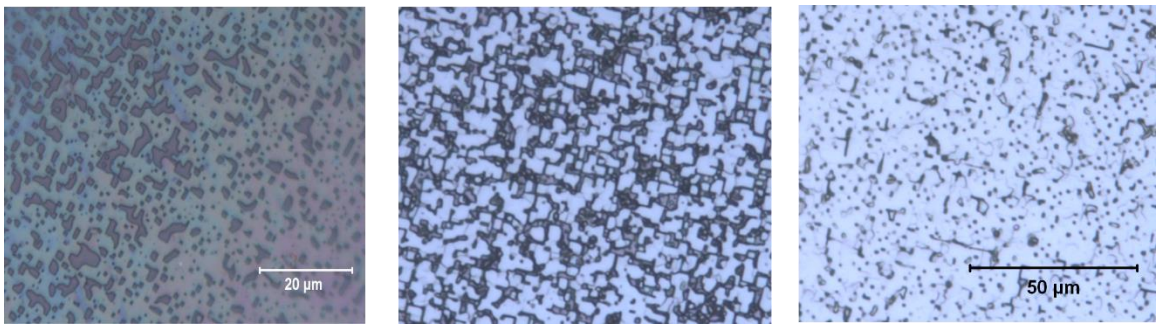

Figure A2.2. Lower growth temperature or shorter growth time reveal Volmer-Weber type of domain merging.

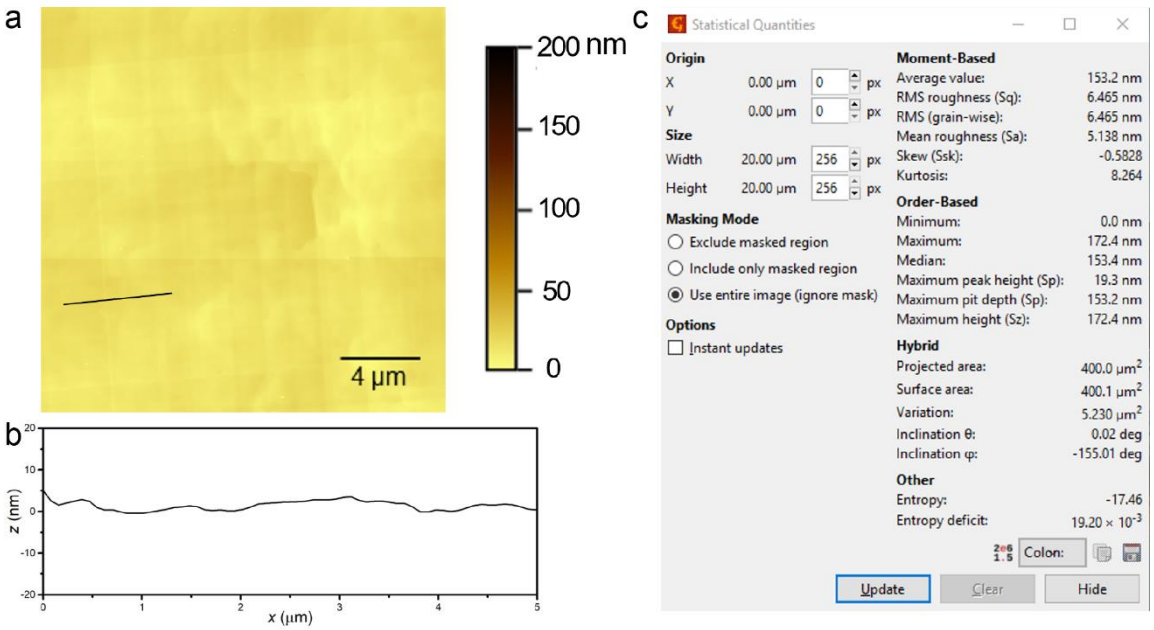

Figure A2.3. Ultra-smooth surface of the as-grown $CsPbBr_3$ SCTF.

(a) AFM characterization on the as-grown $CsPbBr_3$ SCTF. (b) Line-profile taken along the black line marked in (a). (c) Analysis on a 20 um x 20um area on the surface shows a mean roughness~ 5 nm using Gwyddion.

Appendix 3. Surpporting Information for Chapter 4

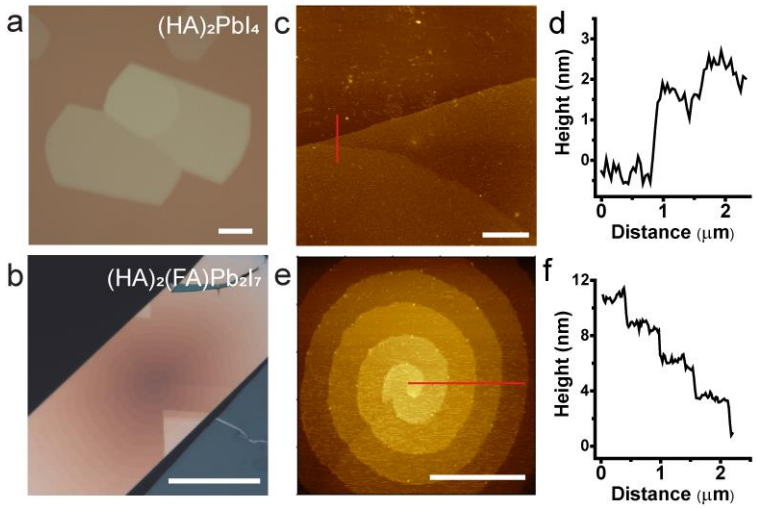

Figure A3.1 Optical and AFM images showing 2 different growth modes.

a, Optical image of $(HA)_2PbI_4$ sheets showing layer-by-layer growth. The AFM image (**c**) shows the growing layer to be ~1 nm thick in the AFM height profile scan (**d**) along the red line, corresponding to a monolayer of $(HA)_2PbI_4$. **b**, Optical image of a thicker $(HA)_2(FA)Pb_2I_7$ sheet showing dislocation-driven growth. AFM image (**e**) clearly shows the spiral steps with ~2 nm terrace height (**f**) corresponding to a monolayer of $(HA)_2(FA)Pb_2I_7$. Scale bars for optical images and AFM images are 50 μm and 2 μm, respectively.

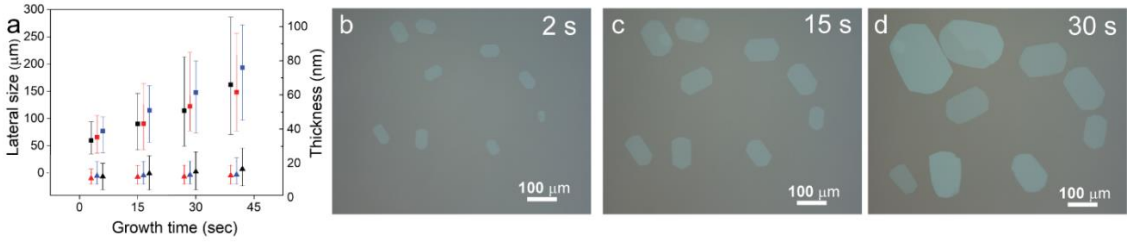

Figure A3.2 Reproducibility of the 2D RP perovskite nanosheet growth.

a, Evolution of the lateral size (top row, squares) and thickness (bottom row, triangles) of $(HA)_2PbI_4$ sheets as a function of growth time for three different growths (black, red, and blue,

respectively) under optimized growth conditions. **b-d**, Optical images of typical growth products taken at 2 s, 15 s, 30 s, respectively. The data points for different trials are offset slightly in time for better display

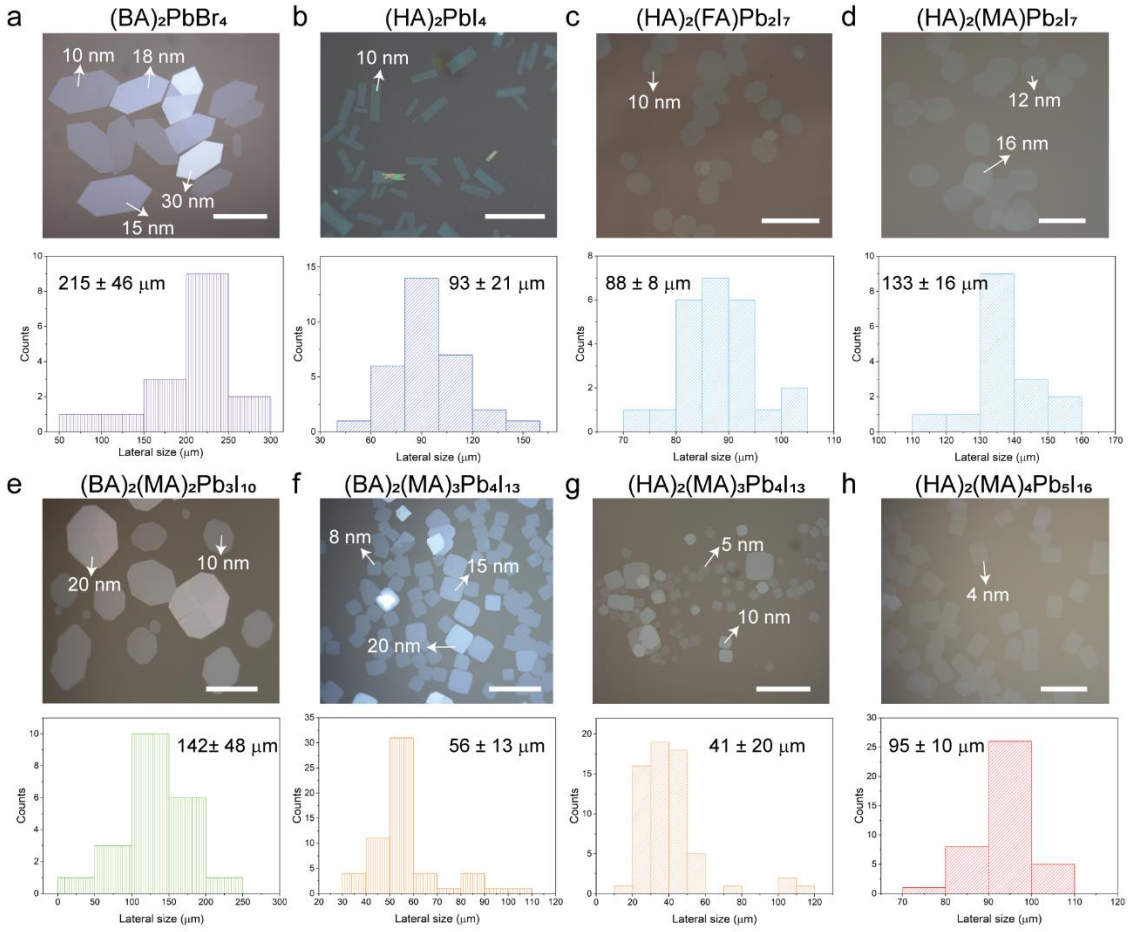

Figure A3.3 Floating growth of selected phases of 2D RP perovskite nanosheets under optimal conditions.

Optical images (upper row) and lateral size distributions (lower row) of a, $(BA)_2PbBr_4$, b, $(HA)_2PbI_4$, c, $(HA)_2(FA)Pb_2I_7$, d, $(HA)_2(MA)Pb_2I_7$, e, $(BA)_2(MA)_2Pb_3I_{10}$, f, $(BA)_2(MA)_3Pb_4I_{13}$, g, $(HA)_2(MA)_3Pb_4I_{13}$, h, $(HA)_2(MA)_4Pb_5I_{16}$ sheets, respectively, under optimized conditions after a growth time of 20 s. Scale bar: 200 μm. The typical thicknesses are marked next to the

sheets estimated by optical contrast (see more discussion below). The analysis was done at local regions, due to asynchronous crystallization and different surface tension across the growth droplet.

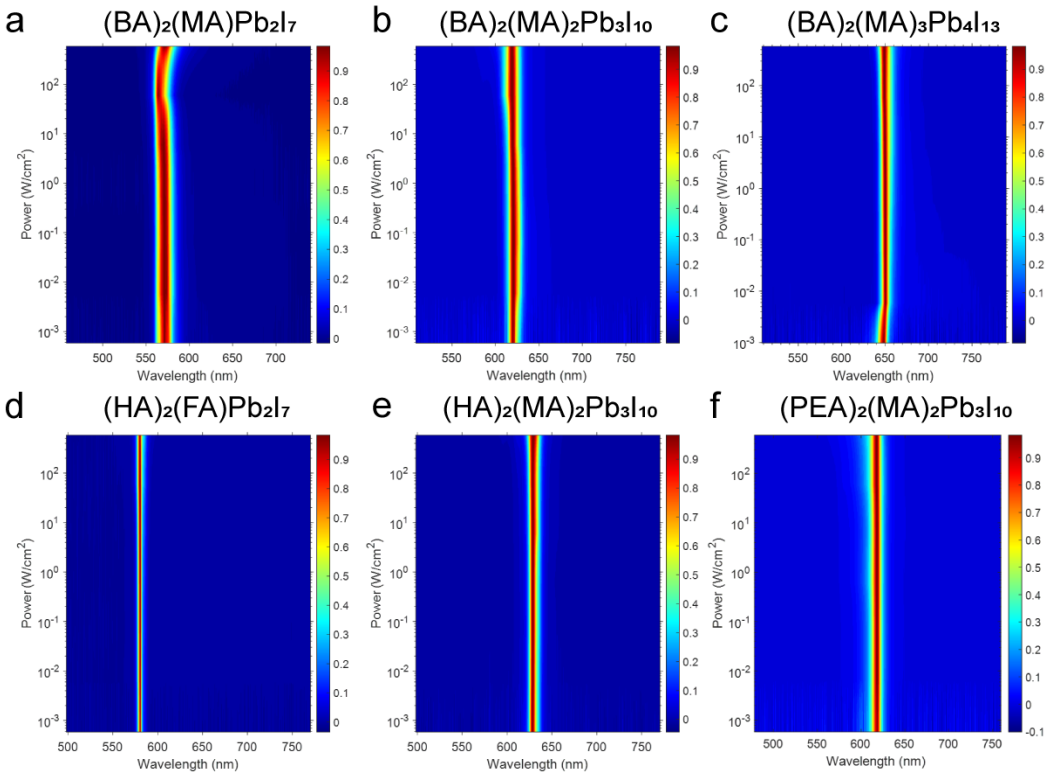

Fig. A3.4 Low-temperature (at 77 K) power-dependent PL studies of representative phases of 2D RP perovskites.

Each horizontal slice is normalized to its maximum value.

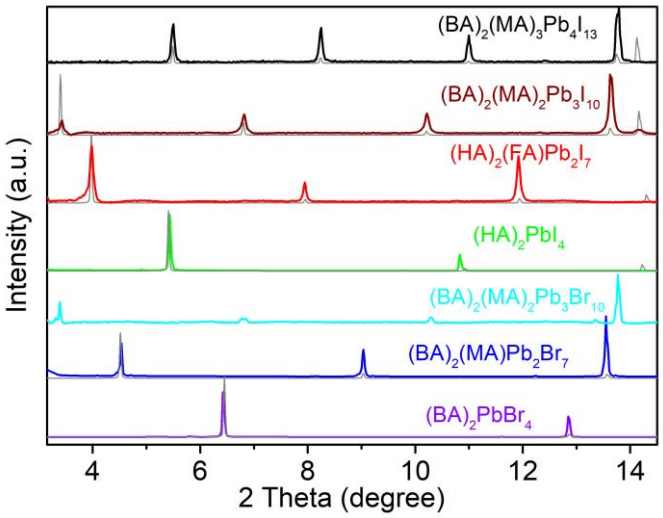

Figure A3.5 Powder X-ray diffraction (PXRD) characterization of various phases of 2D RP perovskite nanosheets.

The available standard XRD patterns are shown in gray dotted lines.

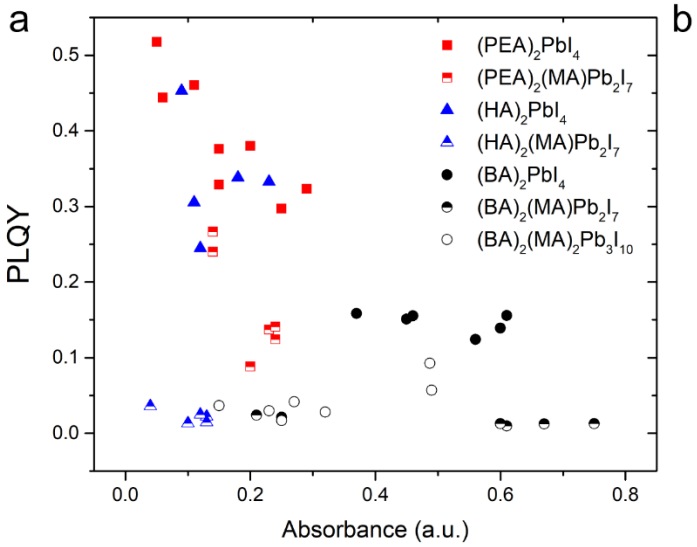

b

	PLQY (%)
$(PEA)_2PbI_4$	36 ± 9
$(PEA)_2(MA)Pb_2I_7$	17 ± 6
$(HA)_2PbI_4$	33 ± 7
$(HA)_2(MA)Pb_2I_7$	2.2 ± 0.8
$(BA)_2PbI_4$	14 ± 3
$(BA)_2(MA)Pb_2I_7$	1.7 ± 0.6
$(BA)_2(MA)_2Pb_3I_{10}$	3.9 ± 2.1

Figure A3.6 PLQY values estimated for nanosheets of 7 representative RP perovskite phases.

a, PLQY plotted versus the absorbance determined for each nanosheet. Each datapoint was collected on a different nanosheet and the PLQY is uniform across the same nanosheets. **b**, Average PLQY values and standard deviations for each phase.

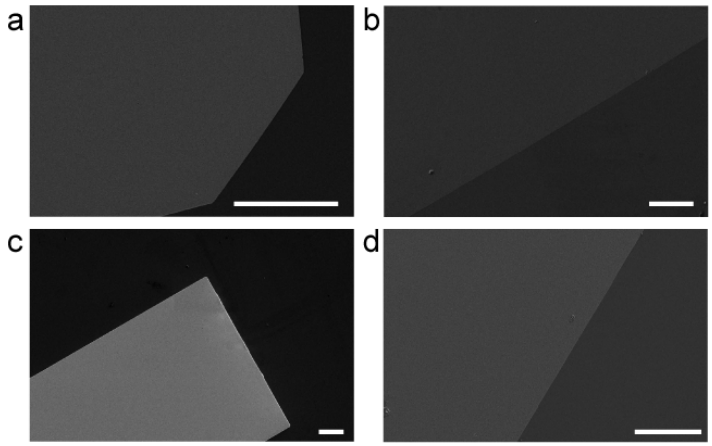

Figure A3.7 SEM images of the as-transferred thin sheets showing the uniform and smooth surface.

a, $(BA)_2(MA)_2Pb_3I_{10}$. **b**, $(HA)_2PbI_4$. c, $(HA)_2(FA)Pb_2I_7$. **d**, $(BA)_2PbBr_4$. Scale bar: 10 μm.

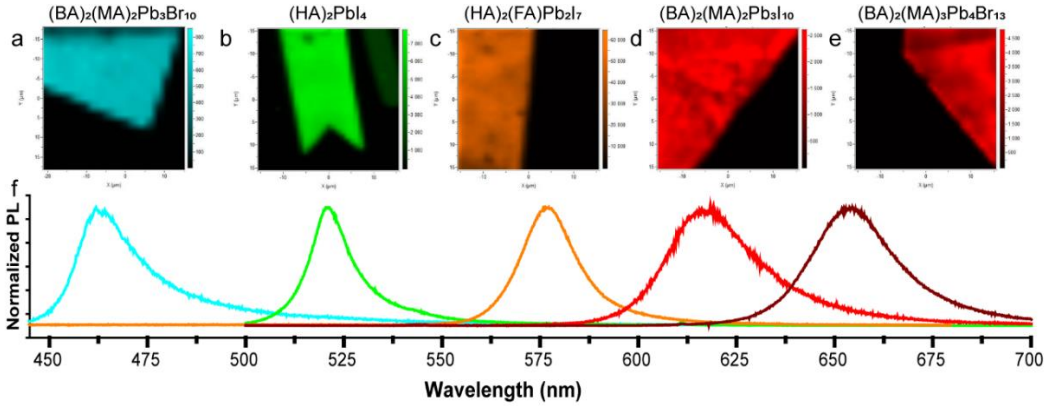

Figure A3.8 PL mapping on transferred thin sheets further showing the uniformness.

a, $(BA)_2(MA)_2Pb_3Br_{10}$. **b**, $(HA)_2PbI_4$. **c**, $(HA)_2(FA)Pb_2I_7$. **d**, $(BA)_2(MA)_2Pb_3I_{10}$. **e**, $(BA)_2(MA)_3Pb_4I_{13}$. **f**, Corresponding PL spectra. The size of the images in (**a**)-(**e**) is 21 μm × 21 μm. Colored bars in (**a**)-(**e**) indicate integrated PL intensity.

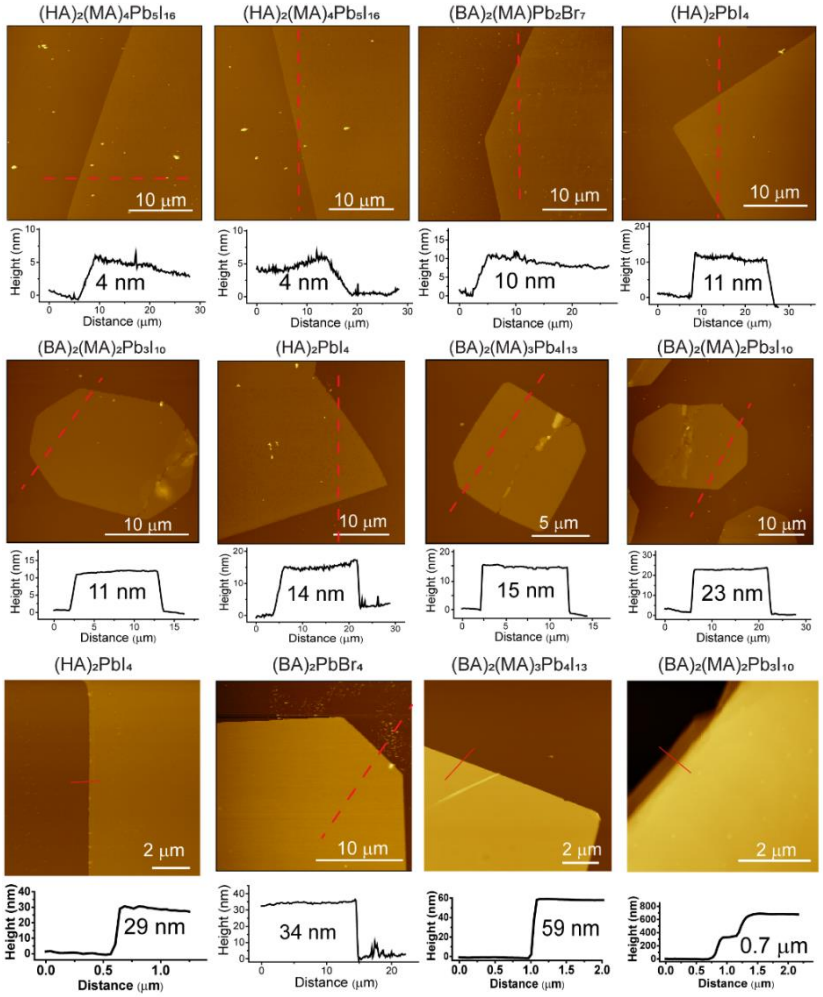

Figure A3.9 Additional AFM images of as-transferred 2D RP perovskite sheets with different thicknesses.

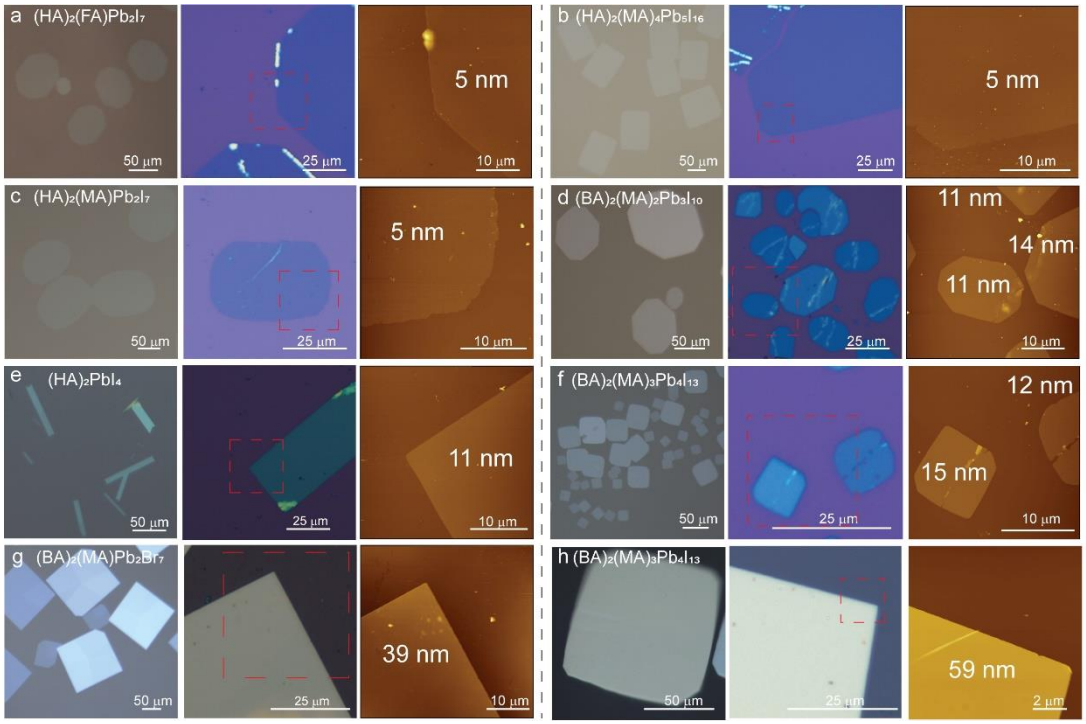

Figure A3.10 Optical-AFM correlations of 2D RP perovskite nanosheets.

Optical images of various phases of 2D RP perovskites with different thickness on the surface of droplets (left), on Si substrates (middle) and the corresponding AFM images (right), respectively. The correlation between the optical contrast and the thickness of these nanosheets allows the facile estimation of their thickness based on optical images.

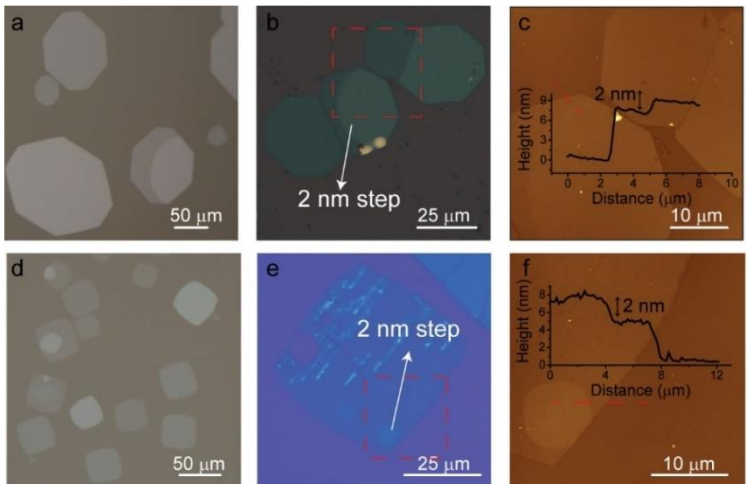

Figure A3.11 Resolving thickness addition by optical contrast.

Optical images of layer-by-layer grown and transferred sheets of $(BA)_2(MA)_2Pb_3I_{10}$ **(a,b)**, $(HA)_2(MA)_2Pb_3I_{10}$ **(d,e)**, respectively. AFM images (**c,f**) taken on the regions marked by the red-dashed boxes demonstrate that an increase of thickness as small as 2 nm (single-layer addition) can be resolved optically.

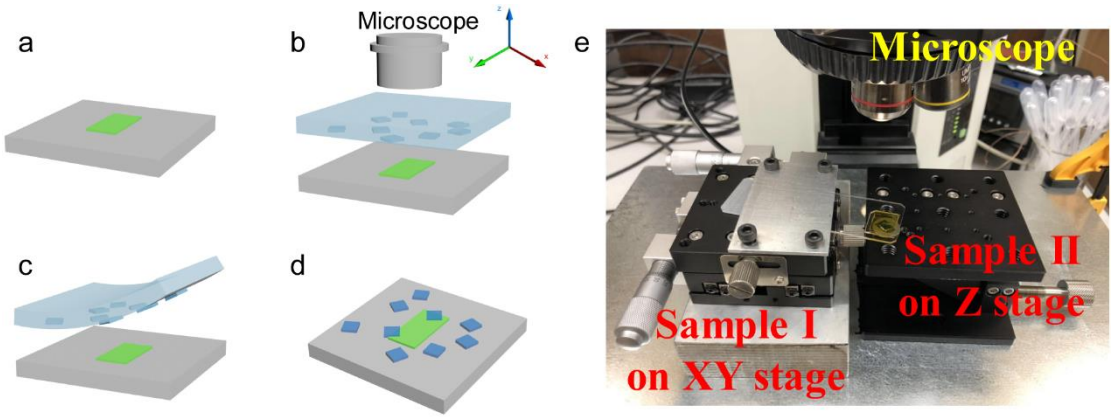

Figure A3.12 Illustration of the RP perovskite heterostructure fabrication process.

a, Transferred thin sheet of RP perovskite phase 1 on a substrate. **b**, Align the picked-up thin sheets of RP perovskite phase 2 (light blue) on PDMS stamp over a chosen phase 1 flake (green) under the optical microscope. **c**, Laminate phase 2 thin sheet onto the phase 1 sheet. **d**, Heterostructures of RP perovskites remain on the substrate after retracting the PDMS stamp. **e**, A photograph of the home-built transfer system under an optical microscope.

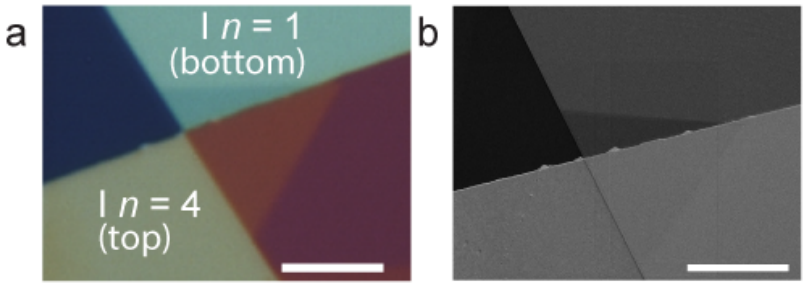

Figure A3.13 Further structural characterization of the heterostructure.

Optical image (**a**) and SEM image (**b**) further showing the conformal contact in the heterostructures of 2D RP perovskites. Scale bar: 10 μm.

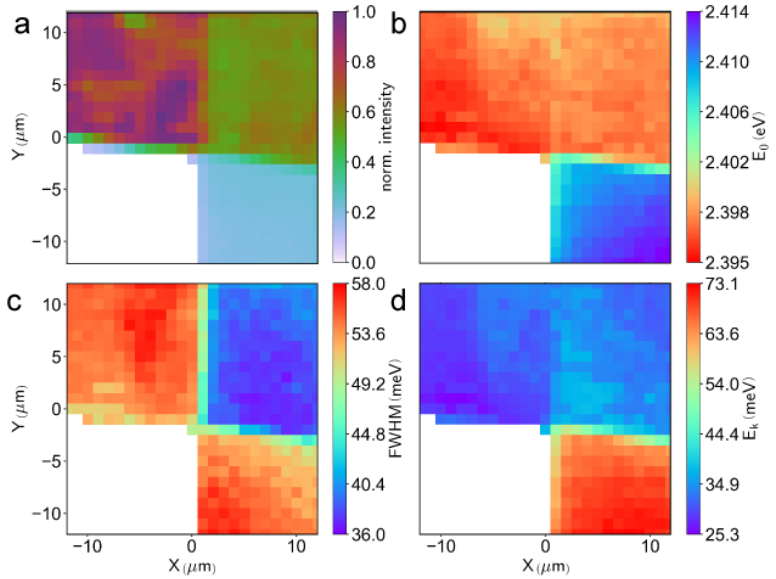

Figure A3.14 PL mapping analysis of the $(PEA)_2PbI_4$/$(HA)_2PbI_4$ heterostructure.

a, Integrated PL intensity mapping. The PL peaks were fitted by an exponentially modified Gaussian function:

$$f(E; E_k, E_0, s) \equiv \frac{1}{2E_k} \exp\left(-\frac{E_0}{E_k} + \frac{s^2}{2E_k^2} + \frac{E}{E_k}\right) \operatorname{erfc}\left(-\frac{E_0}{\sqrt{2}s} + \frac{s^2}{\sqrt{2}sE_k} + \frac{E}{\sqrt{2}s}\right).$$

From this peak fitting analysis, E_0 is the central energy of the Gaussian part, plotted in (**b**); the FWHM is given by $FWHM = s \cdot 2.35482$, plotted in (**c**); E_k is a parameter we introduce to account for the red tailing in the spectra. Plotted in (**d**). White pixels in all panels represent substrate areas, whose intensities are masked due to low fit amplitude.

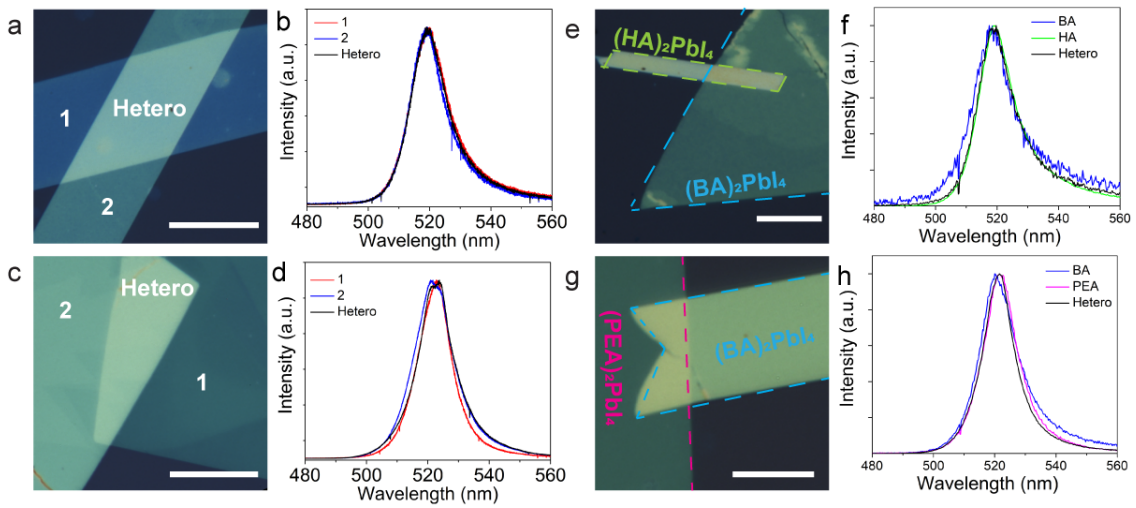

Figure A3.15 Additional experiments examining the PL linewidths of different heterostructures with different LA cations.

Optical images and PL spectra of stacked (**a**, **b**) $(HA)_2PbI_4$ homobilayers, (**c**, **d**) $(PEA)_2PbI_4$ homobilayers, (**e**, **f**) $(BA)_2PbI_4/(HA)_2PbI_4$ heterobilayers, showing no obvious PL linewidth reduction in these stacked bilayer regions (in contrast to the heterobilayers shown in Fig. 3c), and (**g**, **h**) $(BA)_2PbI_4/(PEA)_2PbI_4$ heterobilayers, showing intermediate level of linewidth narrowing in the heterostructure region. Scale bars: 20 μm.

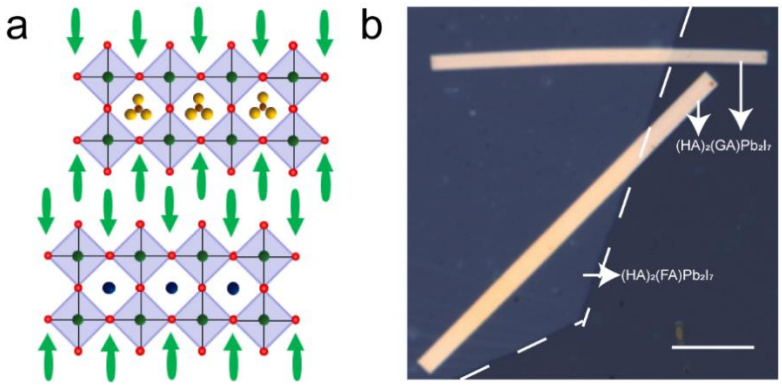

Figure A3.16 $(HA)_2(FA)Pb_2I_7/(HA)_2(GA)Pb_2I_7$ as an example of heterostructures with different A cations.

a, Schematic of the heterostructure with different A cations. Large A cation such as GA significantly influences carrier dynamics and exciton-phonon interactions through modulating the inorganic sublattices. **b,** Optical images of the heterostructure. The outline of the thin $(HA)_2(FA)Pb_2I_7$ sheet is marked by white dashed line. Note that the $(HA)_2(GA)Pb_2I_7$ phase prefers to grow into long ribbons, consistent with what is shown in Fig. 1b. Scale bar: 15 μm.

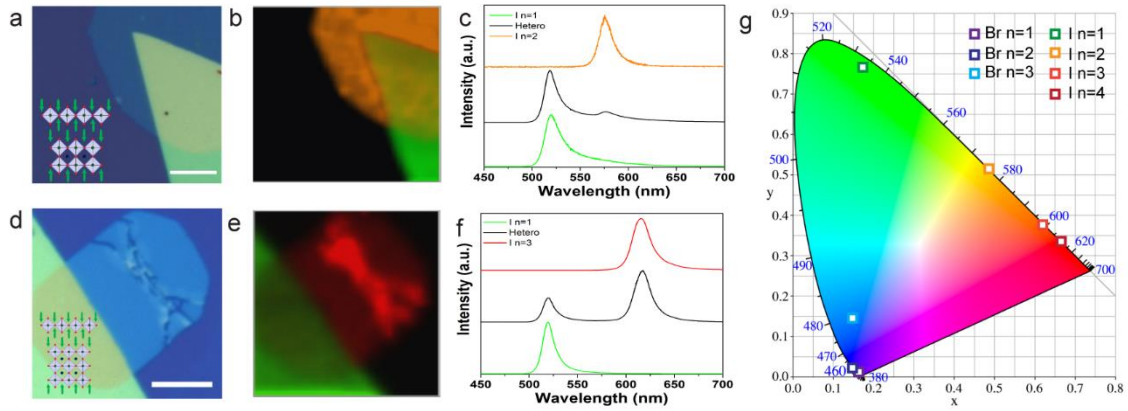

Figure A3.17 Optical and spectral characterization of the heterostructure of different *n* phases.

Optical images (**a**, **d**) and PL characterizations of (**c**) an I *n* = 1/I *n* = 2 heterostructure in comparison to (**d**)-(**f**) an I *n* = 1/I *n* = 3 heterostructure. **b**, **e**, The overlaid PL mapping in 515-525 nm (green), 565-575 nm (orange), and 610-620 nm (red), respectively. **g**, Color gamut of 2D RP perovskites plotted on the CIE 1931 color space chromaticity diagram.

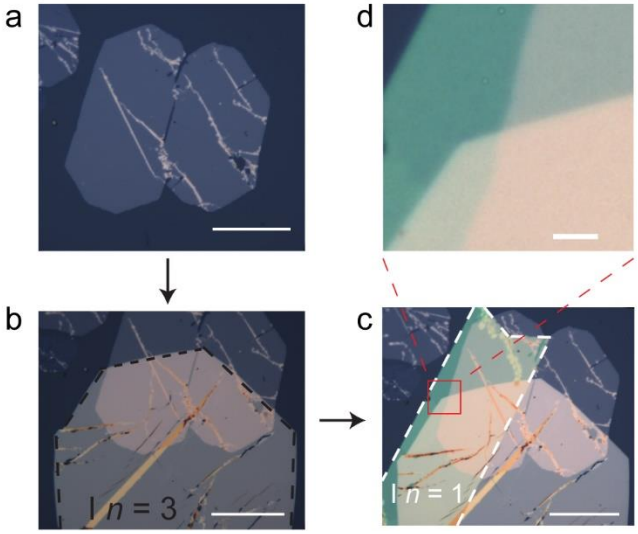

Figure A3.18 Fabrication process of the $(BA)_2PbI_4/(BA)_2(MA)_2Pb_3I_{10}/(BA)_2(MA)Pb_2I_7$ (*n* = 1/ *n* = 3/*n* = 2) multi-heterostructure.

a, The bottom *n* = 2 sheets on Si substrate. **b**, The middle *n* = 3 sheet marked by black dashed line is aligned and transferred on top of the *n* = 2. **c**, The top *n* = 1 sheet marked by white dashed line is aligned and stacked onto previous two layers. Scale bar: 50 μm. The PL mapping area (**d**) showed in the main text is highlighted by the red box. It contains single layer (*n* = 1), double layer (*n* = 1,2 or 1,3) and triple layer (*n* = 1,3,2) areas. Scale bar: 5 μm.

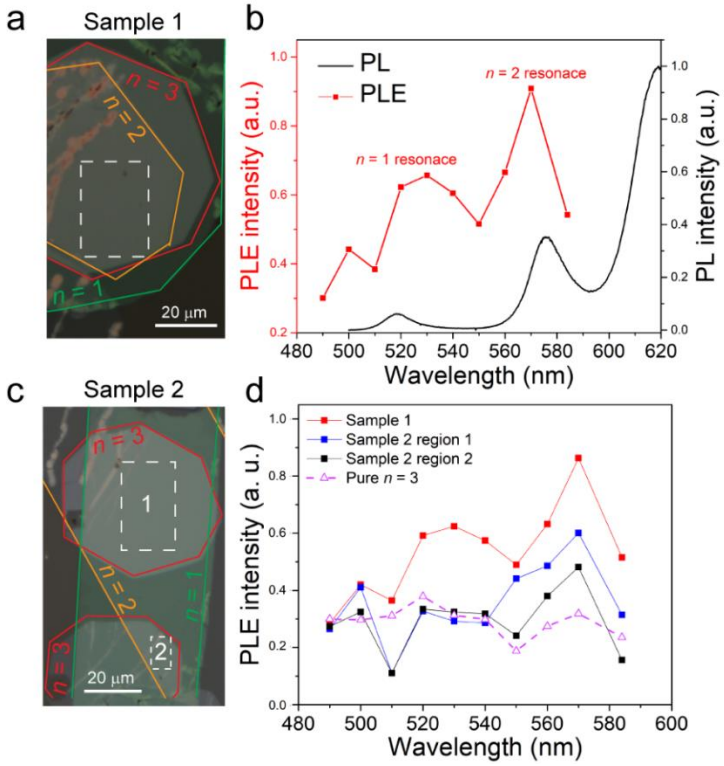

Figure A3.19 Photoluminescence excitation (PLE) spectroscopy experiments on additional $(BA)_2PbI_4/(BA)_2(MA)_2Pb_3I_{10}/(BA)_2(MA)Pb_2I_7$ (1-3-2) multi-heterostructures.

Optical image of heterostructure sample 1 (**a**), and 2 (**c**). The n = 1, n = 2, and n = 3 phases are outlined by green, orange, and red profiles, respectively. **b**, PLE spectrum (red) taken from the multi-heterojunction region marked by white-dashed box in (**a**), overlaid on the PL spectrum of the multi-heterostructure shown in Fig. 4. **d**, PLE spectra taken from multi-heterojunction regions marked by the white boxes in (**a**) (red), and (**c**) (region 1 and 2, blue and black, respectively). The purple dashed spectrum was collected on a pure n = 3 sheet for comparison. The average intensity in each region of interest was normalized by the corresponding incident power to yield the data points in the PLE spectra.

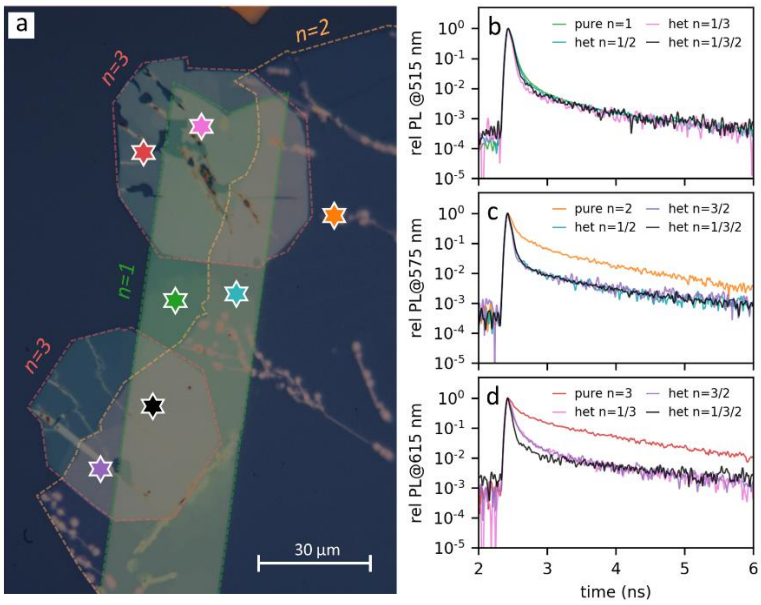

Figure A3.20 Time-resolved photoluminescence (TRPL) spectroscopy experiments on additional $(BA)_2PbI_4/(BA)_2(MA)_2Pb_3I_{10}/(BA)_2(MA)Pb_2I_7$ (*n* = 1/*n* = 3/*n* = 2) multi-heterostructures.

a, Optical image of the heterostructure sample. The *n* = 1, *n* = 2, and *n* = 3 phases are outlined by green, orange, and red profiles, respectively. TRPL curves probed at **b**, *n* =1 emission energy (515 nm), **c**, *n* =2 emission energy (575 nm), **d**, *n* =3 emission energy (615 nm), respectively. The individual TRPL curves were collected in the regions marked by the correspondingly colored stars in **a**.

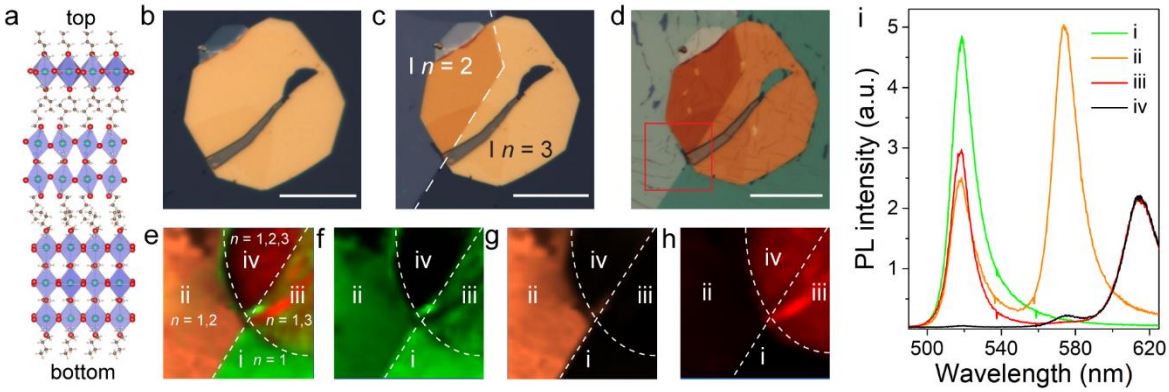

Figure A3.21 Fabrication and characterization of a $(BA)_2PbI_4/(BA)_2(MA)Pb_2I_7/(BA)_2(MA)_2Pb_3I_{10}/$ (n = 1/n = 2/n = 3) multi-heterostructure.

a, Schematic structure of the multi-heterostructure. Note this scheme illustrates the RP phase sequence but does not imply that there is only one monolayer for each phase, however, the number of layers does not change the electronic structure and PL properties. **b**, Optical image of the bottom n = 3 layer on Si substrate. **c**, Then the middle n = 2 layer is transferred on top of it with the edge marked by white dashed line. **d**, The top n = 1 layer is transferred on the top of both structures, covering the entire field of view of this image. Scale bars in (**b**)-(**d**): 25 μm. **e-h**, PL mappings of the heterostructure region marked by the red box in (**d**). **f**) Green corresponds to emission integrated from 515 to 525 nm (corresponds to the n = 1 phase), **g**) orange from 570 to 580 nm (corresponds to the n = 2 phase), and **h**) red from 613 to 623 nm (corresponds to the n = 3 phase). Regions i-iv are assigned similarly to those in Fig. 4 and annotated in (**e**).

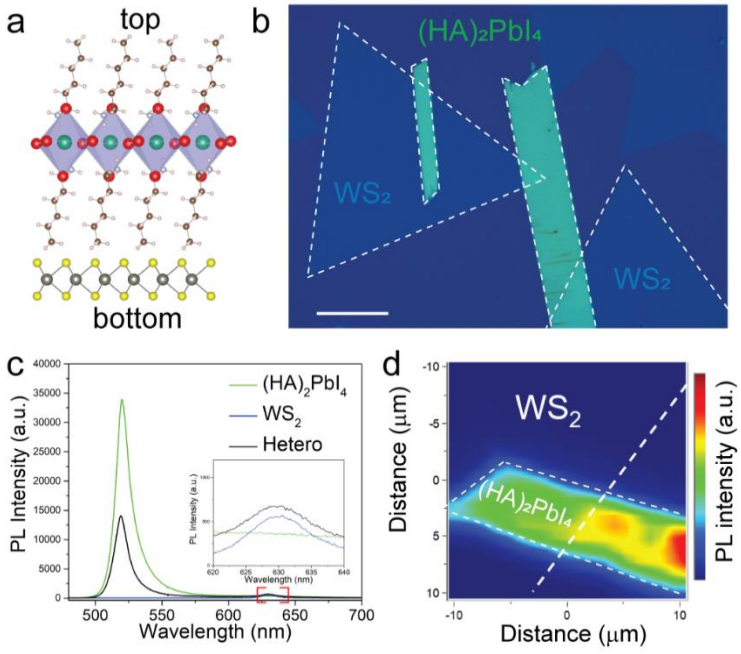

Figure A3.22. Fabrication of vertical heterostructures of $(HA)_2PbI_4$/monolayer WS_2 on Si substrate.

a, Schematic of the heterostructure. Note the scheme does not imply there is only one layer of $(HA)_2PbI_4$, but the number of layers does not change the electronic structure and PL properties of 2D RP perovskites. **b,** Optical image of the heterostructure. The CVD-grown triangularly shaped monolayer WS_2 is at the bottom on Si substrate. The ribbon-shaped $(HA)_2PbI_4$ sheets are then transferred on top of WS_2 monolayers. The outlines of both layers are marked by white dashed lines. Scale bar: 25 μm. **c,** Confocal PL spectra taken at the $(HA)_2PbI_4$ (green), WS_2 (blue), and heterostructure (black) region, respectively. The inset shows magnified spectral range marked by the red box, where PL from WS_2 A-exciton is observed. The PLQY of $(HA)_2PbI_4$ is much higher than that of the WS_2, so the relative PL peak intensity of WS_2 is much lower in the heterostructure spectrum. **d**, PL mapping integrated from 515-525 nm ($(HA)_2PbI_4$ emission) taken at the heterojunction of another heterostructure.

Table A3.1 Recipe for synthesis of different phases 2D RP perovskites.

	LA (M)	A(M)	PbX_2 (M)	T (°C)
$(BA)_2PbBr_4$	0.50	\	0.50	25
$(BA)_2(MA)Pb_2Br_7$	0.43	0.31	0.59	28
$(BA)_2(MA)_2Pb_3Br_{10}$	0.19	0.40	0.59	50
$(BA)_2PbI_4$	0.050	\	0.45	25
$(BA)_2(MA)Pb_2I_7$	0.43	0.31	0.59	30
$(BA)_2(MA)_2Pb_3I_{10}$	0.19	0.40	0.59	65
$(BA)_2(MA)_3Pb_4I_{13}$	0.17	0.52	0.69	70
$(HA)_2PbBr_4$	0.20	\	0.20	25
$(HA)_2PbI_4$	0.050	\	0.45	25
$(HA)_2(MA)Pb_2I_7$	0.15	0.25	0.50	30
$(HA)_2(GA)Pb_2I_7$	0.17	0.52	0.50	50
$(HA)_2(FA)Pb_2I_7$	0.027	0.063	0.45	30
$(HA)_2(MA)_2Pb_3I_{10}$	0.083	0.417	0.50	30
$(HA)_2(MA)_3Pb_4I_{13}$	0.033	0.467	0.50	50
$(HA)_2(MA)_4Pb_5I_{16}$	0.083	0.294	0.80	65
$(PEA)_2PbBr_4$	0.20	\	0.20	55
$(PEA)_2PbI_4$	0.25	\	0.25	70
$(PEA)_2(MA)Pb_2I_7$	0.1	0.6	0.2	55
$(PEA)_2(MA)_2Pb_3I_{10}$	0.033	0.8	0.33	65
$(PMA)_2PbI_4$	0.30	\	0.30	50
$(PMA)_2(MA)Pb_2I_7$	0.88	1.55	0.27	65
$(PA)_2PbI_4$	0.25	\	0.25	50
$(PA)_2(MA)Pb_2I_7$	0.43	0.31	0.59	30
$(PA)_2(MA)_2Pb_3I_{10}$	0.19	0.40	0.59	65

* Room temperature is ~22 °C

Appendix 4. Supporting Information for Chapter 5

Synthesis.

All chemicals were purchased from Sigma-Aldrich and used as received unless noted otherwise. Series of six different $(PA)_2(A)Pb_2I_7$ were synthesized using a solution growth method reported previously with modified conditions.[1] An exemplary synthesis for $(PA)_2(DMA)Pb_2I_7$ is described below:

1 mmol of PbO (223 mg), 0.24 mmol of DMAI (42 mg) were added to 2 mL of concentrated HI solution, before 0.56 mmol (65 μL) of pentylamine was added. The mixture was heated in an oil bath at 125 °C under stirring until a yellow clear solution was obtained. The hot plate was then turned off and the solution was cooled to room temperature. The red crystals settled at the bottom of the vial were separated from the mother liquor, washed by dichloromethane and dried before characterization.

The recipes for all 6 $(PA)_2(A)Pb_2I_7$ perovskite phases are summarized in Table A5.1.

Table A4.1 Recipes for synthesis of various phase-pure $(PA)_2(A)Pb_2I_7$

	[PA] / M	[AI] / M	[PbO] / M
$(PA)_2(MA)Pb_2I_7$	0.14	0.10	0.50
$(PA)_2(FA)Pb_2I_7$	0.12	0.15	0.50
$(PA)_2(DMA)Pb_2I_7$	0.28	0.12	0.50
$(PA)_2(EA)Pb_2I_7$	0.20	0.20	0.50
$(PA)_2(GA)Pb_2I_7$	0.25	0.20	0.50
$(PA)_2(AA)Pb_2I_7$	0.25	0.20	0.50
$(PA)_2(EA)_2Pb_3I_{10}$	0.25	0.50	0.50

Single-Crystal structure determination

$(PA)_2(DMA)Pb_2I_7$. A red crystal with approximate dimensions 0.015 x 0.016 x 0.021 mm^3 was selected under oil under ambient conditions and attached to the tip of a MiTeGen MicroMount©. The crystal was mounted in a stream of cold nitrogen at 100(1) K and centered in the X-ray beam by using a video camera. The crystal evaluation and data collection were performed on a Bruker Quazar SMART APEXII diffractometer with Mo Kα (λ = 0.71073 Å) radiation and the diffractometer to crystal distance of 4.96 cm. The initial cell constants were obtained from three series of ω scans at different starting angles. Each series consisted of 12 frames collected at intervals of 0.5º in a 6º range about ω with an exposure time of 60 seconds per frame. The reflections were successfully indexed by an automated indexing routine built in the APEX3 program suite. The final cell constants were calculated from a set of 9041 strong reflections from the actual data collection.

The data were collected by using a full sphere data collection routine to survey reciprocal space to the extent of a full sphere to a resolution of 0.66 Å. A total of 44196 data were harvested by collecting 6 sets of frames with 0.5º scans in ω and φ with an exposure time of 75 sec per frame. These highly redundant datasets were corrected for Lorentz and polarization effects. The absorption correction was based on fitting a function to the empirical transmission surface as sampled by multiple equivalent measurements.

The systematic absences in the diffraction data were consistent for the space groups $P2_1$ and $P2_1/m$. The E-statistics were inconclusive and only the non-centrosymmetric space group P21 yielded chemically reasonable and computationally stable results of refinement.

A successful solution by intrinsic phasing provided most non-hydrogen atoms from the E-map. The remaining non-hydrogen atoms were located with an alternating series of least-squares cycles and difference Fourier maps. All non-hydrogen atoms were refined with anisotropic displacement coefficients. All hydrogen atoms were included in the structure factor calculation at idealized positions and allowed to ride on the neighboring atoms with relative isotropic displacement coefficients. The structure was refined as a four component non-merohedral twin with a ratio of 27.8(16) : 25.9(9) : 25.2(9) : 21.1(9). Here, the second component is related to the major component by a 180° rotation about reciprocal axis [001], the third component is related to the major component by an inversion, and the fourth component is related to the second component by an inversion. The two PA cations and the DMA cation were refined with geometric and atomic displacement parameter restraints.The final least-squares refinement of 226 parameters against 11083 data resulted in residuals R (based on F^2 for $I \geqslant 2\sigma$) and wR (based on F^2 for all data) of 0.0506 and 0.1177, respectively. The final difference Fourier map contains several peaks of residual electron density (ca. 5.3 $e^-/Å^3$) in the vicinity of the Pb and I atoms. These peaks are in chemically unreasonable positions and were considered noise.

$(PA)_2(AA)Pb_2I_7$. A red crystal with approximate dimensions 0.054 × 0.028 × 0.01 mm^3 was selected under oil under ambient conditions and attached to the tip of a MiTeGen MicroMount©. The crystal was mounted in a stream of cold nitrogen at 100(1) K and centered in the X-ray beam by using a video camera. The crystal evaluation and data

collection were performed on a Bruker Quazar SMART APEXII diffractometer with Mo Kα (λ = 0.71073 Å) radiation and the detector to crystal distance of 4.96 cm.

The initial cell constants were obtained from three series of ω scans at different starting angles. Each series consisted of 12 frames collected at intervals of 0.5º in a 6º range about ω with the exposure time of 60 seconds per frame. The reflections were successfully indexed by an automated indexing routine built in the APEX3 program suite. The final cell constants were calculated from a set of 6459 strong reflections from the actual data collection.

The data were collected by using the full sphere data collection routine to survey the reciprocal space to the extent of a full sphere to a resolution of 0.8 Å. A total of 22130 data were harvested by collecting 4 sets of frames with 0.5º scans in ω and φ with exposure times of 75 sec per frame. These highly redundant datasets were corrected for Lorentz and polarization effects. The absorption correction was based on fitting a function to the empirical transmission surface as sampled by multiple equivalent measurements.

The systematic absences in the diffraction data were consistent for the space groups *Cc* and *C2/c*. The E-statistics strongly suggested the centrosymmetric space group *C2/c* that yielded chemically reasonable and computationally stable results of refinement. A successful solution by intrinsic phasing provided most non-hydrogen atoms from the E-map. The remaining non-hydrogen atoms were located in an alternating series of least-squares cycles and difference Fourier maps. All non-hydrogen atoms were refined with anisotropic displacement coefficients. All hydrogen atoms were included in the structure

factor calculation at idealized positions and were allowed to ride on the neighboring atoms with relative isotropic displacement coefficients. The crystal appeared to be split and was treated as a pseudo-merohedral twin. The second component contribution is 14.4(6) %. Atom I1 is disordered over two positions with the major component contribution of 90.0(11) %. Atom I4 is equally disordered over a crystallographic two-fold axis. The (1-aminoethylidene)azanium resides on a crystallographic two-fold axis. Atom N2 is disordered over two positions with the major component contribution of 59(4) %. The data quality is low and thus many atomic displacement parameter constraints and restraints were used to achieve a stable refinement. The (1-aminoethylidene)azanium was refined assuming its molecular symmetry was consistent with the symmetry of the site it occupies (2-fold axis). Its interatomic distances were refined with restraints. The final least-squares refinement of 93 parameters against 3327 data resulted in residuals R (based on F^2 for $I \geqslant 2\sigma$) and wR (based on F^2 for all data) of 0.0891 and 0.1879, respectively. The final difference Fourier map contains numerous residual electron density peaks and valleys. Several additional disorder models were considered but none was satisfactory.

$(PA)_2(EA)Pb_3I_{10}$. A red crystal with approximate dimensions 0.009 x 0.017 x 0.045 mm^3 was selected under oil under ambient conditions and attached to the tip of a MiTeGen MicroMount©. The crystal was mounted in a stream of cold nitrogen at 100(1) K and centered in the X-ray beam by using a video camera.

The crystal evaluation and data collection were performed on a Bruker Quazar SMART APEXII diffractometer with Mo K_α (λ = 0.71073 Å) radiation and the diffractometer to crystal distance of 4.96 cm.

The initial cell constants were obtained from three series of ω scans at different starting angles. Each series consisted of 12 frames collected at intervals of 0.5º in a 6º range about ω with an exposure time of 60 seconds per frame. The reflections were successfully indexed by an automated indexing routine built in the APEX3 program suite. The final cell constants were calculated from a set of 4841 strong reflections from the actual data collection.

The data were collected by using a full sphere data collection routine to survey reciprocal space to the extent of a full sphere to a resolution of 0.73 Å. A total of 54440 data were harvested by collecting 6 sets of frames with 0.5º scans in ω and φ with an exposure time of 75 sec per frame. These highly redundant datasets were corrected for Lorentz and polarization effects. The absorption correction was based on fitting a function to the empirical transmission surface as sampled by multiple equivalent measurements.

Powder X-ray Diffraction

The powder X-ray diffraction (PXRD) patterns were collected on a Bruker D8 Advance X-ray diffractometer with Cu Kα radiation.

Steady-State Photoluminescence

Steady-state confocal PL spectra were collected on exfoliated flakes with a Horiba Labram Aramis confocal Raman microscope at ambient conditions in PL mode using a

442 nm CW He/Cd laser. The laser beam was attenuated by neutral filters and focused on to the sample via a ×50 objective, producing a spot diameter of ~1 μm, giving an estimated laser power of 300 W cm^{-2}. The samples are protected by polystyrene, and are stored in desiccators at room temperature between measurements.

Steady-State Absorption and Time-Resolved Photoluminescence

Second-Harmonic Generation Measurements

Computational details

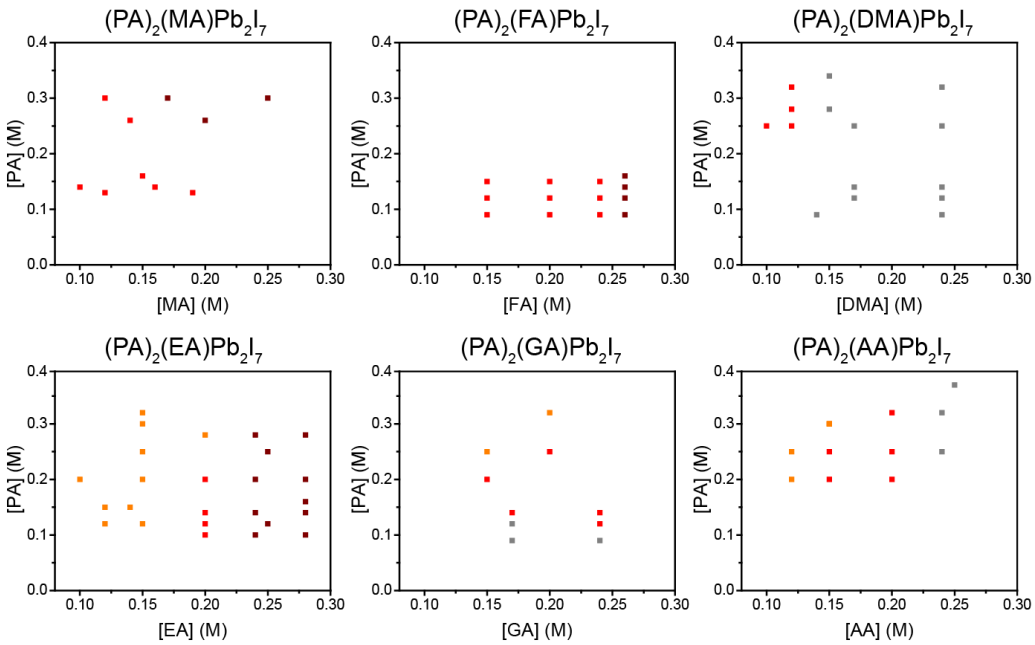

Figure A4.1. Syntheses of $(PA)_2(A)Pb_2I_7$ using different [PA] and [A] concentrations. Each data point represents a synthetic attempt. The data point is colored yellow if any n = 1 crystals were spotted (based on color) in the vial using the corresponding conditions; the data point is colored brown if any n = 3 crystals were spotted (based on color) in the vial using the corresponding conditions; the suitable synthetic window for phase-pure n = 2

crystals are thus shown by the red data points. The grey data points represent conditions where precursors cannot be fully dissolved after extended heating.

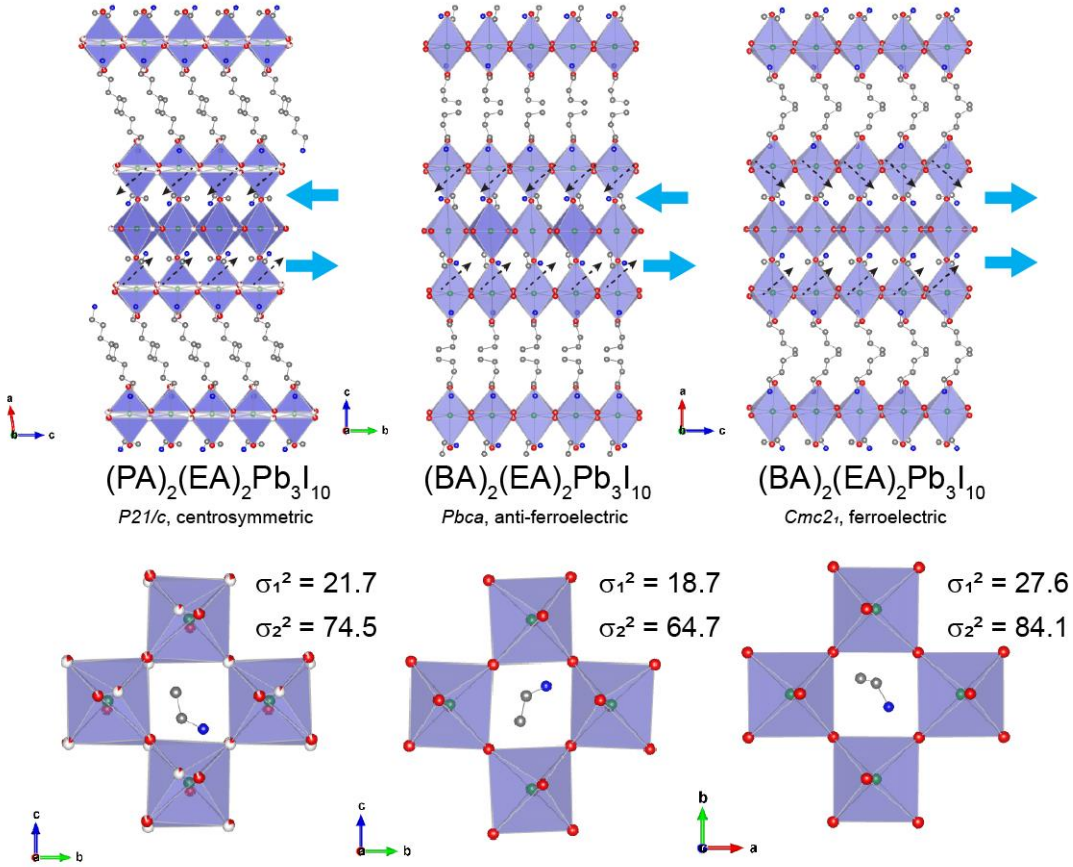

Figure A4.2 Structural comparison of $(PA)_2(EA)_2Pb_3I_{10}$, $(BA)_2(EA)_2Pb_3I_{10}$ anti-ferroelectric phase and $(BA)_2(EA)_2Pb_3I_{10}$ ferroelectric phase.

The dipoles of EA are shown by dashed arrows, and the resultant dipole are shown by blue arrow. The anti-parallel dipole alignment in the $(PA)_2(EA)_2Pb_3I_{10}$, $(BA)_2(EA)_2Pb_3I_{10}$ anti-ferroelectric phase lead to non-polar, centrosymmetric structures, whereas parallel dipole alignment of lead to non-centrosymmetric in $(BA)_2(EA)_2Pb_3I_{10}$ ferroelectric phase.

Table A4.2 Coordinates of the point charges in $(PA)_2(DMA)Pb_2I_7$.

Atoms	Coordinates		Central coordinate
Pb	(0.68381,0.24307,0.83756)	(0.81277,0.24506,0.16373)	(0.5, 0.49406, 0.5)
	(0.18723,0.74506,0.83627)	(0.31619,0.74307,0.16244)	
N (PA)	(0.82800,0.70600,0.26600)	(0.38300,0.28600,0.26610)	(0.5, 0.49600, 0.5)
	(0.61700,0.78600,0.73390)	(0.17200,0.20600,0.73400)	
N(DMA)	(0.18700,0.17300,0.98200)	(0.81300,0.67300,0.01800)	(0.5, 0.42300, 0.5)

Based on the crystal structure, we select a unit cell and assume that the centers of the positive charges of the DMA, PA and the negative charges of the $(Pb_2I_7)^{3-}$ are located on the N atoms and Pb atoms, respectively.

$$|P_s| = |[(-e \times 0.49406) \times 6 + (e \times 0.49600) \times 4 + (e \times 0.42300) \times 2] \times \frac{b}{V}|$$

$$= \left|-0.13436 \times 1.6 \times 10^{-19} \times 9.124 \div 1615.35 \times 10^{20} \ \frac{C}{m^2}\right| = 1.2\ \mu C/cm^2$$

Table A4.3 Structural parameters for $(PA)_2(EA)_2Pb_3I_{10}$

	$(PA)_2(EA)Pb_3I_{10}$
crystal system	monoclinic
space group	*P2₁/c*
	27.067(9); 90

***a*/Å; α/°**	8.818(3); 97.714(9)
***b*/Å; β/°**	8.981(3); 90
***c*/Å; γ/°**	
volume/ Å^3	2124.2(12)
Z	2
density (calc.) / g/cm^3	3.376
reflections collected	54440
independt reflectinons	5762
	[R_{int} = 0.1189, R_{sigma} = 0.0712]
No. of data/restraints/params.	5762/0/92
Goodness-of-fit on F^2	1.068
Final *R* indexes	R_1 = 0.0956, wR_2 =
[I ≥ 2σ(I)]	0.2065
Final *R* indexes	R_1 = 0.1230, wR_2 = 2195
[all data]	
Largest diff. peak /hole / e Å^{-3}	6.87/-4.62

References

1 Stoumpos, C. C. *et al.* Ruddlesden-Popper Hybrid Lead Iodide Perovskite 2D Homologous Semiconductors. *Chem Mater* **28**, 2852-2867, doi:10.1021/acs.chemmater.6b00847 (2016).

2 Morrow, D. J. *et al.* Disentangling Second Harmonic Generation from Multiphoton Photoluminescence in Halide Perovskites using Multidimensional Harmonic Generation. *J Phys Chem Lett* **11**, 6551-6559, doi:10.1021/acs.jpclett.0c01720 (2020).